Application of Quasi-Solid-State Electrolyte, Alternative Polymer Counter Electrode, and Up-Conversion Nanomaterials to Dye-Sensitized Solar Cells

チャワランブワ ファザイ レスリー

Application of Quasi-Solid-State Electrolyte, Alternative Polymer Counter Electrode, and Up-Conversion Nanomaterials to Dye-Sensitized Solar Cells.

A Thesis

For

Doctor of Engineering in Electrical and Electronic Engineering

Kyushu University

CHAWARAMBWA Fadzai Lesley

Graduate School of Information Science and Electrical Engineering

February 2023

Abstract

Dye-sensitized solar cells (DSSC) are a new generation type of solar cells that have received a lot of attention due to their unique qualities such as low cost of production, ease of fabrication and high efficiency under low light illumination. A DSSC cell structure is mainly divided into three parts namely, the anode, the electrolyte, and the counter electrode. To improve the performance of a DSSC all three sections of the DSSC must be investigated. This study is divided into three sections: the photoanode section, the counter electrode section, and the electrolyte section.

Under the anode section, up-conversion materials were investigated. Upconversion, materials can convert at least two lower energy photons into higher energy photons. Upconversion, nanomaterials were fabricated using a facile urea-based homogeneous precipitation method. The nanomaterials were characterized using XRD and photoluminescent microscopy and employed on the photoanode of the DSSC. The performance of various up nanomaterials was simulated under a 100 mW/cm^2 Xeon lamp solar simulator. Furthermore, a study on the effect of co-sensitization on the performance of the DSSC was also conducted. Co-sensitization is an excellent technique to enhance the performance of a dye-sensitized solar cell (DSSCs) by broadening the cell's absorption spectrum.

In the counter electrode section new electrocatalysis, polymer materials were developed and employed on the DSSC. The catalytic activity of the new materials was investigated using CV, EIS, and IV curves obtained from the solar simulator. The feasibility of these new materials to replace the Pt electrode of the DSSC was also evaluated.

Under the electrolyte section, printable polymer gel quasi-solid electrolyte (QSE) materials were developed using three different nanofillers namely, titanium dioxide (TiO$_2$), silicon nitride (Si$_3$N$_4$), and titanium carbon nitride (TiCN) nanoparticles. The quasi-solid dye-sensitized solar cells (QSDSSC) that were developed with these QSEs were then coupled to a concentric mirror under focused irradiation. The performance and stability of the QSDSSC under focused irradiation was investigated under continuous light soaking for 120 minutes.

Dedications

To my mother, Amoria,

for teaching me the power of love, the significance of kindness, the

importance of education, and the value of hard work.

List of Journal Publications

1) **Chawarambwa, F. L**., Putri, T. E., Pankaj, A., Kamataki, K., Itagaki, N., Koga, K., & Shiratani, M. (2022). The Effects of Spin-Coating Rate on Surface Roughness, Thickness, and Electrochemical Properties of a Pt Polymer Counter Electrode. Advance Engineering Forum, 2234-991X, Vol. 45, 1-13 https://doi.org/10.4028/p-6l16rl

2) **Chawarambwa, F. L**., Putri, T. E., Pankaj, A., Kamataki, K., Itagaki, N., Koga, K., & Shiratani, M. (2022). Performances of carbon black-titanium nitrate and carbon black-titanium/Triton X-100 composite polymer counter electrodes for dye-sensitized solar cells. Advanced Materials Research, 1168, 35–47.
https://doi.org/10.4028/www.scientific.net/amr.1168.35

3) **Chawarambwa, F. L**., Putri, T. E., Hwang, S.-H., Attri, P., Kamataki, K., Itagaki, N., Koga, K., Nakamura, D., & Shiratani, M. (2022). Improved luminescence performance of Yb^{3+}-Er^{3+}-Zn^{2+}: Y_2O_3 phosphor and its application to solar cells. Optical Materials, 123, 111928.
https://doi.org/10.1016/j.optmat.2021.111928

4) Putri, T. E., Hao, Y., **Chawarambwa, F. L**., Seo, H., Son, M. K., Kamataki, K., Itagaki, N., Koga, K., & Shiratani, M. (2022). Performance Comparison of Nitrile Based Liquid Electrolytes on Bifacial Dye-Sensitized Solar Cells Under Low Concentrated light. Materials Research Society Advances (MRSA) 7, 427–432. https://doi.org/10.1557/s43580-022-00270-x

5) Putri, T. E., **Chawarambwa, F. L**., Son, M.-K., Attri, P., Kamataki, K., Itagaki, N., Koga, K., & Shiratani, M. (2021). Performance characteristics of bifacial dye-sensitized solar cells with a V-shaped low-concentrating light system. ACS Applied Energy Materials, 4(12), 13410–13414. https://doi.org/10.1021/acsaem.1c02774

6) **Chawarambwa, F. L**., Putri, T. E., Attri, P., Kamataki, K., Itagaki, N., Koga, K., & Shiratani, M. (2021). Effects of concentrated light on the performance and stability of a quasi-solid electrolyte in dye-sensitized solar cells. Chemical Physics Letters, 781, 138986.
https://doi.org/10.1016/j.cplett.2021.138986

7) **Chawarambwa, F. L.**, Putri, T. E., Kamataki, K., Shiratani, M., Koga, K., Itagaki, N., & Nakamura, D. (2021). Synthesis of Yb^{3+}/Ho^{3+} co-doped Y_2O_3 nanoparticles and its application to dye sensitized solar cells. Journal of Molecular Structure, 1228, 129479.
https://doi.org/10.1016/j.molstruc.2020.129479

8) Putri, T. E., Hao, Y., **Chawarambwa, F. L.**, Seo, H., Son, M. K., Kamataki, K., Itagaki, N., Koga, K., & Shiratani, M. (2021). Effects of activated carbon counter electrode on bifacial dye sensitized solar cells (DSSCs). Materials Science Forum, 1016, 863–868. https://doi.org/10.4028/www.scientific.net/msf.1016.863

9) **Chawarambwa, F. L.**, Putri, T. E., Attri, P., Kamataki, K., Itagaki, N., Koga, K., & Shiratani, M. (2021). Highly efficient and transparent counter electrode for application in bifacial solar cells. Chemical Physics Letters, 768, 138369. https://doi.org/10.1016/j.cplett.2021.138369

10) **Chawarambwa, F. L.**, Putri, T. E., Son, M.K., Kamataki, K., Itagaki, N., Koga, K., & Shiratani, M. (2020). Graphene-Si_3N_4 nanocomposite blended polymer counter electrode for low-cost dye-sensitized solar cells. Chemical Physics Letters, 758, 137920. https://doi.org/10.1016/j.cplett.2020.137920

Table of Contents

x

x

CHAPTER ONE: INTRODUCTION

1.1 Introduction

The world`s population is growing at an exponential rate. According to the United Nations` research [1], the human population is expected to be nearly 10 billion by the end of the year 2050. As such, it has been projected that this population will consume approximately 30TW of power at that time [1]. The current energy scenario in the world relies mainly on unsustainable energy sources such as fossil fuels to supply the increasing energy demand. Even though this long-adopted pattern ensures electricity availability on demand through the least cost-proven technology, it is profoundly unsustainable because of its drastic impacts on environmental emissions and depletion of resources.

The burning of fossil fuels for power generation is a major contributor to global warming from the emissions of greenhouse gases, chiefly CO_2 [2]. For coal-fired thermal power stations, the ratio of CO_2 emissions to electricity production is extremely high. Considering that power generation from fossil fuels is set to continue well into this century, supplying the current energy demands and the expected future increases, requires action to be taken now if targets are to be met.

The growing need for energy by human society and the exhaustion of fossil energy sources calls for a sustainable, safe, low-cost, and ever-present energy source [2]. One of the most appropriate ways to solve the conceivable world`s energy crisis is to use the power of the sun. Photovoltaics among other renewable energy sources have the capability of supplanting existing conventional power-generating systems in meeting this increasing energy demand. According to Tai-Jin Kim [3], about 89PW of solar energy is absorbed by the earth`s surface, by converting only 0.034% of this power all the world`s energy requirements can be met.

However, it is unfortunate since the current solar energy conversion technologies are quite insufficient and too costly to be used for this task [4]. These costs are attributed to the solar modules themselves, land requirements, and power conversion devices such as invertors. Recent studies have shown a big decline in power generating cost of photovoltaics due to economies of

scale and this has allowed photovoltaic to be a direct contender of fossil fuel power-generating technologies [4]. However, photovoltaics still suffers from reduced efficiency and weather intermittency [4]. To truly reduce photovoltaic power generating costs, there is a need of improving power conversion efficiencies. By improving power conversion efficiencies, land requirements for photovoltaic power generation are reduced which further lowers power generation costs. The main objective is therefore to improve efficiencies in current technologies keeping in mind not to sacrifice the cost of production to decrease the total cost per watt of photovoltaic energy.

Dye Sensitised Solar Cells are a new breed of third-generation solar cells. This cell exhibits excellent qualities ranging from a low cost of production, and ease of production to high power conversion efficiency [5]. As a result, this cell has received a lot of acclamation and is currently undergoing extensive investigation due to its promising properties. The efficiency of DSSC has increased from 11% [5] to 14.6% [6] ever since the first DSSC solar cell was developed by Gratzel and his team. Consequently, DSSCs have emerged as one of the most efficient third-generation photovoltaic cells with simple manufacturing procedures. In addition, DSSCs exhibit better conversion efficiency than conventional silicon cells in diffuse light or cloudy conditions. Despite, the considerable advances in DSSCs, [5, 6] that have been made in the past two decades, enhancing efficiency remains challenging.

1.2 Background of the problem 1

PV solar cells can convert sunlight into electricity. The rate of conversion by the PV cells is mainly determined by the light absorption capability of the cell. Despite PV technologies that have been developed in this century, the production of solar power remains costly, mainly due to the low power conversion efficiencies of PV solar cells [4]. The efficiency of current PV solar cells is significantly impeded by the transmission loss of the sub-band gap photons. The main problem in improving the conversion efficiency of PV solar cells lies in the mismatch between photons' energy distribution in the incident solar spectrum and the bandgap of semiconductor material [6- 8]. Dye Sensitised Solar Cells generally use visible light for photo-generation. In a DSSC, light absorption is conducted by a light sensitisable dye. The ability of the dye to capture

light in a wide band range of the light spectrum heavily determines the light-electricity efficiency of the DSSC. The currently employed dyes in DSSC with the highest conversion efficiencies (N-719, N-749) have a solar spectrum absorption range of 300-800 nm [7,8]. Consequently, the inability of these dyes to absorb infrared (IR) light (800-2500 nm), which makes up 52% of the energy of the entire solar spectrum, forms the main energy loss mechanism of DSSC solar cells [9-13]. A challenge now arises of how to overcome this problem while employing low-cost, and environmentally friendly means.

Recent research has established that photon conversion can circumvent photon transmission losses. This technology enables single-junction photovoltaic cells to break the Shockly-Queisser limit through the transformation of the solar spectrum. Photon conversion basically can be branched into two groups [7,8].

4. **Up-conversion:** two low-energy sub-band photons are combined and transformed into one high-energy photon.
5. **Downshifting:** One high-energy photon is transformed into one or two lower-energy photons.

Currently, three distinct photon up-conversion materials are being investigated namely [7], a) Rare Earth doped micro and nano crystals (RED-UC) b) Up-conversion quantum nanoparticles (QN-UC), and c) Triplet-triplet annihilation up-conversion (TTA-UC). This study will be focused on the application of rare earth material in photon conversion.

1.3 Background of the problem 2

The counter electrode in the DSSC plays an important role since the fill factor of the cell is determined by the catalytic activity of the counter electrode. Currently, due to its high catalytic activity, platinum (Pt) is the most used material for the counter electrode. Unfortunately, Pt is both rare and very expensive, costing about 4 x 10^4 US\$/Kg [6–9]. Thus, there is a significant need to develop a less costly counter electrode for DSSCs. To this end, many studies have been conducted on various materials, such as carbon [14] and polymers [15], as potential substitutes for the Pt counter electrode. This study focuses on polymer counter electrodes to make low-cost DSSCs. Due to its catalytic property and high stability, (PEDOT:PSS) poly (3, 4-ethylene

dioxythiophene): poly (styrene sulfonate) is one of the most researched polymer materials for various applications. However, PEDOT:PSS has a low catalytic activity which decreases its fill factor (FF), leading to a reduction in the conversion efficiency of the DSSC. To overcome this challenge, researchers have experimented on the effects of blending PEDOT: PSS with various materials, such as dimethyl sulfoxide (DMSO) [14], carbon [16-20], TiO_2 [21], $CuInS_2$[22], and CoS [23]. Unfortunately, most previous studies did not attain the much hoped-for performance as compared to the DSSCs based on Pt counter electrodes. In addition, such studies still need complicated procedures or expensive materials. In this study, highly transparent CEs and carbon-based CEs were developed for efficient low-cost DSSCs.

1.4 Background of the problem 3

The electrolyte is one of the crucial components of the DSSC [24,25]. The electrolyte is responsible for the inner charge carrier transport between the CE and the photoanode and the continuous regeneration of the dye and itself during the DSSC process [8, 13, 24]. The electrolyte has a great influence on both the light-to-electric conversion efficiency and the long-term stability of the DSSC. Most DSSCs require the use of liquid solvents for their electrolyte [26]. The use of liquid solvents presents many challenges such as volatilization and leakage of the organic solvents, which in turn reduce the long-term stability of the DSSC [27]. One suggested solution to this, is to use solid electrolytes or to employ polymer gel electrolytes (PGEs) with in-situ gelation properties [28]. Therefore, in this study, we fabricated a printable quasi-solid electrolyte with various nanofillers and poly(ethylene) oxide (PEO) as the gelation polymer.

1.5 Objectives

   i.   To synthesize up conversion nanomaterials for application in DSSCs
   ii.   Optimization of the Rare Earth ion (Er^{3+}, Zn^{2+}, Yb^{3+}) concentration in the efficient host (Y_2O_3) as a function of incident solar concentration and under broadband excitation.
   iii.   Develop a cost-effective and efficient counter electrode for DSSC
   iv.   Develop cost-effective, efficient, and stable polymer-based quasi-solid electrolytes with TiO_2, TiCN, and Si_3N_4 nanofillers

v. Characterization of the DSSC by employing; Scanning Emission Microscope (SEM), X-Ray Diffraction (XRD, fluorescent spectrometer, and solar spectrum simulator.

1.6 References

1. United Nations Dept. of Economic and Social Affairs, "World Population Prospects: The 2008 Revision," Population Newsletter, pp. 1-20, June 2009.

2. I. Ahmed, M. Rehan, A. Basit, & K. Hong. Sci Rep 12, 12380 (2022).

3. Tai-Jin Kim Open Journal of Earthquake Research. Vol.7 No.3, 2018

4. G. Kavlak, J. McNerney, J. E. Trancik, Energy Policy, 2018, Pgs. 700-710.

5. B. O`Regan and M. Gratzel, Nature, 1991, 353, 737

6. Y.K. Eom, S.H. Kang, I.T. Choi, Y. Yoo, J. Kim, H.K. Kim J. Mater. Chem. A, 5 (2017), p. 2297

7. Yunfei Shang., Nanomaterials, 2079-4991, 1782 (2015).

8. Jessica de Wild, "Photon upconversion for thin film solar cells," 2012

9. Shruti Agarkar, "Dye sensitized solar cell: Optimizing material, methods and optoelectronic effects," (2014)

10. Yi-Hua Fan, Ching-Yuan Ho and Yaw-Jen Chang. Hindawi, 9152973, 7 (2017)

11. Nannan Yao, Jinzhao Huang, Ke Fu et al, Journal of Power Sources 267 (2014) 405-410

12. Peng Du, Joo Ho Lim et al, Nanoscale Research Letters (2015) 10:321

13. Xiaoyong Huang, Sanyang Han et al, Chem. Soc. Rev., 2013,42, 173

14. J.-G. Chen, H.-Y. Wei, K.-C. Ho, Sol. Energ. Mat. Sol. C 91 (2007) 1472–1477.

15. Q. Li, J. Wu, Q. Tang, Z. Lan, P. Li, J. Lin, L. Fan, Electrochem.Commun.10(2008)1299

16. W. Hong, Y. Xu, G. Lu, C. Li, G. Shi, Electrochem. Commun. 10 (2008) 1555–1558.

17. H. Wang, Y. H. Hu, Energy Environ. Sci., 5 (2012) 8182–8188.

18. P. Balraju, M. Kumar, M. S. Roy, G. D. Sharma, Synth. Met. 159 (2009) 1325–1331.

19. H. Sakamoto, S. Igarashi, M. Uchida, K. Niume, M. Nagai, Org. Electron. 13 (2012) 514–518.

20. G. Yue, J. Wu, Y. Xiao, J. Lin, M. Huang, Electrochim. Acta 67 (2012) 113–118.

21. W. Maiaugree, S. Pimanpang, M. Towannang, S. Saekow, W. Jarernboon, V. Amornkitbamrung, J. Non-Cryst. 358 (2012) 2489–2495.

22. Z. Zhang, X. Zhang, H. Xu, Z. Liu, S. Pang, X. Zhou, S. Dong, X. Chen, G. Cui, Appl. Mater. Interfaces 4 (2012) 6242–6246.

23. P. Sudhagar, S. Nagarajan, Y.-G. Lee, D. Song, T. Son, W. Cho, M. Heo, K. Lee, J. Won, Y. S. Kang, ACS Appl. Mater. Interfaces 3 (2011) 1838–1843.

24. L. Goncalves. Bermudez, H. Ribeiroa, A. Mendes. Energy Environ. Sci. 2008, 1, 655

25. J. Wu, Z. Lan, J. Lin, M. Huang, Y. Huang, L. Fan & G. Luo. Chem Rev. 2015, 115, 5, 2136-2173

26. J.M. Cole, G. Pepe, O.K.A. Bahri, C.B. Chem. Rev., 119 (2019), pp. 7279-7327

27. C.-P. Lee, C.-T. Li, K.-C. Ho, Mater Today Off., 20 (2017), pp. 267-283

28. S. Yuan, Q. Tang, B. Hu, C. Ma, J. Duan, B. He J. Mater. Chem. A, 2 (2014), p. 2814

CHAPTER TWO: LITERATURE REVIEW

2.0 Introduction

In this chapter, some fundamentals required on the current technology, materials, operation, fabrication, and characterization of dye-sensitized solar cells were reviewed.

2.1 Dye-Sensitized Solar Cell

The dye-sensitized solar cell was developed by O'Regan and his team in 1991 [1]. DSSC is one of the cells that divide the function of light harvesting and charge-carrier transport. The overall cell efficiency of the DSSC is relatively low (~13% at full sunlight) which is about half that of conventional silicon solar cells. Despite this, DSSC is a very promising photovoltaic technology since it offers excellent features such as high transparency, low cost of production, ease of fabrication, flexibility, and multi-color range possibilities [2,3,4]. **Figure 2.1** illustrates some of the daily applications of the DSSC. **Figure 2.2** shows the schematic of the DSSC [3].
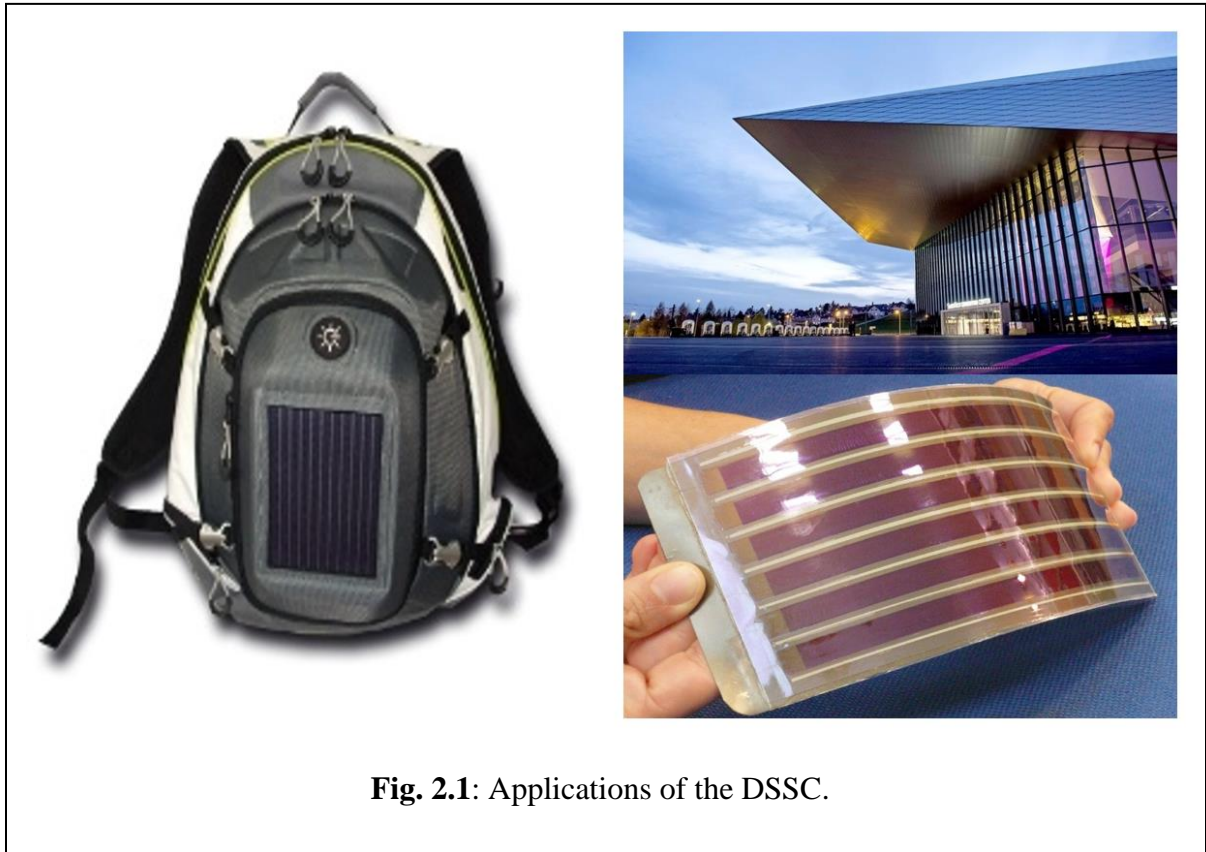
Fig. 2.1: Applications of the DSSC.
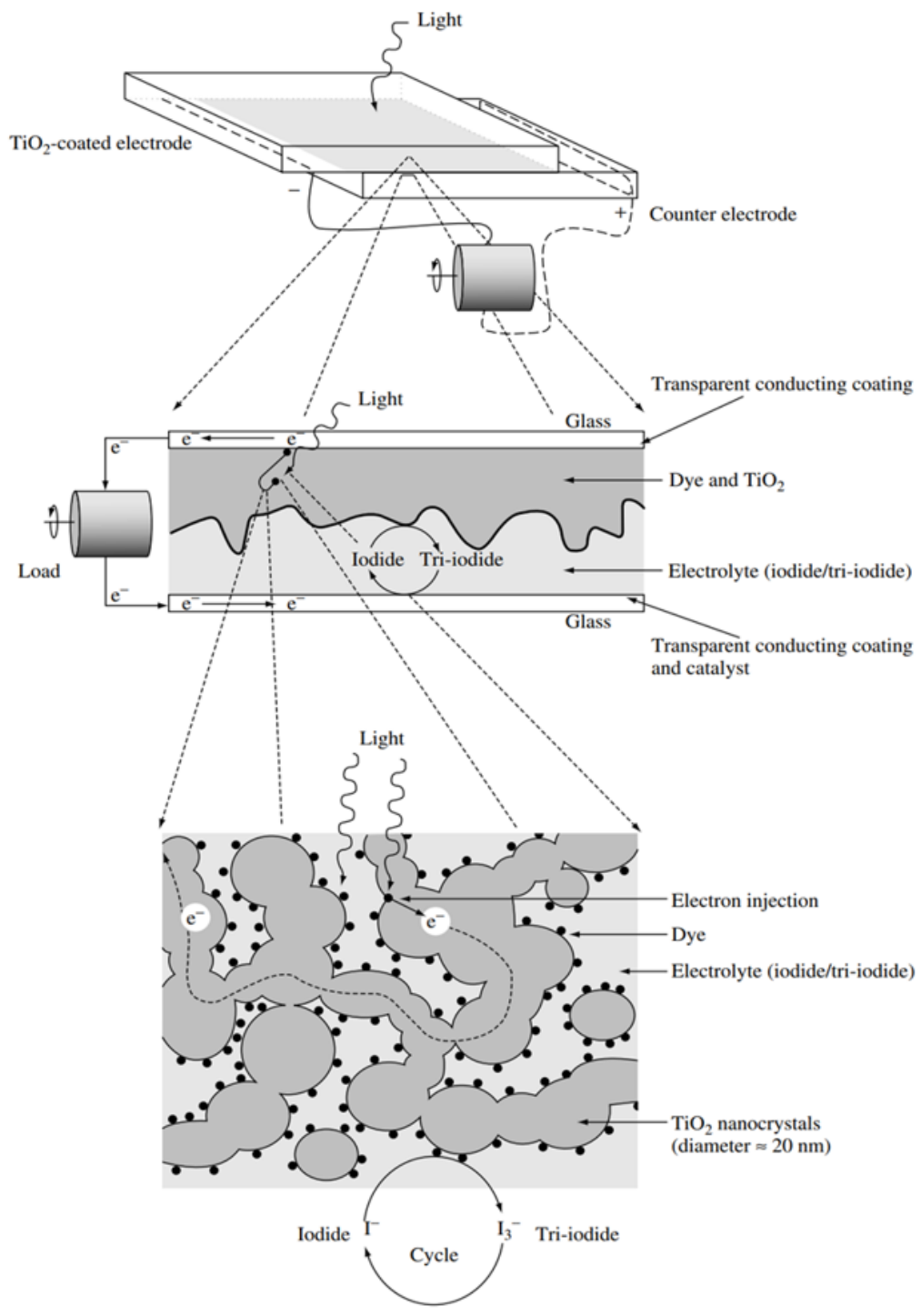
Fig. 2.2: Schematic of the DSSC.

2.2 Structure of DSSC

2.2.1 TiO$_2$ photo anode

The DSSC is mainly composed of three components: the photoanode, the electrolyte, and the counter electrode (CE). Usually a transparent conducting oxide (TCO)-coated glass is used as the substrate for the DSSC. Fluorine or Indium doped Tin Oxide (FTO/ITO) is the commonly used TCO material in DSSCs. The photoanode consists of a mesoporous layer of a wide-bandgap oxide semiconductor. Different oxides can be used however TiO$_2$ is the most commonly used semiconductor. TiO$_2$ delivers the best efficiency, is transparent, non-toxic, chemically stable, and is available in large amounts [1,3]. Another advantage of the TiO$_2$ semiconductor is that it has a suitable LUMO and HOMO alignment with the dye and electrolyte respectively.

A film of TiO$_2$ paste is coated onto the FTO glass and then sintered at 450-500 ℃ for 30 minutes, producing a thin film (~10 µm). The particle size of the TiO$_2$ is between 10-30 nm, as a result, the total surface area, and roughness structure (rf) of the TiO$_2$ layer is about 1000. The dye is adsorbed on the TiO$_2$ surface in a monolayer [1-2]. The dye monolayer is responsible for effective electron injection into the TiO$_2$ layer however light harvesting from a single dye monolayer is very small. This is where the mesoporous structure of the semiconductor is effective, as it increases the amount of the dye adsorbed by the TiO$_2$ on the order of 10^{-7} mol/cm^2.

The porosity of the semiconductor layer is also very important since it dictates how the electrolyte penetrates the film [4]. The porosity of the semiconductor layer can be controlled in the sintering process by adding polymers such as ethyl cellulose (EC) and polyethylene glycol (PEG) into the semiconductor paste.

2.2.2 Dye/Photosensitizer

The semiconductor is sensitized by dye molecules. The photosensitizer is responsible for the primary steps of photon absorption and electron injection into the semiconductor layer [1,5]. The mainly employed dye molecules are the Ruthenium ion-based dyes. The standard dye was the tris(2,2′-bipyridyl-4,4′-carboxylate) ruthenium (II) (N3 dye). The dye is attached to the semiconductor layer by a carboxylate group [4]. To ensure effective electron injection into the semiconductor conducting band, the dye must be strongly attached to the semiconductor [4,5].

Attachment groups such as the phosphonate and carboxylate groups are required to facilitate dye adsorption onto the semiconductor layer [3]. N3 dye can absorb over a wide range of visible light 400~800 nm. A relatively new dye: tri(cyanato-2,2′,2″-terpyridyl-4,4′,4″-tricarboxylate) Ru (II) (black dye), absorbs NIR region up to 900 nm. The absorption of light by these dyes is attributed to the metal-ligand charge transfer (MLCT) transition. Other new dyes are N-719 and N-621. These dyes have been able to achieve a cell efficiency of over 10% [6-7]. The properties of dyes can be modified by incorporating different groups into the dye molecule. By choosing an optimum design, some dyes can be tuned to increase the long wavelength absorption, achieve a high extinction coefficient, and shift the energy levels to enhance the performance of the DSSC. The positions of the energy levels in the dye are important. A narrow gap between the energy levels gives the possibility to harvest more low-energy photons. Howbeit, the different electron transfers within the DSSC require enough driving force to proceed. The exited state of the dye (LUMO) must be sufficiently more negative (higher) than the conduction band edge of the semiconductor to ensure efficient injection of electrons. By the same token, the ground state of the dye (HOMO) must be more positive (lower) than the redox potential of the electrolyte redox couple for efficient regeneration of the oxidized dye [8-10]. **Figure 2.3** shows the molecular structure of N3, N621, and N719 dyes [11].

Fig. 2.3: Molecular structure of N3, N621 and N719.
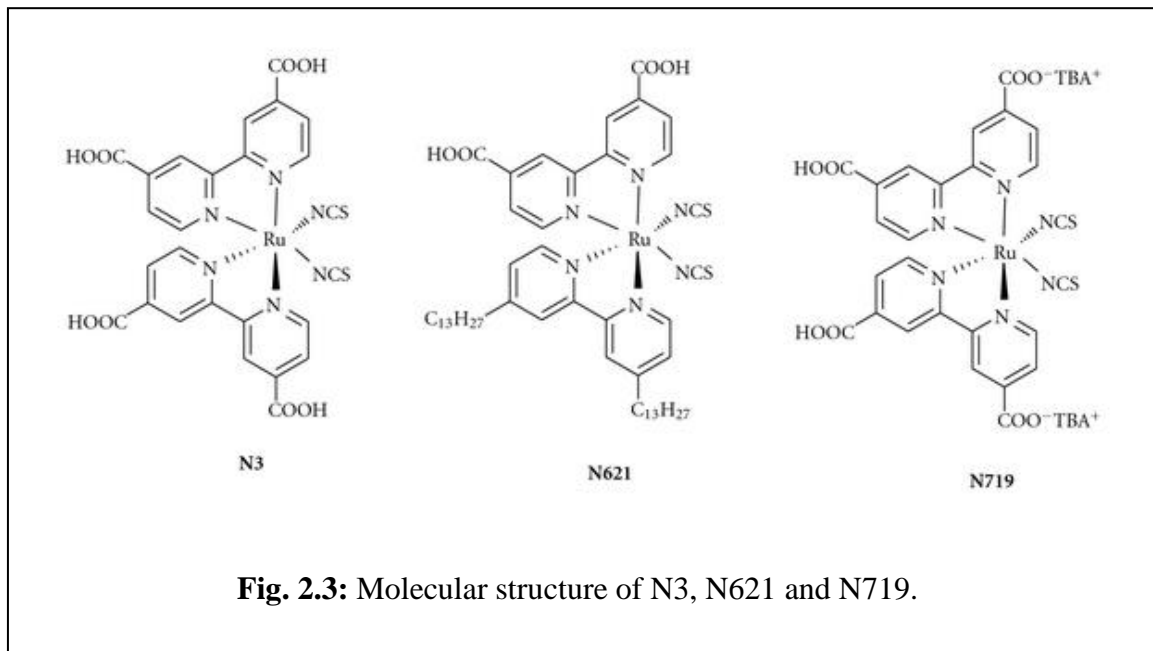
Design considerations for the dye are as follows:

i. The light absorption properties of the dye must be as wide as possible to attain a high light response.

ii. A high extinction coefficient will make the use of thinner semiconductor films (that can still keep a high amount of adsorbed dye), possible.

iii. The functional groups on the dye must be capable of binding strongly to the surface of the semiconductor for long-term stability.

iv. To ensure efficient effective charge transfer, the excited state of the dye (LUMO of the dye) must be aligned to the acceptor orbitals of the semiconductor (titanium 3d orbitals).

v. To have effective hole transfer reactions in the electrolyte medium, there is a need to tune the reduced state of the dye to the reduction potential of the redox mediator.

vi. The dye should have high chemical stability to compete with the existing technologies.

vii. The synthesis process should be easy to facilitate large-scale production.

2.2.3 Redox Electrolyte

Redox electrolytes containing I^-/I_3^- redox ions are required for dye regeneration and electron transportation between the counter electrode and the photoanode. The redox electrolyte not only contains the redox ion couple (I^-/I_3^-) but also contains small amounts of additives dissolved in an organic solvent such as acetonitrile (ACN), propionitrile, propylene carbonate, and methoxy acetonitrile [2]. The performance of the DSSC is dependent on counter cations of iodides such as R_4N^+, Li^+, K^+, and Na^+ due to different ion adsorption on the semiconductor surface or conductivity in the electrolyte, resulting in the shifting of the conduction band level of the photoanode [12-13]. Different types of electrolytes have also been tried in the DSSC. These include CuI and CuSCN [14-15] however the performance has not been comparable to that of the iodine electrolyte.

A good electrolyte should have the following properties [16-18]:

i. The ion couple potential should be less negative relative to the oxidized energy level of the photosensitizer while maintaining a substantial driving force for the regeneration of the dye

ii. The redox couple should have very slow electron recombination kinetics at the interface

iii. The redox couple should exhibit fast electron transfer at the CE

iv. The electrolyte should possess good diffusion properties for carrier transport

v. The electrolyte must be chemically inert to other compounds in the cell.

2.2.4 Counter Electrode

Normally platinum coated FTO glass substrate is used as the counter electrode of the DSSC. The Pt layer serves two purposes; a) reflecting light that passes through the film to maximize light absorption and b) catalyzes the reduction of the I_3^- ion. The I_3^- ions formed by the reduction of dye cations with I_3^- ion is reduced to $3I^-$ at the CE. High electrocatalytic activity is one of the requirements of a good CE.

2.3 Mechanism of DSSC

Figure 2.4 shows the schematic energy diagram of a DSSC. The procedure to convert photons to energy is as follows:

[1] The Ruthenium complex dye adsorbed on the semiconductor surface absorbs incident photon flux

[2] The dye is exited from the ground state (S) to the excited state (S*) as a result of the metal-to-ligand charge-transfer transition. The excited electrons are injected into the conduction band (CB) of the semiconductor, leading to the oxidation of the dye (**Eq. 1.2** and **2.2**).

$$S + hv \rightarrow S^* \tag{2.1}$$

$$S^* \rightarrow S^+ + e^-(TiO_2) \tag{3.2}$$

[3] The injected electrons in the CB of the semiconductor are transported between the semiconductor nanoparticles by diffusion towards the TCO and eventually reach the CE via an external load circuit.

[4] The oxidized dye (S$^+$) accepts electrons from the I^- redox ion and is regenerated to the ground state (S). Meanwhile I^- is oxidized to I_3^-. Two main unwanted recombination reactions ultimately lower the overall conversion efficiency of the DSSC. The excited electron in the

semiconductor can either recombine with the oxidized dye or with the oxidized redox ion couple in the electrolyte (**Eq. 2.3** and **2.3**).

(dye regeneration) $2S^+ + 3I^- \rightarrow 2S + I_3^-$ (2.3)

(recombination) $S^+ + e^-(TiO_2) \rightarrow S$ (2.4)
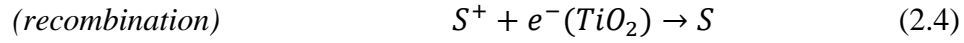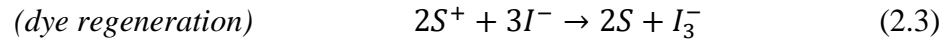
[5] The oxidized iodide ion I_3^- diffuses towards the CE where it is reduced to triiodide (**Eq. 2.5**)

$$I_3^- + 2e^- \rightarrow 3I^-$$ (2.5)
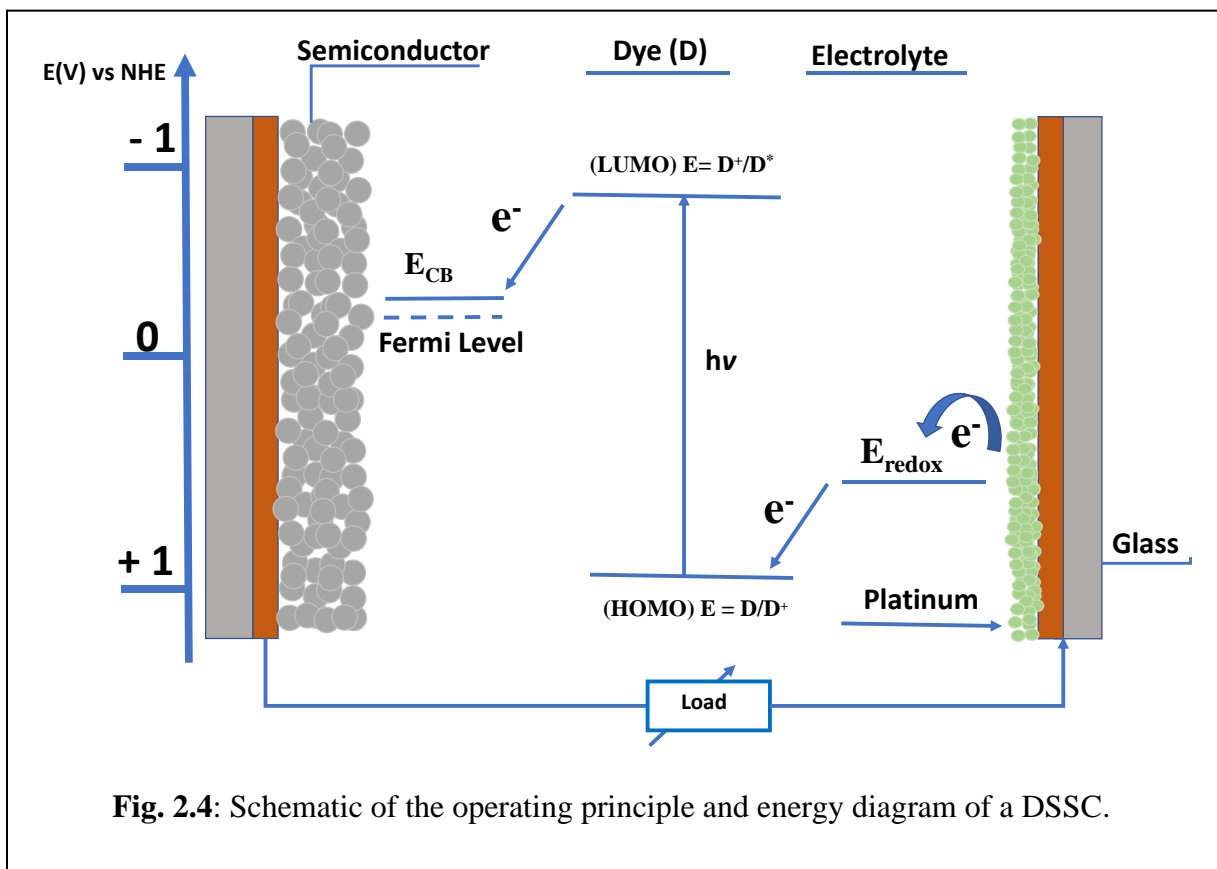
Fig. 2.4: Schematic of the operating principle and energy diagram of a DSSC.

Four energy levels of the DSSC components; a) the ground state (HOMO) b) the excited state (LUMO) c) the fermi level of the semiconductor which is situated next to the CB and d) the redox potential of the electrolyte redox ion couple (I^-/I_3^-) govern the performance of the DSSC [14, 18]. The energy difference between the HOMO and the LUMO of the dye determines the photocurrent obtained in a DSSC. The utilization of the long-wavelength region of the solar spectrum is required to generate more current density. To achieve this, the HOMO-LUMO energy gap must be small. For effective electron injection into the CB of the semiconductor, the energy level of the LUMO must be sufficiently negative relative to that of the CB of the semiconductor (ΔE_1). The HOMO level of the dye complex must be substantially more positive than the redox potential of the redox ion couple (I^-/I_3^-) to accept electrons effectively (ΔE_2). All in all, the energy gaps $\Delta E_1/\Delta E_2$, must be > 200 mV as the driving force for the electron-transfer reactions to ensure optimal efficiency [18].

2.4 Photovoltaic performance

The photovoltaic parameters of the DSSC are conducted at a light intensity equivalent to 1 sun. The term "1 sun" refers to the international standard set of light intensity conditions for solar cell measurement which is generally at A.M. 1.5 when the temperature of the cell is 25℃. A.M (air mass coefficient) refers to the path length of the solar light through the earth`s atmosphere and its angle of incident relative to the equator. A light intensity of 1 sun is equivalent to 1000 Wm^{-2}. Four main parameters are essential in calculating the efficiency of the DSSC; open-circuit voltage (V_{oc}), short-circuit photocurrent (J_{sc}), maximum power point (P_{max}), and the fill factor (FF) as illustrated in **Figure 2.5**.

Fig. 2.5: I-V characteristics of the DSSC.
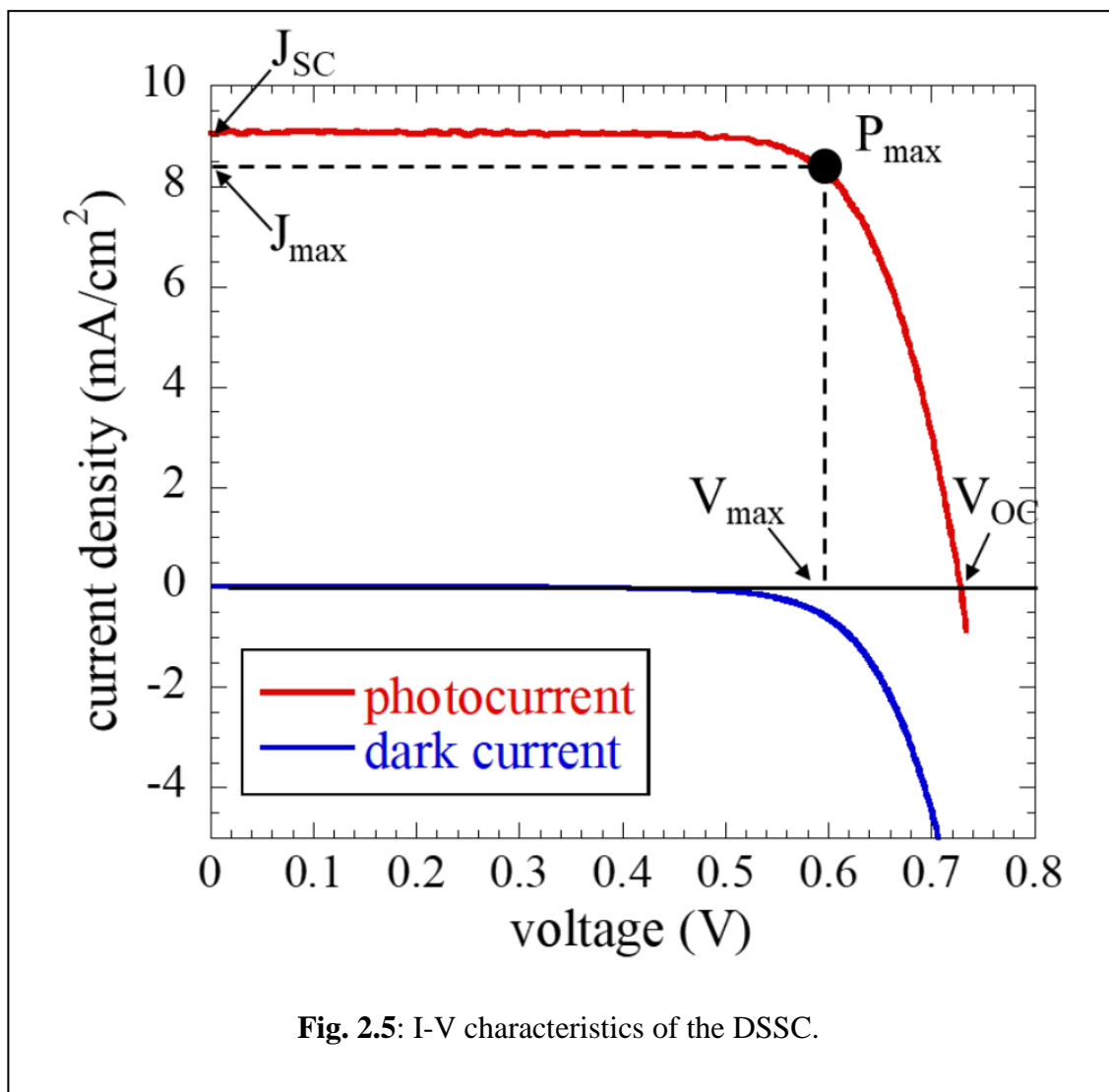
1. **Open circuit photovoltage (V_{oc}):** at the point when the output current of the cell is 0, the cell is said to be open-circuited, and the voltage of the cell is referred to as the *open circuit voltage*. Open circuit voltage is related to the difference between the quasi-fermi energy level (E_f) in the semiconductor and the chemical potential of the redox couple in the electrolyte.

2. **Short circuit photocurrent (J_{sc}):** when the output voltage is 0, the cell is said to be short-circuited. J_{sc} of the cell is equivalent to the absolute number of photons that are converted to electro-hole pairs. J_{sc} is dependent on the light intensity, optical properties of the cell, electron collection capability, and electron lifetime. J_{sc} is related to the total amount of light harvesting in the visible region of the solar spectrum by the dye.

3. **Fill Factor (FF):** is a value between 0 and 1 and is the ratio of P_{max} to the product of V_{oc} and J_{sc}. The fill factor is sometimes referred to as the "squareness" of the I-V curve as illustrated by the dotted lines in **Figure 2.5**. I_{max} and V_{max} are the current and voltage at maximum power (**Eq. 2.6**)

$$FF = \frac{I_{max}*V_{max}}{I_{sc}*V_{oc}} = \frac{P_{max}}{J_{sc}*V_{oc}} \qquad (2.6)$$

Together with the total solar power incident on the cell (P_{in}), these parameters are used to calculate the overall cell efficiency of the DSSC (**Eq. 2.7**).

$$E_{ff} = \frac{J_{sc}*V_{oc}*FF}{P_{in}} \qquad (2.7)$$

2.5 Characterization of the DSSC

2.5.1 Incident photon to current conversion efficiency (IPCE) measurement

The responsiveness of the DSSC to the solar spectrum varies with the wavelength of the incident light. IPCE measures the ratio of the number of electrons generated by the DSSC to the number of incident photons on the active surface under solar light irradiation. IPCE is also referred to as external quantum efficiency (EQE). A high EQE value at a particular wavelength means that a high percentage of the photons is absorbed by the photosensitizer in that specific region of the solar spectrum leading to electrons in the external circuit. In general, DSSCs with high IPCE over a broad wavelength exhibit high cell efficiency.

IPCE is calculated as follows (**Eq. 2.8**):

$$IPCE = \frac{1240 * J_{sc}}{\lambda * \Phi} \tag{2.8}$$

Where λ is the wavelength and Φ is the monochromatic light intensity. **Fig. 2.6** shows the spectral response of DSSC operating with black dye and N3 dye [18]. As shown in **Fig. 2.6**, Ru ion-based dyes are sensitive in the visible region of the solar spectrum.

Fig. 2.6: IPCE of DSSCs operating with black dye and N3 dye.
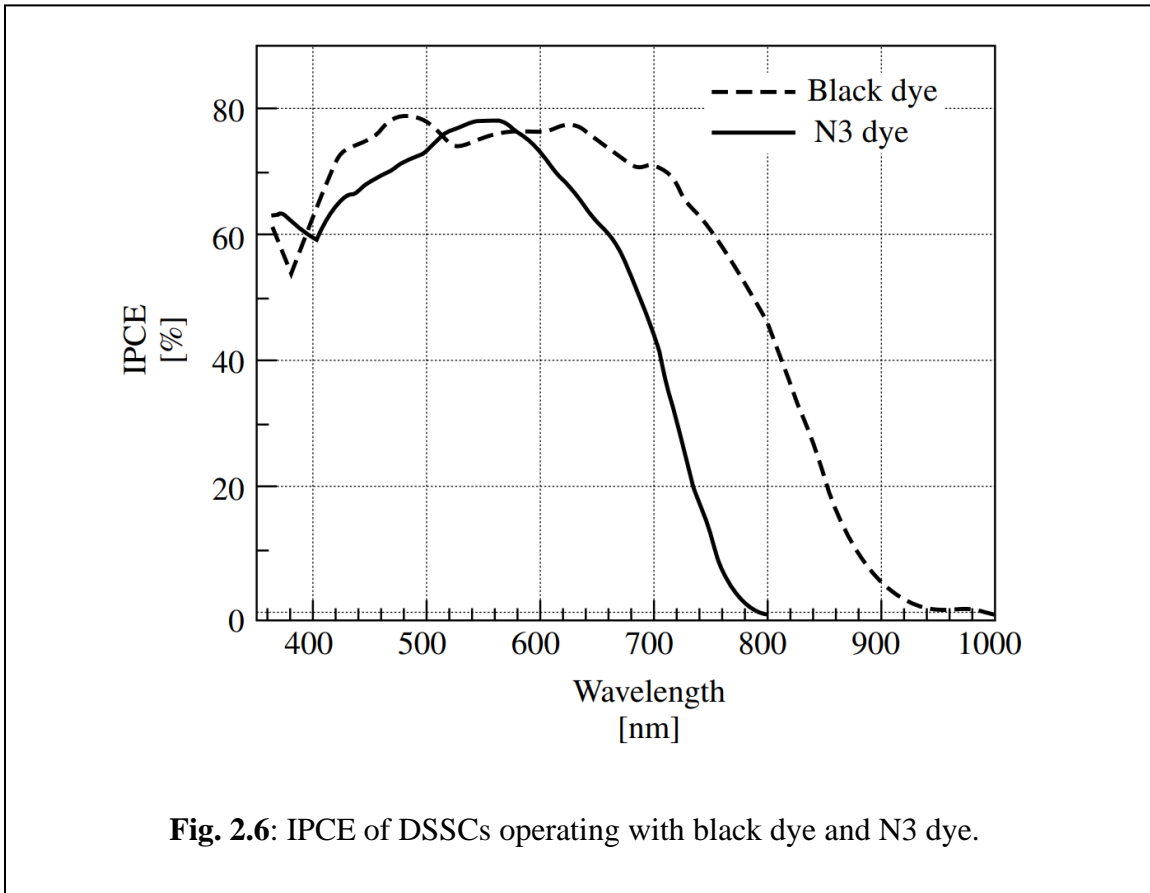
2.5.2 Electrochemical impedance spectroscopy (EIS)

EIS is a versatile technique employed in the determination of electron transfer processes at different interfaces of a DSSC. EIS measures the complex resistance to the flow of electrical current in the DSSC. EIS is measured both under illumination and under dark conditions. Under illumination, the DSSC is illuminated with a range of intensities, and impedance is measured at open circuit conditions. On the other hand, in the dark, a bias potential is applied. **Fig. 2.7** shows a typical EIS plot of a DSSC with different impedances. Z_1 is the charge-transfer impedance at the counter electrode, Z_2 is the electron recombination resistance at the semiconductor/dye/electrolyte interface and Z_3 is the diffusion resistance in the electrolyte.
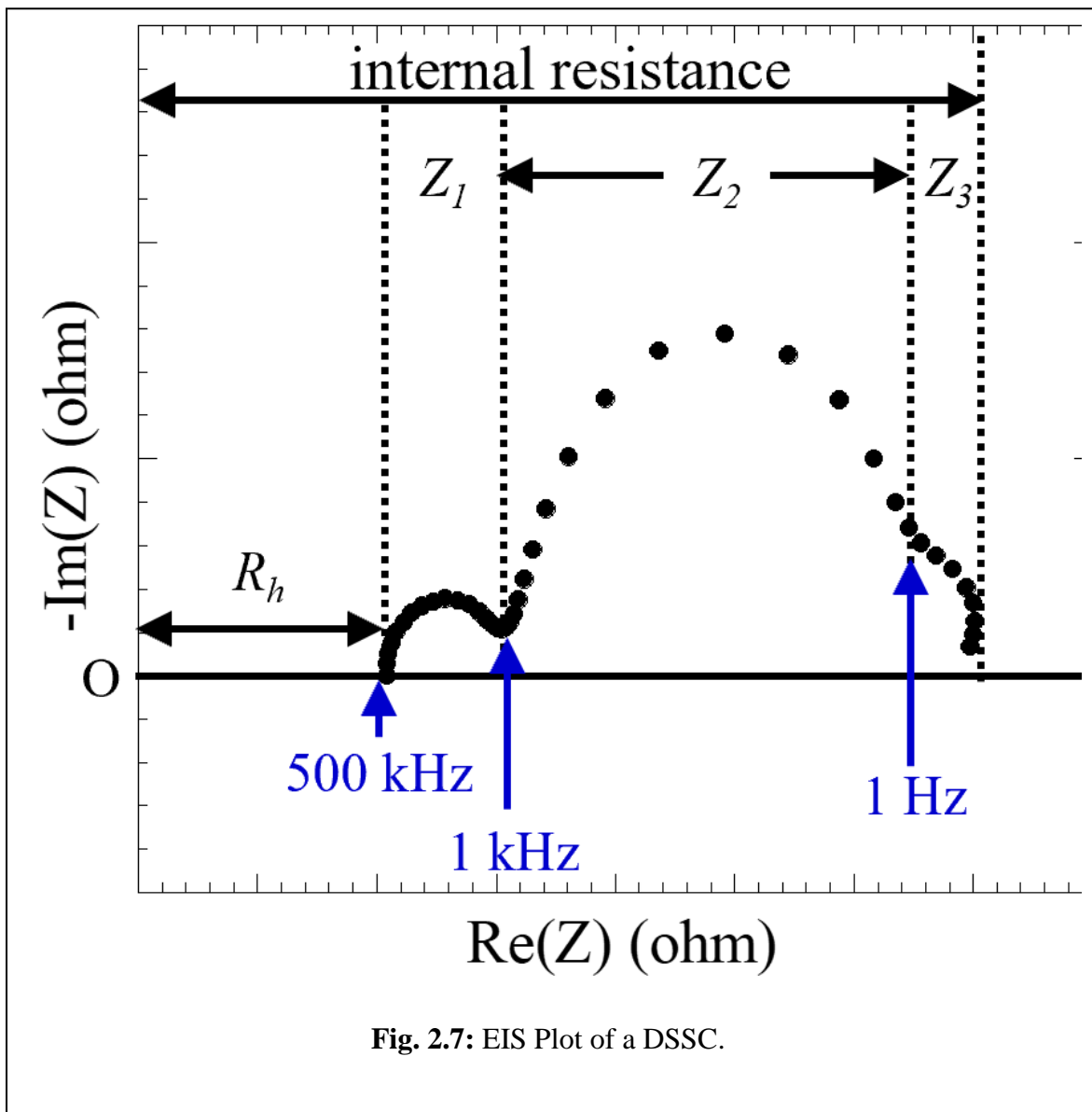
Fig. 2.7: EIS Plot of a DSSC.

2.5.3 Cyclic voltammetry

Cyclic voltammetry (CV) is a type of electrochemistry that studies electron transfer reactions on an electrode surface. CV can be used to determine the oxidation and reduction processes that the electrolyte undergoes at the CE or which the photosensitizer undergoes, both in solution and on the surface of the semiconductor. The driving force for the regeneration of the oxidized dye is determined by the oxidation potential of the sensitizer and the potential of the redox couple. There must be a balance between efficient regeneration and the loss in V_{oc}. For the sensitizer, the oxidation potential can be determined by measuring the CV of the dye in solution or adsorbed onto the semiconductor. When measuring CV, the potential is scanned and the resulting current from the electrochemical system is measured. Since the system is reversible, both the oxidation and reduction peaks appear. **Fig 2.8** shows the CV curves of DSSCs made with two different CE materials.

Fig 2.8: Cyclic Voltammetry of DSSCs made with Pt CE and PEDOT:PSS CE.
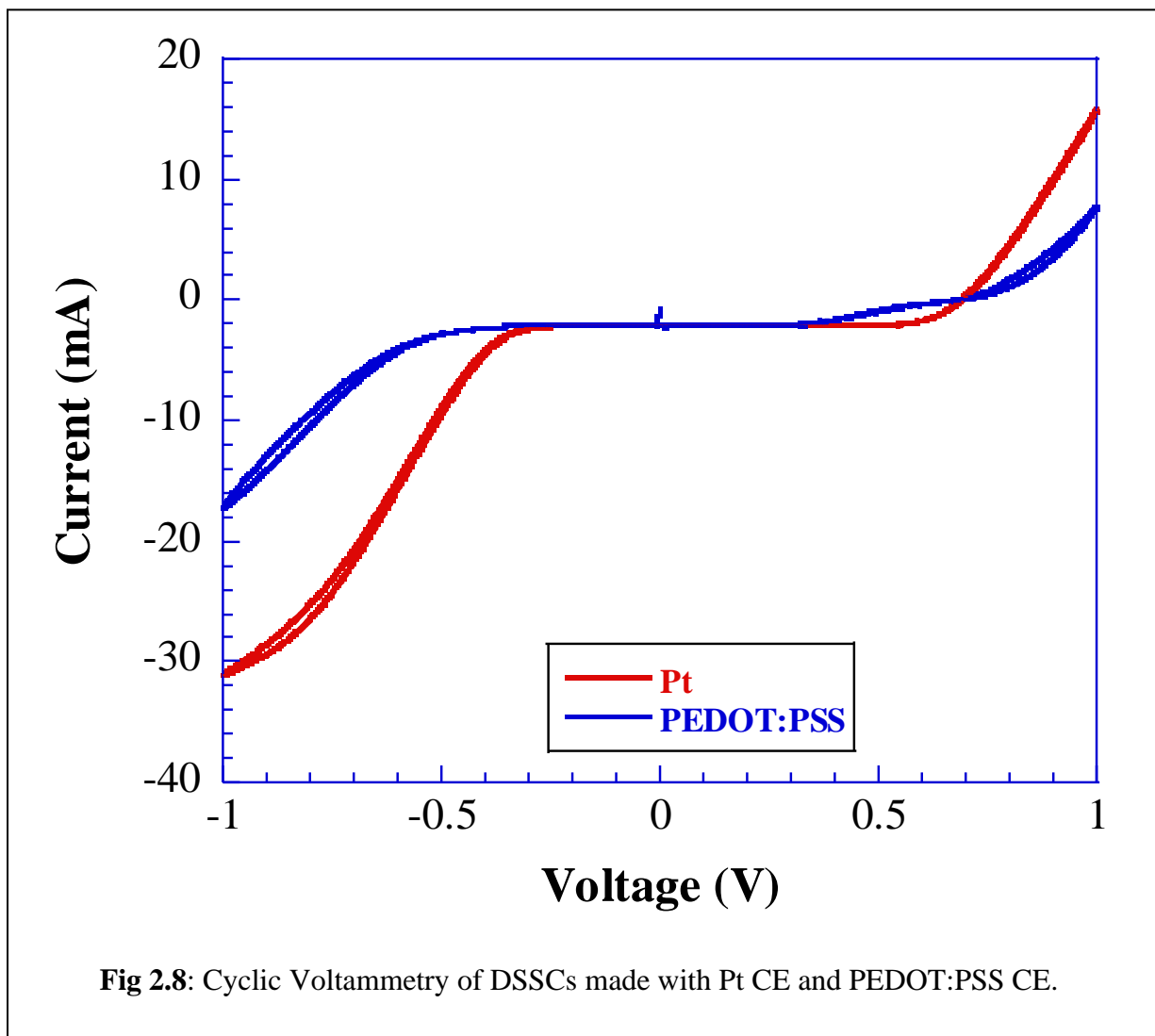
2.5 Fabrication Procedure of the DSSC

In this study, the DSSC was fabricated using the doctor blade method. Although many different materials were employed in this study and the fabrication process, the doctor blade was still the fundamental procedure in all these fabrication processes.

2.5.1 Materials

1. Fluorine-doped tin oxide (FTO) substrates, Indium doped Tin Oxide (ITO): (2cm x 1.5 cm, 2 slides for each DSSC cell) (TEC7, TEC15 Sigma-Aldrich)

2. Transparent Titanium dioxide (T/SP, TiO_2) and Reflective Titanium dioxide (R/SP, TiO_2) paste: (SOLARONIX)

3. Ruthenium-based dye solutions (N719, N749, SQ2, DN709, N3) (SOLARONIX)

4. Platinum Paste: PT1 (Dyesol)

5. Spacer:

   ➤ A 60/25 μm plastic film having dimensions of 1.4 cm^2.

   ➤ Make a square hole on the film of dimensions 1.2 cm^2.

6. Cover glass with a thickness of 0.17 mm and a diameter of 1.2 cm^2
7. Acetone, Ethanol, Deionized water (DI)
8. Liquid electrolyte
   ➤ Iodolyte AN50 0.5M with the lowest viscosity formulation for high-performance DSSCs
   ➤ Iodolyte Z-100 a 100 mM iodide/tri-iodide electrolyte synthesized with a higher boiling point solvent thus making it suitable for long-term stability assessments

Fig. 2.9: Dimensions of the spacer.
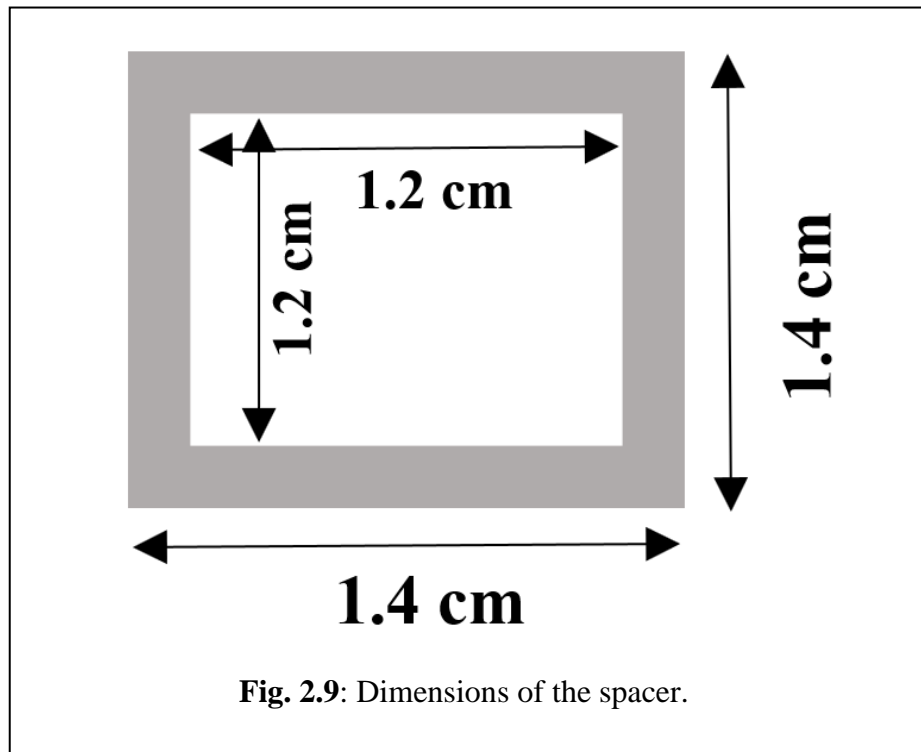
2.5.2 Tools

➢ Glass cutter, Glass drill, Slide-glass

➢ Utility knife, Pierce punch, Scoopula, mending tape

➢ Electric furnace, Ceramic hot plate, tweezers

➢ Pipets, Soldering iron, KimWipes,

➢ Mending tape with a thickness of 0.09 mm

2.5.3 Preparation of TiO₂ Photoanode

a) Cut FTO substrates to 1.5 cm x 2.0 cm using a glass cutter, section paper, and ruler. Cut the glass as smoothly as possible into a rectangular shape.

b) Sonicate the cut glass rectangles successively with acetone, ethanol, and distilled water for 20 min. **Acetone melts plastic. Therefore, it is advisable to use a glass container such as a beaker.**

c) Make a 5.5 mm hole in mending tape using a pierce punch and put it on the FTO substrate. Use a slide-glass to ensure that the mending tape has been firmly attached to the conductive side of the FTO.

d) T/SP TiO$_2$ paste is then deposited on the hole and coated on the FTO substrate. Use a slide-glass to spread the TiO$_2$ paste evenly onto the punch-holed area of the mending tape onto the FTO glass (this is referred to as the **doctor blade method**).

e) After removing the tape, the substrates and the TiO$_2$ films are sintered at 450 °C for 30 min in an electric furnace. The film is allowed to cool in the air.

f) After cooling the substrate to below 100 °C, the film is soaked in the dye solution for at least 18 hours. Use a plastic container and cover it with Aluminum foil to prevent light from entering.

g) Remove the substrate from the dye solution and rinsed lightly with ethanol and dried on the ceramic hot plate a 50 °C.

Fig. 2.10: Dimensions of the photoanode.
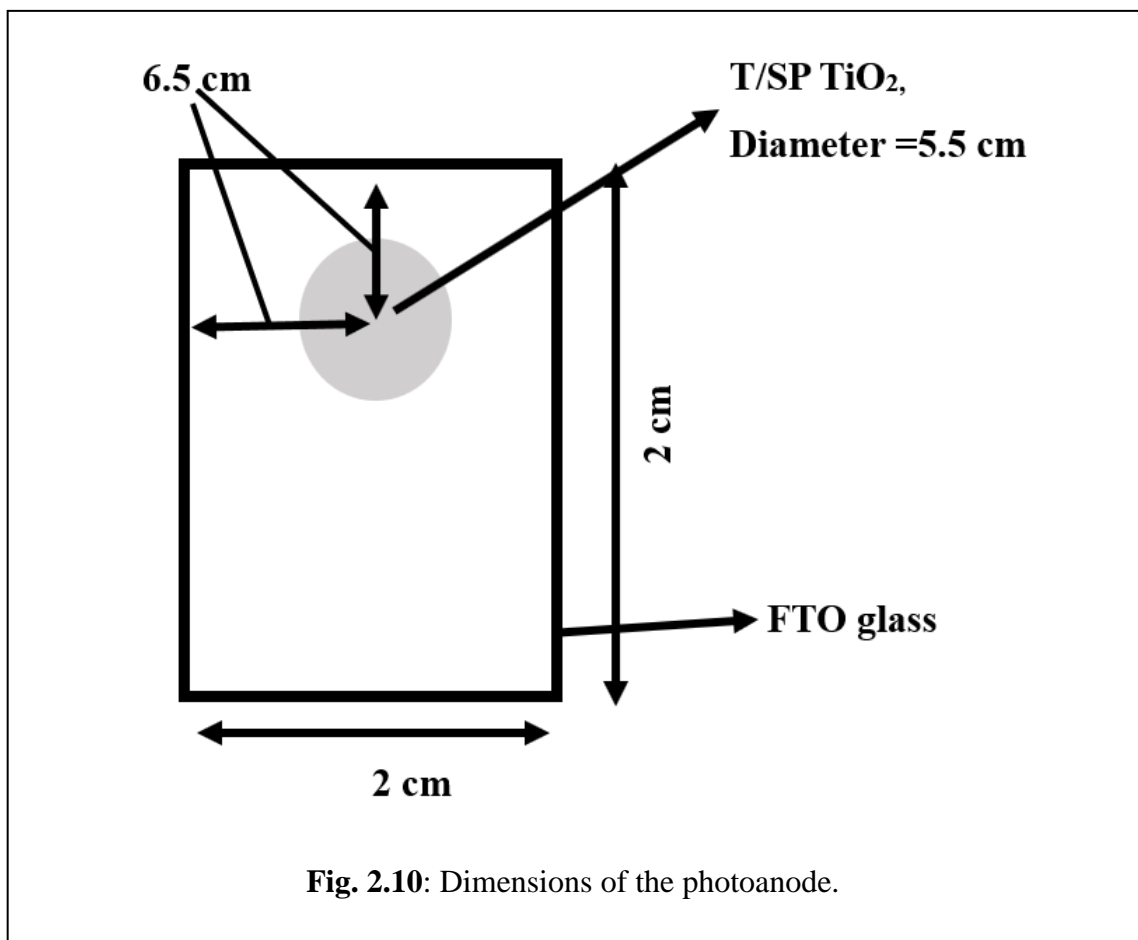
2.5.4 Preparation of platinum counter electrode

a. Cut the FTO substrates into 1.5 cm x 2.0 cm rectangles using a glass cutter, section paper, and ruler.

b. Make 2 holes in the substrate using a small glass drill with weak power, supplying water.

c. Sonicate successively with acetone, ethanol, and distilled water for 20 mins.

d. Make a 7.0 mm hole in mending tape using a pierce punch and place it on the FTO substrate. The platinum paste is then deposited on the hole and coated on FTO substrates by the doctor blade method.

e. After removing the tape, the substrate and Pt film are sintered at 450°C for 30 mins in an electric furnace.

Fig. 2.10: Dimensions of the counter electrode.
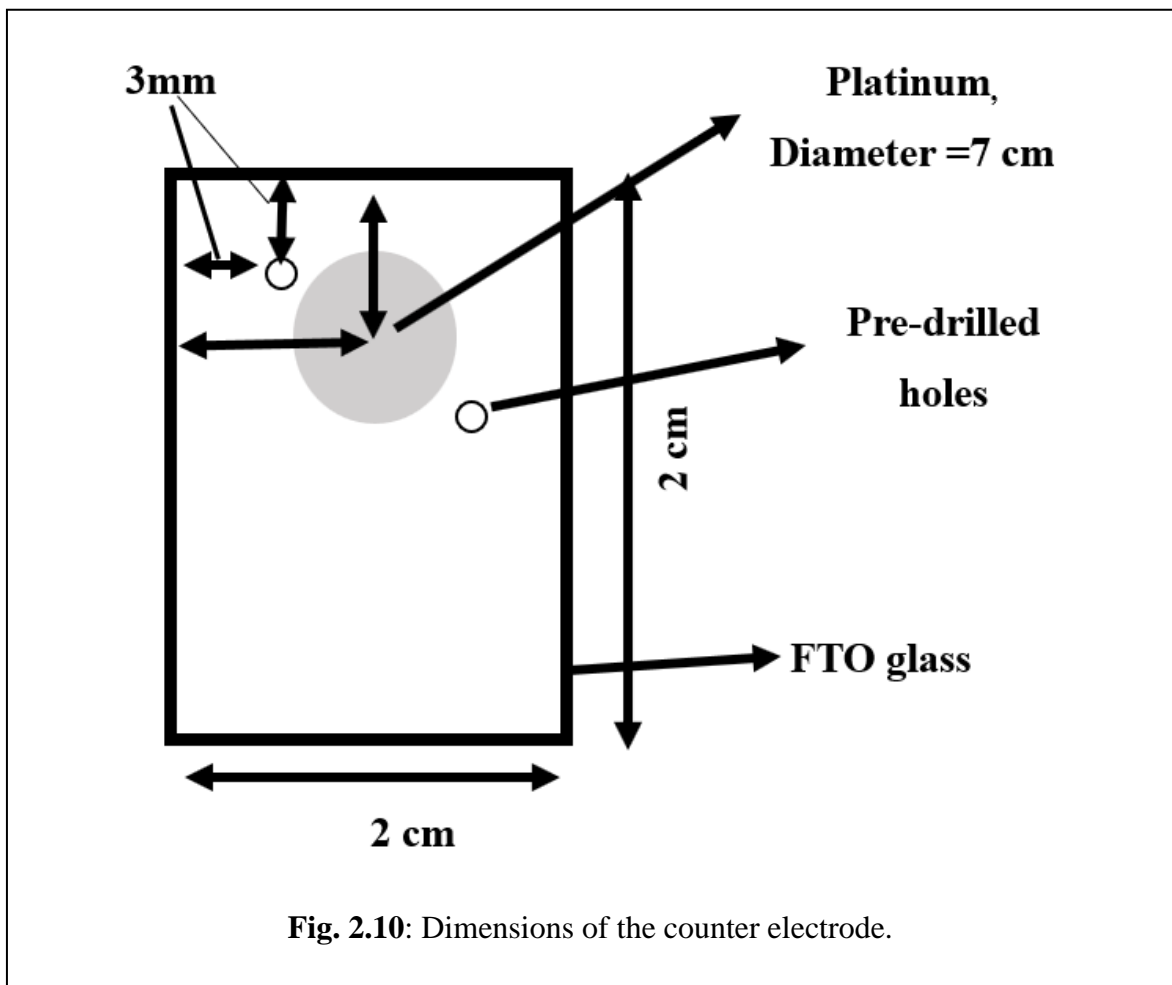
2.5.4 Fabrication of the DSSC

a) Cut the sealant as explained before and place it onto the dye-soaked photoanode

b) 2 FTO substrates, the Pt CE, and the dye-soaked photoanode are then overlapped and pressed on a hot ceramic plate at 110°C. A hot press may be utilized to press the 2 substrates until the spacer melts and firmly seals the DSSC.

c) Using a solder iron place two contacts one on the CE side and the other on the photoanode side. These contacts will ensure effective contact between the DSSC and the DSSC characterization equipment.

d) Inject the liquid electrolyte into the DSSC through the pre-drilled holes making sure that no air gaps are trapped within the DSSC.

e) Use a sealant the cover glass on the hole and seal them using a soldering iron.
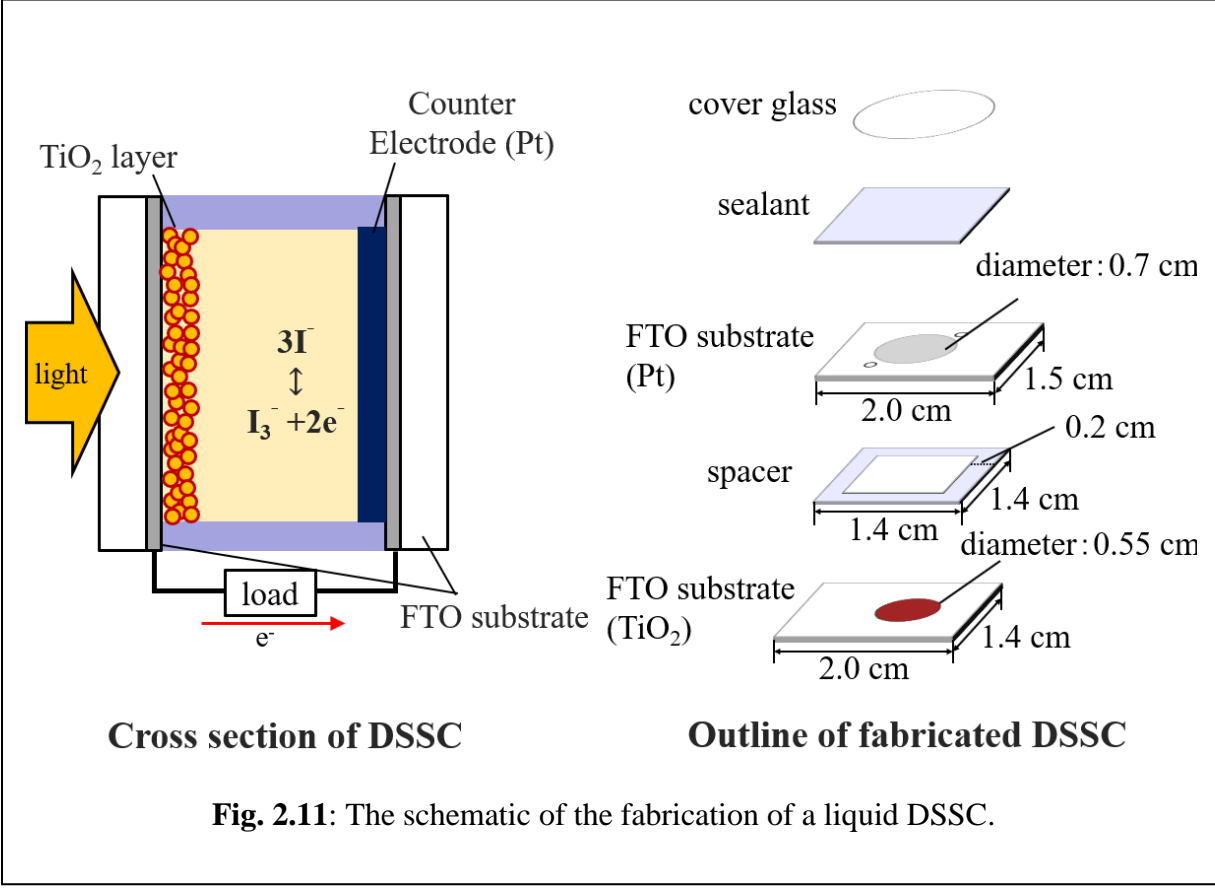
Fig. 2.11: The schematic of the fabrication of a liquid DSSC.

2.7 References

1.	B. O'Regan, M. Grätzel, Nature 353 (1991) 737–740.

2.	K. Hara, H. Arakawa, Handbook of Photovoltaic Science and Engineering, Chap 15 (2003) 663-697.

3.	Smestad G, Sol. Energy Mater. Sol. Cells 55, 157–178 (1998).

4.	Vlachopoulos N, Liska P, Augustynski J, Gratzel M, J. Am. Chem. Soc. 1988;110:1216–1220.

5.	Neil Robertson, Angewandte Chemie International Edition, 45(15):2338–2345, 2006.

6.	Md K Nazeeruddin, A Kay, I Rodicio, R Humphry-Baker, E M¨uller, P Liska, N Vlachopoulos, and M Gr¨atzel, Journal of the American Chemical Society, 115(14):6382–6390,1993

7.	Yasuo Chiba, Ashraful Islam, Yuki Watanabe, Ryoichi Komiya, Naoki Koide, and Liyuan Han,JJAP, 45(7L):L638, 2006

8.	Ooyama, Y., Harima, Y., Eur. J. Org. Chem. 2009, (18), 2903-2934. 76

9.	Mishra, A., Fischer, M. K. R., Bäuerle, P., Angew. Chem. Int. Ed. 2009, 48 (14), 2474-2499.

10.	Robertson, N., Angew. Chem. Int. Ed. 2006, 45 (15), 2338-2345.

11.	M. K. Nazeeruddin, F. De Angelis, S. Fantacci, Journal of the American Chemical Society, vol. 127, no. 48, pp. 16835–16847, 2005.

12.	Liu Y, Hagfeldt A, Xiao X, Lindquist S, Sol. Energy Mater. Sol. Cells 55, 267–281 (1998).

13.	Hara K et al., Sol. Energy Mater. Sol. Cells 70, 151–161 (2001)

14.	O'Regan B, Schwartz DT, Chem. Mater. 1995;7:1349–1354.

15.	O'Regan B, Schwartz DT, Zakeeruddin SM, Gratzel M. Adv. Mater. 2000;12:1263–1267.

16.	Kalyanasundaram K, Gratzel M, ¨ Coord. Chem. Rev. 77, 347–414 (1998).

17.	Hagfeldt A, Gratzel M, ¨ Acc. Chem. Res. 33, 269–277 (2000)

18.	A Hauch, R Kern, J Ferber, A Georg, and J Luther. 2nd World Conference and Exhibition on Photovoltaic SolarConversion, Vienna, Austria, 1998.

CHAPTER THREE: RESEARCH PLAN

3.0 Introduction

This chapter briefly outlines the research techniques and activities employed to meet the objectives of this research. The thesis plan is described below. Tasks are grouped into three phases. Each phase contains tasks that are described in this section.

3.1 System review and design (Literature review)-Phase 1

- ❖ Definition of objectives and literature review
- ❖ Analysis and interpretation of experimental data
- ❖ Extensive literature review on implementations and comparisons of existing techniques on material and manufacturing options for flexible DSSCs.
- ❖ Definition of a system and methodology
- ❖ Periodic re-evaluation of objectives - "what needs to be done and why?"

3.2 System Implementation-Phase 2

- ❖ Preliminary study on the fabrication of DSSC
- ❖ Preliminary studies on CE material synthesis using mechanical mixing technologies, chemical reactions, and spin coating techniques.
- ❖ Preliminary studies on polymer gel electrolytes synthesis using chemical-thermal and mechanical mixing techniques
- ❖ Preliminary studies on the synthesis of up converter nanomaterials using the co-precipitation methods.
- ❖ Preliminary studies on the optimization of co-dopants in the host material.
- ❖ Preliminary studies on the optimization of rare earth ion concentration in the efficient host lattice as a function of incident solar concentration and under broadband excitation
- ❖ Preliminary studies on the measurement procedures and characterization techniques used during experimental studies.

- ❖ Synthesis and characterization of films using SEM, AFM, and Raman spectroscopy.
- ❖ Evaluation of the electrocatalytic performance and internal impedance of the DSSC cell using cyclic voltammetry and Electrochemical Impedance Spectroscopy (EIS).
- ❖ Optimization of the performance of the developed photoanodes, electrolytes, and CEs through optimization of reaction parameters.
- ❖ Evaluation of the experimental data to check for any unexpected effect on the performance of DSSCs.

3.3 System Deployment (Validation and experimental integration)

- ❖ Analysis of preliminary data, discussion about formation mechanism for a full-scale study
- ❖ Integration of methodology, usable experimental procedure, and evaluation of results. This task includes all studies during the thesis.
- ❖ Evaluation of the effectiveness of DSSC developed by proper experimental processes.

3.4 Documentation

Thesis plan, journal articles, conference papers and presentations, and thesis reports.

3.5 Conclusion

In this chapter, all the necessary activities that were employed to carry out the research process have been summarized. The researcher obtained much of the information through research and observations that were related to the project.

CHAPTER FOUR: Effects of Concentrated Light on the Performance and Stability of Quasi-Solid State Electrolytes

4.0 Introduction

For the past two decades, dye-sensitized solar cells (DSSCs) have received a lot of acclamation as a suitable alternative to conventional inorganic solar cells due to their ease of fabrication, low production cost, transparency, and wide range of working temperatures [1-4]. Although the operating efficiency of DSSC remains low. Numerous studies have been conducted on improving the overall efficiency of the DSSC [5-8]. Despite these advances, most of these cells still require liquid solvents for their electrolytes [9]. The use of liquid solvents presents many challenges such as volatilization and leakage of the organic solvents, which in turn reduce the long-term stability of the DSSC [10-12]. One suggested method to address this challenge is to use polymer gel electrolytes (PGEs). PGEs exhibit suitable ionic conductivity and thermal stability [13-16], but PGEs suffer from poor penetration into the dye mesoporous semiconductor due to high viscosity [8, 16] that results in reduced cell efficiency when compared with liquid electrolyte DSSCs. To address this challenge PGEs with in-situ gelation properties were developed [17-20]. The addition of inorganic nanofillers such as SiO_2 and TiO_2 in PEGs reduces the crystalline structure of polymers and enhances redox ion transport in the electrolyte [21,25].

Another possible method to increase DSSCs efficiency is by utilizing concentrating photovoltaic systems (CPV). CPVs employ concentrating devices such as mirrors that concentrate incident sun irradiation and focus it on solar cells. The use of concentrated light enhances the performance of the cell [36-28]. However, limited research has been conducted on concentrated illumination of DSSCs [29] because the utilization of CPV systems on DSSCs presents challenges such as evaporation of the liquid electrolyte, light scattering, recombination of the electrolyte redox couple, and dye degradation in the semiconductor layer that come with the use of light concentrators [30]. Selvaraj et al. [26] combined a DSSC with a small compound concentric parabolic mirror and managed to scale up the performance of the DSSC by 4 times. In another study, Sacco et al [31], investigated the performance of DSSC under concentrated light in both indoor and outdoor settings. All studies have been done on liquid electrolyte DSSCs. To the best

of our knowledge, no study has been conducted on the use of CPVs on quasi-solid DSSCs. Therefore, in this study, we fabricated three different printable quasi-solid electrolytes. The PEO was employed as the gelation polymer, and three nanofillers (TiO$_2$, TiCN, Si$_3$N$_4$) were added to the liquid electrolyte, as described in **section 4.1.2**. Later, we explore the performance and stability of the developed printable polymer electrolytes. Moreover, we also investigated the performance and stability of both the liquid and quasi-solid electrolytes DSSCs under concentrated light illumination.

4.1 Experimental

4.1.1 Materials

TiO$_2$ pastes (T/SP), Meltonix 1170-25, and cis-dicyano-bis (2,2'-bipyridyl-4,4'-dicarboxylic acid) ruthenium (II) (N719 dye) were purchased from SOLARONIX. Platinum paste (Dyesol PT1) was purchased from Dyesol. Fluorine tin oxide doped glass substrate (FTO, 7 Ω cm^{-2}), 3-methoxypropionitrile (MPN), lithium iodide (LiI), 4-tert-butylpyridine (TBP), guanidine thiocyanate (GUSCN), poly(ethylene) oxide (M$_w$ 400,000 gmol^{-1}), TiCN (<150 nm, 97%), and TiO$_2$ <25 nm particle size, 99.98%) were purchased from Sigma Aldrich. Super dehydrated ethanol (99.5%), acetone, and Si$_3$N$_4$ (30 nm particle size) were purchased from Wako. Iso-octyphenoxy-polyethoxyethanol (TX100) was purchased from Amersham Biosciences Ltd and a concave mirror from Edmund. All materials were used as purchased without further modifications.
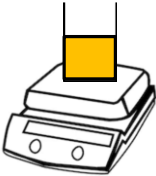
4.1.2 Preparation of the Electrolytes

To prepare the liquid electrolyte, 0.1M lithium iodide, 1M 1-butyl-3-methylimidazolium iodide, 0.1M guanidine thiocyanate, 0.1 M I$_2$, 0.5 M 4-tert-butylpyridine were dissolved in MPN. 2 wt % iso-octyphenoxy-polyethoxyethanol and 1 ml of the liquid electrolyte were added and mixed on a magnetic ceramic stirrer for 24 hr. to produce a stable uniform liquid electrolyte mixture (hereafter refers to as the liquid Iodolyte electrolyte). Further, to prepare quasi-solid printable electrolytes, 9 wt % of poly(ethylene) oxide and 10 wt% of nanoparticles like TiCN, TiO$_2$ and Si$_3$N$_4$ were mixed separately with the liquid electrolyte. The liquid electrolyte mixtures (PEO and NPs) were sequentially mixed by a conditioning mixture (AR-Thinky) at 1000 rpm and 400 rpm

for 10 and 15 min, respectively, to produce uniform Iodolyte/TiCN, Iodolyte/TiO$_2$, and Iodolyte/Si$_3$N$_4$ quasi-solid electrolytes. The quasi-electrolytes were dried at 60 ℃ in the air for 2 hr and then sealed, as shown in **Fig. 4.1**.

1. Preparation of Electrolyte Solution

Liquid Iodolyte
+
2 wt% Triton X-100
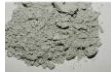
Magnetic stirrer:
- Room temperature
- 600 rpm
- 24 hrs.

2. Mixing with Nanoparticles

9 wt% PEO

10 wt% TiO_2

+

10 wt% TiCN

Electrolyte Mixture

10 wt% Si_3N_4

Mixing with a conditioning mixture (Ar-100 Thinky)
- 10 min at 1000 rpm
- 15min at 400 rpm.

3. Dying in water bath

Electrolyte solution + NPs
- Dry in a water bath at 60°C
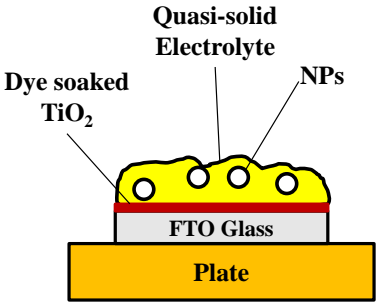
Iodolyte/TiCN

Iodolyte/TiO_2 Iodolyte/ Si_3N_4

4. Coating on photoanode

Quasi-solid Electrolyte

Dye soaked TiO_2

NPs

FTO Glass

Plate

- Doctor Blade printing

Fig.4.1: Preparation of the printable quasi-solid electrolytes.

4.1.3 Preparation of the DSSC

The FTO was used as the substrate for both the cathode and the anode. The FTO was sonicated successively in acetone, ethanol, and distilled water for 20 minutes. Subsequently, TiO_2 colloids were printed on the FTO glass and sintered at 450 ℃ for 30 mins to form transparent photoelectrode films (the active area of the photoanode was set at 0.275 cm ^{2}). Following that, films were soaked in an N-719 dye solution (4 x 10^{-4} M ethanol) for 20 hr. To prepare the CE, the platinum paste was screen printed on the FTO substrate and sintered at 450 ℃ for 30 min. To prepare the DSSC with the liquid electrolyte, the electrolyte was injected through predrilled holes on the CE, and a sandwich-type DSSC was fabricated through a sealing process with the help of a hot press [32]. For the preparation of QSDSSCs, the electrolyte was screen printed onto the dye-soaked TiO_2 layer by a doctor blade method. Following this, the photoanode and the CE were spaced by a 60 μm thermoplastic. To improve the filling of electrolytes onto the TiO_2 layer, the photoanode with the counter electrode was placed in a vacuum chamber for 10 min. Finally, the QSDSSC was sealed with the help of a hot press. The schematic depiction of DSSC fabrication is shown in **Fig. 4.2**.

4.1.4 Light Concentrating Setup

A setup to concentrate light on the DSSC is shown in **Fig. 4.2**. A concave mirror with a 50 mm radius, a focus range of 25 mm, and an aluminum coating with a R_{avg} 85%> in the 400 – 700 nm range was employed as the focusing mirror. The performance of DSSC was investigated at various vertical focal distances (*x*) (1, 2, 3, and 4 cm) from the concentrating mirror.
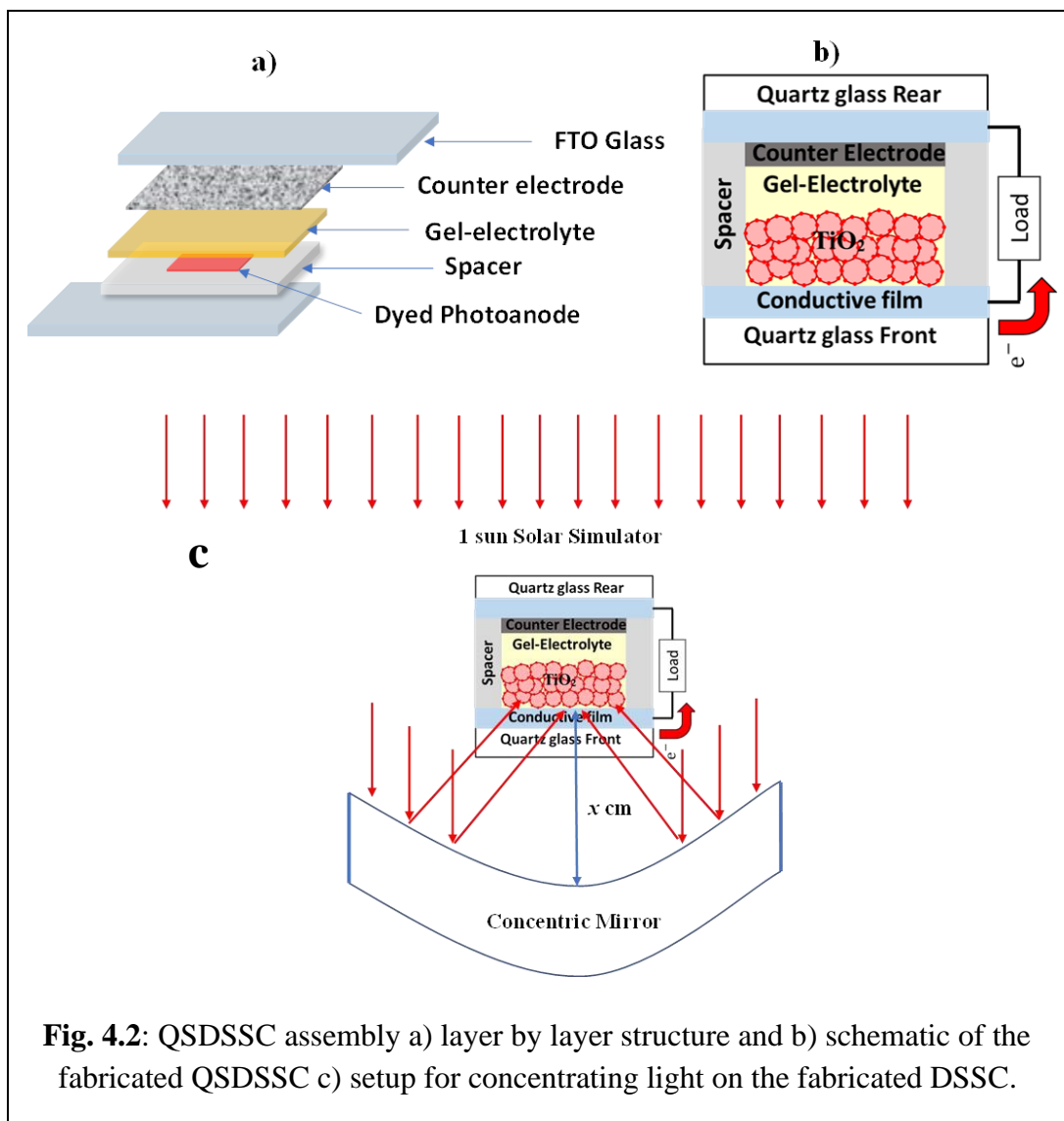
Fig. 4.2: QSDSSC assembly a) layer by layer structure and b) schematic of the fabricated QSDSSC c) setup for concentrating light on the fabricated DSSC.

4.1.5 Characterization

The structural, morphological properties and atomic composition of the prepared printable electrolyte were analyzed by a scanning electron microscope (SEM3500, Hitachi) and subjected to elemental analysis by using energy dispersion spectrometry (EDS) (EDAX, AMETEK, Octane plus). The photovoltaic characteristics of the fabricated DSSCs were obtained under 1 sun intensity (AM 1.5G, 100mWcm^{-2}). Electrochemical impedance spectroscopy (EIS: SP-150, Biologic SAS) (10 mHz to 1 MHz) was employed to measure the internal impedance of the prepared DSSCs. The incident photon to current conversion efficiency (IPCE) (in the range 300 - 800 nm of the light spectra) of the prepared DSSCs were evaluated using a Xeon arc lamp as the light source coupled with a monochromator. The temperature of the DSSC was obtained by an infrared camera (Thermo-Tracer TH7800, NEC San-ei Instruments Ltd).

4.2 Results and Discussion
4.2.1 Morphological Properties

Fig. 4.3 shows the SEM images and EDS spectra of the prepared printable electrolyte. SEM images indicate that the films were uniformly distributed over the substrate's surface and the EDS spectra indicate elements present in the electrolyte in their approximate proportions. **Figs 4.3a** and **4.3b** indicate the relatively dense and flat electrolyte surfaces of Iodolyte/TiO$_2$ and Iodolyte/TiCN, respectively. Dense and flat surfaces ensure that there is maximum contact between the CE and the electrolyte. On the contrary, **Fig 4.3c** indicates that the Iodolyte/Si$_3$N$_4$ electrolyte surface is a highly porous structure that may hinder the effective transport of ions and reduce the effective contact area with the CE.

EDS Quantitative Results

Element	Wt%	At%
CK	26.44	63.66
NK	0.34	0.69
OK	8.75	15.82
SK	1.72	1.55
IL	52.20	11.90
TiK	10.55	6.37

Iodolyte/TiO$_2$

EDS Quantitative Results

Element	Wt%	At%
CK	26.44	63.69
NK	3.02	6.24
OK	5.20	9.41
SiK	1.82	1.88
SK	1.40	1.27
IL	53.19	12.13
TiK	8.93	5.39

Iodolyte/TiCN

EDS Quantitative Results

Element	Wt%	At%
CK	22.02	48.74
NK	9.69	18.40
OK	5.42	9.00
SiK	13.10	12.40
SK	1.66	1.38
IL	48.10	10.08

Iodolyte/Si_3N_4

Fig. 4.3: SEM and EDS spectra of the prepared Iodolyte/TiO_2, Iodolyte/TiCN and Iodolyte/Si_3N_4 electrolytes.

4.2.2 Cyclic Voltammetry

To analyze the electrocatalytic activity of the solar cells, the cyclic voltammetry (CV) was set at 100 mV/s in the voltage range of -2 to 2 V [30]. The cyclic voltammograms of the DSSCs with the liquid Iodolyte, Iodolyte/TiO_2, Iodolyte/TiCN, and Iodolyte/Si_3N_4 electrolytes under 1 sun illumination at room temperature are shown in **Fig. 4.4a.** The CV curves show twin peaks- a negative and a positive peak. The positive peak indicates electrocatalytic activities between the dye and the liquid electrolyte, while the negative peak shows the interaction between the electrolyte and the CE [33, 34]. It can be observed that the peaks and shapes of the quasi-solid electrolytes have similar positions and shapes as that of the liquid electrolyte (**Fig. 4.4a**), which indicates that the quasi-solid electrolytes have the same electrocatalytic activity towards the reduction of I_3^- [35]. The DSSC with Iodolyte/TiO_2 electrolyte exhibits the highest negative and positive peaks followed by DSSC with liquid Iodolyte, on the other hand, DSSCs with the Iodolyte/TiCN Iodolyte have the lowest peak values (**Fig. 4.4a**). The higher the peak current, the more electrocatalytic active the DSSC is. On the other hand, **Fig. 4.4b** shows the CV of the DSSC with four electrolytes under concentrated light illumination. Comparing **Fig. 4.4a** and **Fig. 4.4b** shows that both negative and positive current peaks of the DSSCs with liquid Iodolyte, Iodolyte/TiO_2, Iodolyte/TiCN, and Iodolyte/Si_3N_4 electrolytes were nearly doubled under concentrated illumination, this points to an increase in catalytic activity due to increased illumination.

Fig. 4.4b: Cyclic voltammetry of the liquid and quasi-solid DSSC under 1 sun and concentrated light (3 suns).
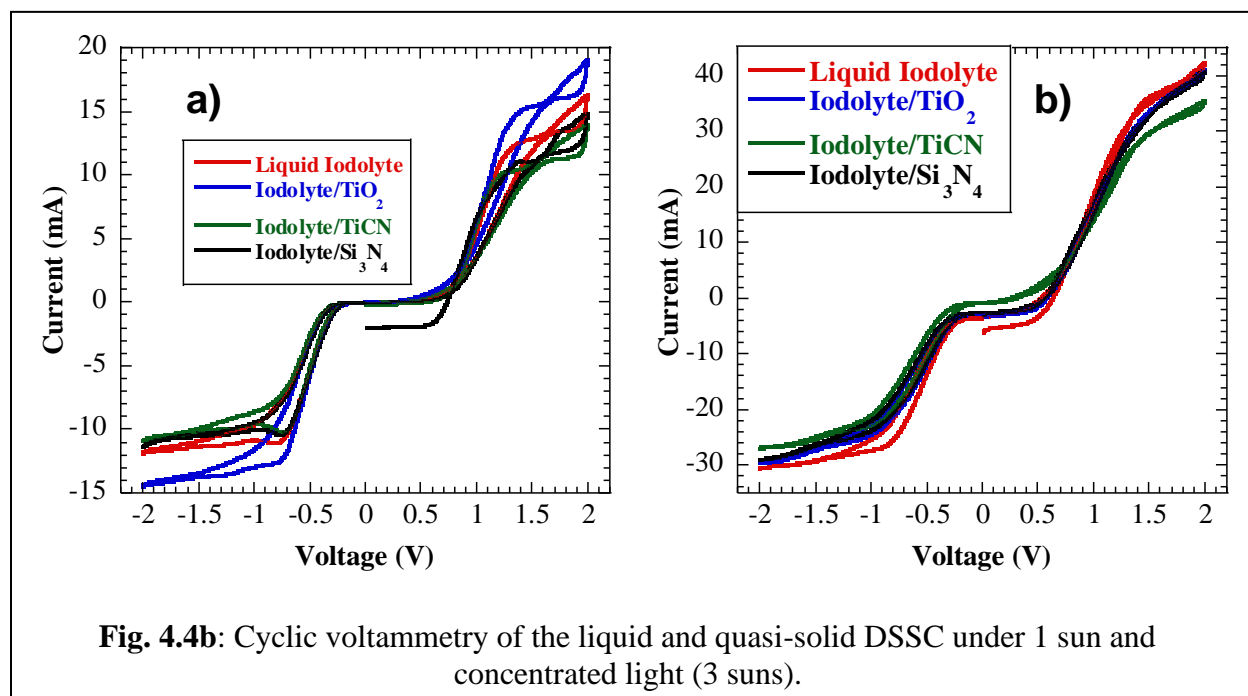
4.2.3 Electrochemical Impedance Spectroscopy

To evaluate the internal impedance of the DSSC with the four electrolytes, EIS was conducted. **Fig. 4.5** shows the Nyquist plots of the DSSCs with liquid Iodolyte, Iodolyte/TiO$_2$, Iodolyte/TiCN, and Iodolyte/Si$_3$N$_4$ electrolytes. The Nyquist plots in **Fig. 4.5a** generally show three semicircles. **Table 4.1** shows the surface resistance (R$_s$) and internal impedances of the three DSSCs under 1 sun illumination. As indicated in our previous studies [32], Z$_1$, Z$_2$, and Z$_3$ were observed under high, middle, and low frequencies [32,36].

Fig.4.5: a) EIS Nyquist plots of the DSSCs under 1 sun illumination and b) EIS under concentrated illumination.
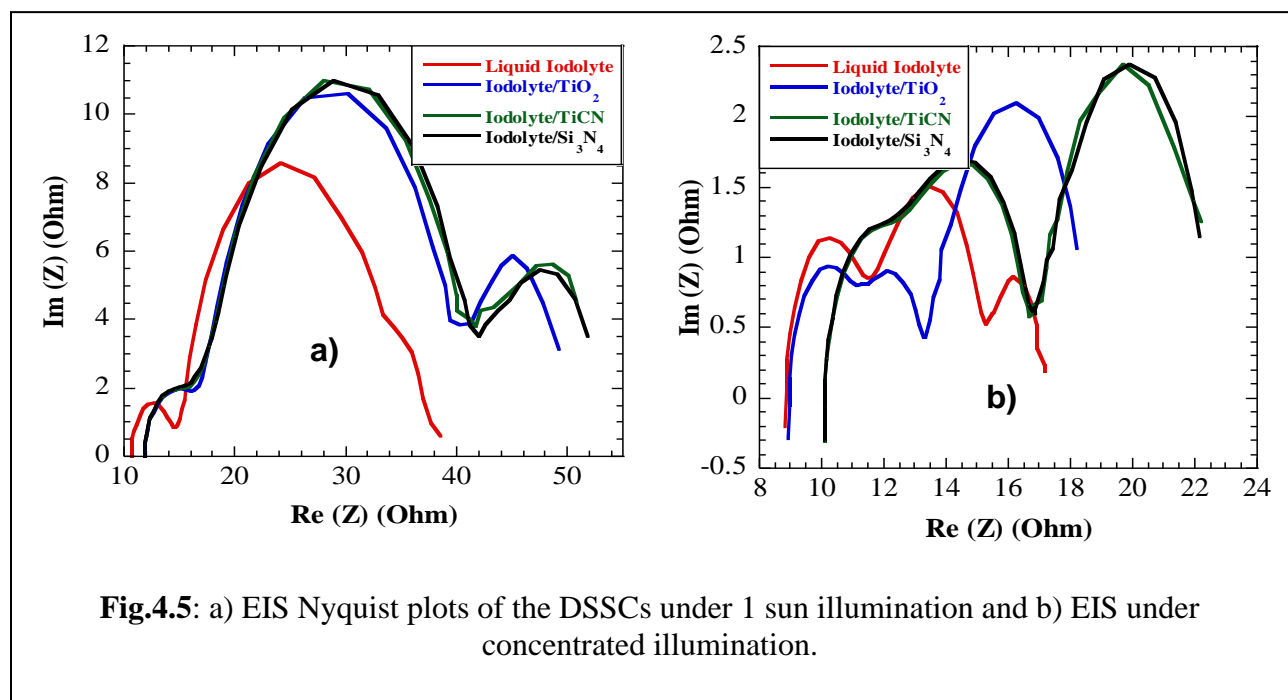
Table 4.1 indicates the Z_1 resistances of the DSSC with Liquid Iodolyte resistance (3.584 Ω) are lower than that of the DSSCs with Iodolyte/TiO$_2$ (4.274 Ω), Iodolyte/TiCN (4.904 Ω), Iodolyte/Si$_3$N$_4$ (4.546 Ω) electrolytes. This suggests that the DSSC with the liquid Iodolyte electrolyte exhibits better electrocatalytic activity at the CE/electrolyte interface due to the reduced surface interaction between the quasi-solid electrolyte and the Pt CE. On the contrary, the Z_2 resistances of the DSSCs with Iodolyte/TiO$_2$ (25.98 Ω), Iodolyte/TiCN (27.88 Ω), and Iodolyte/Si$_3$N$_4$ (27.93 Ω) electrolytes were significantly higher than that of the DSSC with the Liquid Iodolyte electrolyte (21.09 Ω). High Z_2 resistances were due to lower charge recombination at the photoanode/electrolyte interface [12,36]. Additionally, this indicates faster electron transfer between the quasi-solid electrolyte and the photoanode, supported by the lower dark currents exhibited by the DSSCs with quasi-solid electrolytes in **Fig. 4.6b**. The lower dark current of the DSSCs with quasi-solid electrolytes was due to the possible suppression of electron recombination with the addition of nano-fillers and polymers into the liquid electrolyte [20]. The Z_3 resistances with quasi-solid electrolytes were lower than the liquid Iodolyte electrolyte in DSSC. It means that there was facilitated transport of I_3^- ions through the part developed by the addition of nanoparticles [37,38]. Moreover, **Fig. 4.5b** shows the EIS of the fabricated DSSCs at

concentrated illumination. **Table 4.2** shows the surface resistances and internal impedance of the fabricated DSSCs under concentrated illumination. From comparing the **Figs. 4.5a** and **4.5a** it can be observed that there was a significant decrease in dynamic impedances of the DSSCs. The reduction in dynamic resistance of the DSSC was attributed to the increase in light intensity [39].

Table 4.1: Surface resistance and impedance values of the fabricated DSSCs at 1 sun illumination.

Electrolyte	R_s (Ω)	Z_1	Z_2	Z_3
		Resistance (Ω)	Resistance (Ω)	Resistance (Ω)
		Capacitance (μF)	Capacitance (μF)	Capacitance (mF)
Liquid Iodolyte	11.02	3.584	21.09	18.94
		2.852	739.1	5.64
Iodolyte/TiO_2	12.01	4.274	25.98	8.892
		6.174	188.9	56.3
Iodolyte/TiCN	12..03	4.904	27.88	14.32
		6.639	119.3	51.2
Iodolyte/Si_3N_4	12.00	4.546	27.93	11.84
		4.871	119.1	42.2

Table 4.2: Surface resistance and impedance values of the fabricated DSSCs under concentrated illuminationation.

Electrolyte	R_s (Ω)	Z_1	Z_2	Z_3
		Resistance (Ω)	Resistance (Ω)	Resistance (Ω)
		Capacitance (μF)	Capacitance (μF)	Capacitance (mF)
Liquid Iodolyte	8.94	2.865	4.005	1.843
		2.429	261.6	57.9
Iodolyte/TiO_2	8.98	2.748	3.407	5.615
		3.726	96.65	60.7
Iodolyte/TiCN	8.97	2.884	3.711	5.696
		3.550	105.8	59.7
Iodolyte/Si_3N_4	8.98	2.787	3.601	5.662
		3.674	91.46	60.3

4.3 Photovoltaic Characterization of the fabricated DSSC under 1 sun illumination

The J-V curves of the fabricated DSSCs under I sun illumination and at the room, temperatures are shown in **Fig. 4.6a**. The short-circuit current density (J_{sc}), open-circuit voltage (V_{oc}), fill factor (FF), and overall cell efficiency (E_{ff}) of the fabricated DSSCs, are listed in **Table 4.3.** The DSSC with the liquid Iodolyte electrolyte had an optimal cell efficiency of 4.59 % (J_{sc} = 8.823 mA/cm^2, V_{oc} = 0.73 V, FF = 0.71). On the other hand, the DSSC with the Iodolyte/Si$_3$N$_4$ electrolyte yielded an optimal E_{ff} of 4.6% (J_{sc} = 8.354 mA/cm^2, V_{oc} = 0.77 V, FF = 0.71) while the DSSCs with Iodolyte/TiCN had a cell E_{ff} of 4.66% (J_{sc} = 8.4874 mA/cm^2, V_{oc} = 0.77 V, FF = 0.72). Lastly, the DSSC with the Iodolyte/TiO$_2$ electrolyte yielded an optimal E_{ff} of 5.02 % (J_{sc} = 9.5608 mA/cm^2, V_{oc} = 0.76 V, FF = 0.69). The E_{ff} of the DSSC with the liquid Iodolyte, Iodolyte/TiCN, and Iodolyte/Si$_3$N$_4$ electrolytes was almost similar. Whereas DSSC with the Iodolyte/TiO$_2$ electrolyte had a significantly higher E_{ff} than other electrolytes. The higher catalytic activity and reduced Z_2, and Z_3 impedances of the Iodolyte/TiO$_2$ quasi-solid DSSCs were due to the intrinsic properties of the TiO$_2$ nanofillers [44]. The high J_{sc} of the DSSC with Iodolyte/TiO$_2$ electrolyte reflects faster I^-/I_3^- interconversion and faster dye regeneration kinetics [39]. From **Table 4.3**, it can be noted that DSSCs with quasi-solid electrolytes have higher V_{oc} values. The higher V_{oc} value of the DSSCs with quasi-solid electrolytes was ascribed to both the upward shift of the conduction band (CB) edge as well as the higher recombination resistance (Z_2) at the photoanode/electrolyte interface [16]. This is also supported by the dark currents of the DSSCs, as shown in **Fig. 6b**.
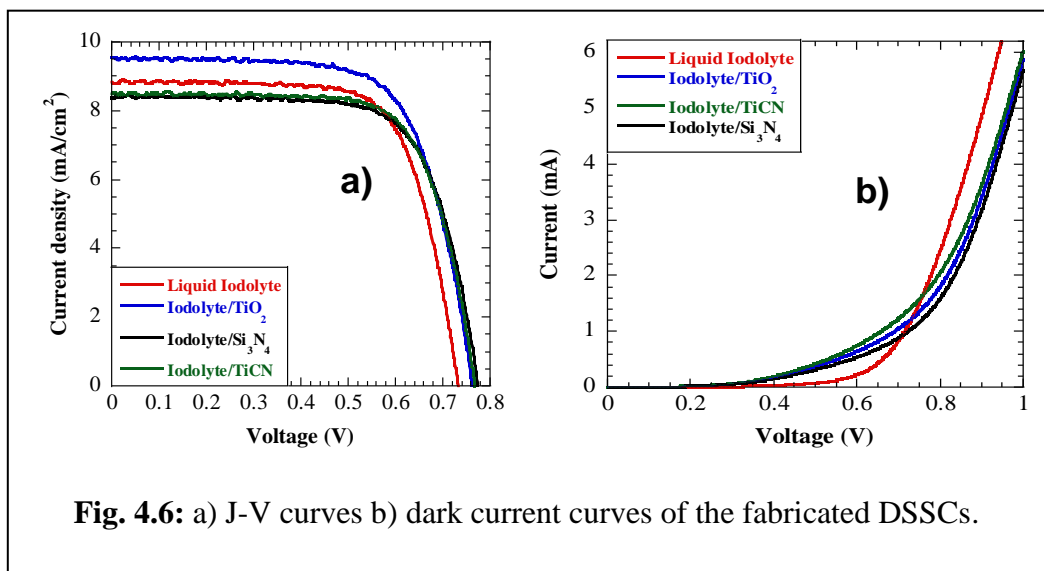
Fig. 4.6: a) J-V curves b) dark current curves of the fabricated DSSCs.

Fig. 4.7a, shows the IPCE curves of the DSSCs with various electrolytes in the 300-800 nm range. All DSSCs show similar shapes because they all employ a similar dye (N-719). The DSSCs with the quasi-solid electrolytes exhibited higher IPCE values as compared to the DSSC with the liquid electrolyte. This may be due to the enhanced light-scattering abilities of the nanofillers [12]. This result indicates that IPCE could be one of the factors contributing to the enhanced performance of the QSDSSCs. The stability of the DSSCs with various electrolytes under dark conditions was shown in **Fig. 4.7b**. The performance of all DSSCs diminished with time, however, the rate of degradation for the DSSC with the liquid Iodolyte electrolyte is faster than that of the QSDSSCs (see **Fig. 4.7b**). As a result, QSDSSCs exhibit better durability than the DSSC with the liquid Iodolyte electrolyte. This predominant stability can be ascribed to the 3D frame formed by the nanofillers and the polymers that prevent the evaporation and leakage of the electrolyte [20].

Table 4.3: Photovoltaic parameters of the fabricated DSSC under frontal illumination.

Electrolyte	Illumination	Voc[V]	Jsc [A/m^2]	FF	Eff [%]
Liquid Iodolyte	Front	0.73	8.823	0.71	4.59
Iodolyte/TiO$_2$	Front	0.76	9.561	0.69	5.02
Iodolyte/TiCN	Front	0.77	8.487	0.72	4.66
Iodolyte/Si$_3$N$_4$	Front	0.77	8. 354	0.71	4.60
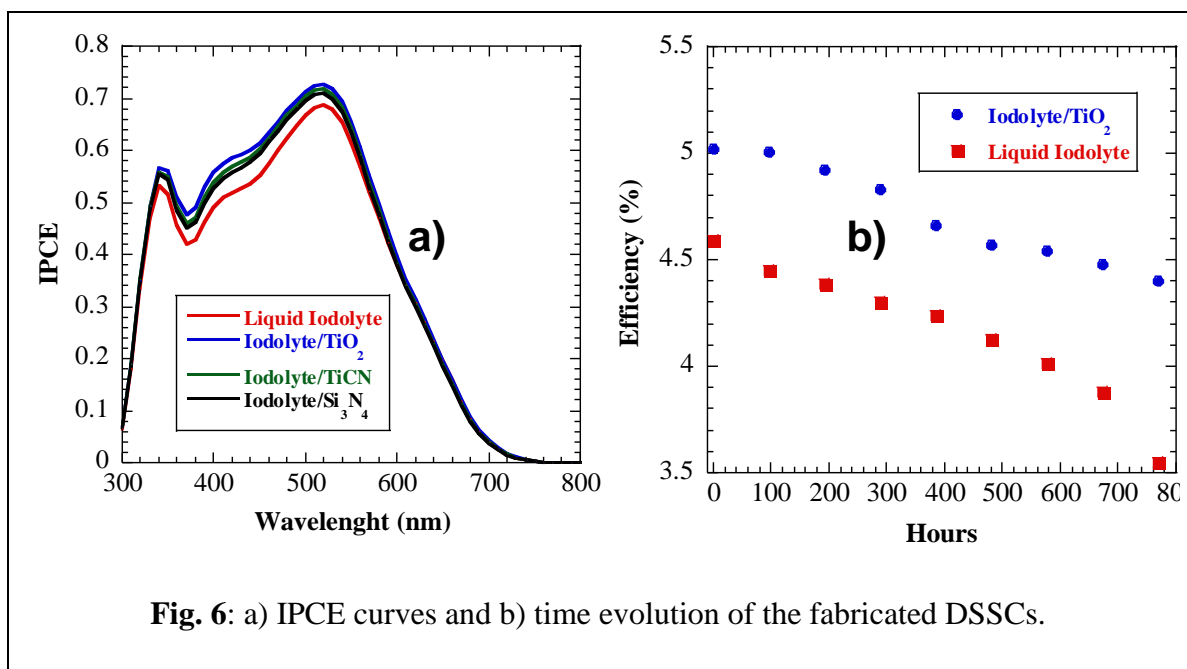
Fig. 6: a) IPCE curves and b) time evolution of the fabricated DSSCs.

4.4 Photovoltaic Characterization of the fabricated DSSC under concentrated light (3 suns)

4.4.1 Effects of focal distance on the performance of the DSSC

To determine the optimal focal distance from the concave mirror the J-V characteristics of the DSSC was recorded as the vertical distance from the center of the concave mirror to the photoanode layer was adjusted from 1 – 4 cm. **Fig. 4.8** shows the performance of the DSSCs against the vertical distance from the center of the concave mirror, and it was observed that performance of the QSDSSC increases as the distance was increased from 1 to 2.5 cm. However, a further increase in distance results in a decrease in efficiency because the focal point was located at a vertical distance of ~ 2.5 cm from the center of the concave mirror.
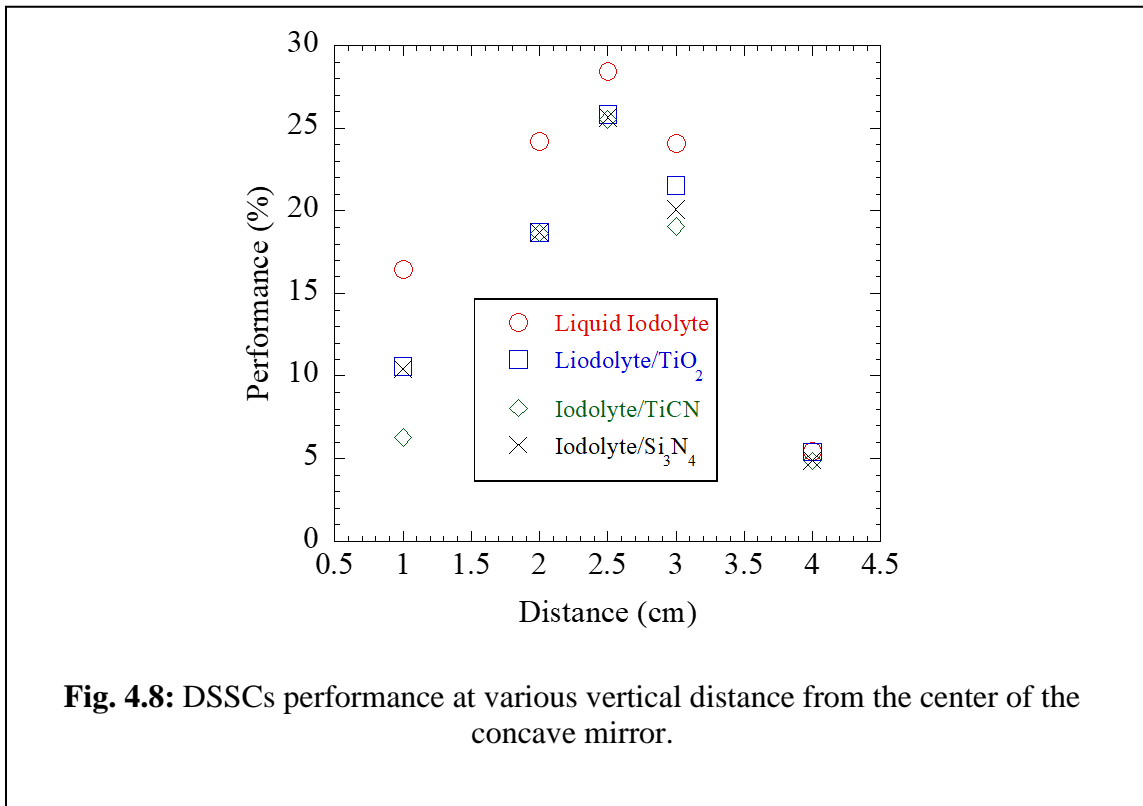
Fig. 4.8: DSSCs performance at various vertical distance from the center of the concave mirror.

4.4.2 Performance at the focal distance of 2.5 cm

Fig. 4.9 shows the photovoltaic properties of the DSSCs employing the liquid Iodolyte and Iodolyte/TiO$_2$ electrolyte measured at the focused position of the concentric concave mirror. The photovoltaic parameters of the fabricated DSSC under concentrated illumination were shown in **Table IV**. It was observed from **Table 4.4** that DSSC with the liquid Iodolyte electrolyte exhibited a remarkably high J$_{sc}$ of 100.14 mA/cm^2 and an overall system efficiency (E$_{sys}$) of 28.44%, which is an enhancement of ~6.2 times its performance under I sun illumination. The DSSCs with the Iodolyte/TiO$_2$ electrolyte achieved an E$_{sys}$ of 25.84 % (J$_{sc}$ = 80.31 mA/cm^2), which enhances efficiency ~ 5.1 times. The QSDSSCs with the Iodolyte/TiCN and Iodolyte/Si$_3$N$_4$ electrolytes exhibited almost similar E$_{sys}$ and J$_{sc}$ values to that of the Iodolyte/TiO$_2$ QSDSSC. From these results, it is noticeably clear that DSSCs coupled to a concentric mirror perform significantly better than those that are not coupled to a concentric mirror. The increased J$_{sc}$ and overall cell performance can be attributed to the increase in illumination due to the light-focusing effects of the concentric mirror. This effect is like that of the Silicon solar cells, the V$_{oc}$ of the DSSC increases logarithmically with an increase in irradiation intensity according to **Eq. 4.1**.

$$V_{oc}^{`} = V_{oc} + \frac{nkT}{q} In\, X \qquad\qquad (4.1)$$

Where *X* in the solar irradiation intensity [26]. The high J$_{sc}$ value of the liquid Iodolyte DSSC was mainly due to its high transmittance, which facilitates more photons to reach the dye. On the other hand, the performance of the QSDSSC is slightly decreased owing to their reduced transmittance due to the presence of nanofillers and polymers.

This study showed that DSSC was subjected to continuous focused light soaking for 120 mins (**Fig. 4.2**). Under continuous focused light, the temperature of the DSSC changes with an increase in soaking time as shown in **Table 4.4**. **Fig. 4.9a** shows the change in E$_{sys}$ of the DSSCs as a function of light soaking time. It was observed that E$_{sys}$ decreases with an increase in light soaking time. However, the rate of E$_{sys}$ for Iodolyte/TiO$_2$ QSDSSC decreases significantly slower compared to that of the liquid Iodolyte DSSC. The Iodolyte/TiO$_2$ DSSC still retains ~91.4% of its initial E$_{sys}$ after 120 min, on the contrary, the liquid Iodolyte DSSC manages to retain only

~73.2% of its initial E_{sys} value. As soaking time under focused light increases, the temperatures of the DSSCs also increase such that after 120 mins, both the liquid Iodolyte DSSC and the Iodolyte/TiO$_2$ reach a high temperature of ~ 98℃. The rate of evaporation and leakage of the liquid electrolyte increases with temperature due to poor DSSC sealing conditions [39]. As expected, the performance of the liquid Iodolyte DSSC will be diminished owing to the loss of electrolytes due to high temperature.

On the other hand, there was a slight decrease in E_{sys} of the Iodolyte/TiO$_2$ DSSC with an increase in light soaking time, and no significant physical changes were observed on the DSSC that indicate the loss of electrolyte. The decrease in E_{sys} is attributed to the increase in the rate of electron recombination at the electrolyte/photoanode interface at a significantly higher temperature of the DSSC [39,26]. The effects of light soaking time on the J_{sc} of the DSSCs were illustrated in **Fig. 4.9b**. There was a gradual increase in the J_{sc} of the Iodolyte/TiO$_2$ DSSC with an increase in light intensity. The high J_{sc} values of QSDSSCs at high light irradiation point to a possibility of enhanced charge transport within the Iodolyte/polymer/TX100 electrolytes [6].

Additionally, in **Fig. 4.9c** while the *FF* of the liquid Iodolyte DSSC is gradually increasing, the *FF* of the QSDSSC gradually decreases with an increase in soaking time. In a liquid DSSC, increasing temperature leads to a reduction in recombination resistance. With an increase in temperature, the rate of photon generation increases, which causes reverse saturation current to increase rapidly, reducing the bandgap. This results in significant changes in J_{sc} and smaller changes in V_{oc} of the DSSC. At higher temperatures, the decrease in recombination resistance and V_{oc} coupled with a loss of electrolyte leads to changes in the *JV* curve, reduction of cell efficiency, and a small increase in *FF*. The decrease in *FF* of the QSDSSC is ascribed to the decrease in V_{oc} and the rate of electron recombination, which increases with long light irradiation and elevated temperatures. The decrease in V_{oc} shown in **Fig. 4.9d** was mainly attributed to the rise in temperature [26].

Fig. 4.9: Time evolution performance parameters of the liquid Iodolyte and Iodolyte/TiO$_2$ DSSCs under concentrated light soaking.
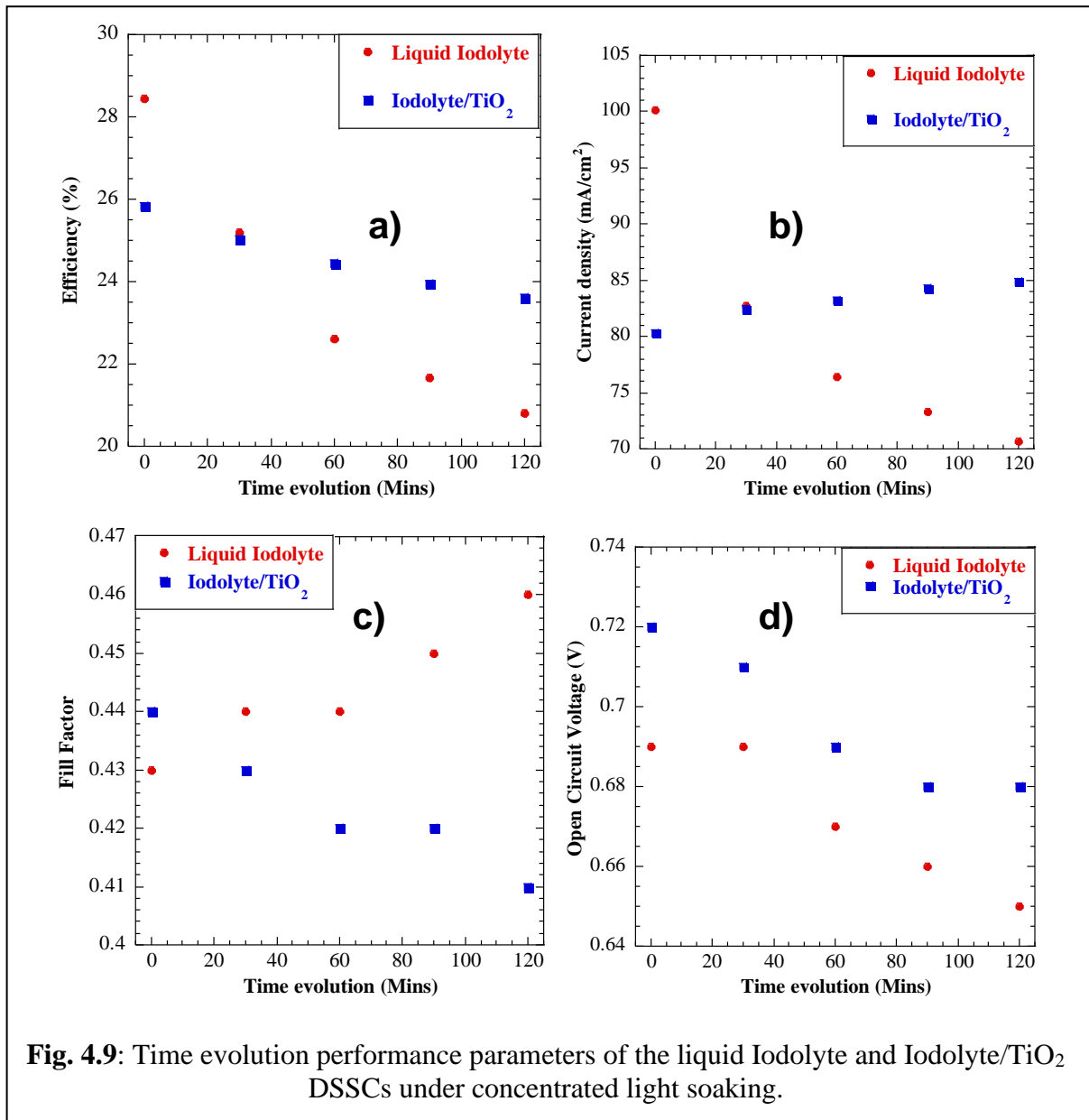
Fig. 4.10 shows the IPCE of the SQDSSCs at room temperature and the IPCE after 120 mins of continuous light soaking. **Fig. 4.10a** shows the IPCEs of the Iodolyte/TiO$_2$ QSDDSC. The results show a slight increase in IPCE after continuous light soaking. This has been attributed to the increase in the contact between the electrolyte and the photoanode after the quasi-solid polymer had been subject to heat and then finally cooled. On the other **Fig 4.10b** shows the IPCE of the

Iodolyte/TiCN under similar conditions. The results show a slight decrease in IPCE after continuous light soaking. This result has been attributed to the degradation of the Iodolyte/TiCN nanoparticles under continuous light soaking.

Fig. 4.10: a) IPCE of a) Iodolyte/TiO$_2$ and b) TiCN before and after continuous light soaking
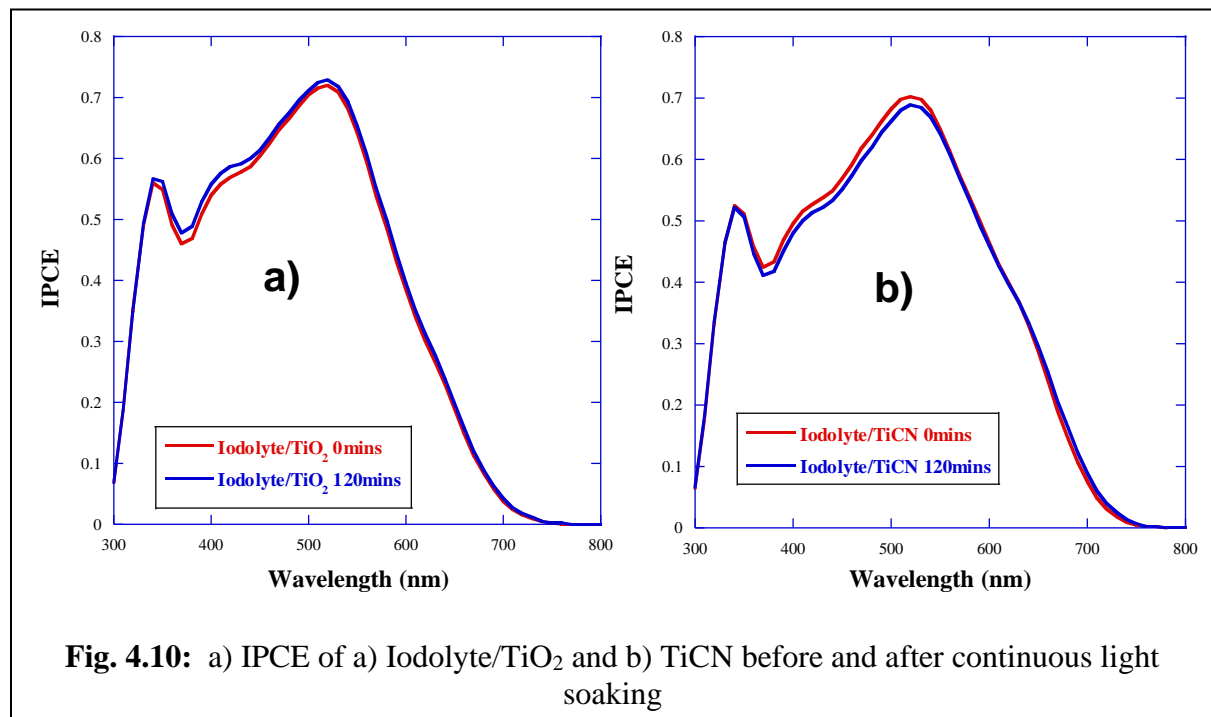
Table 4.4: DSSC performance parameters of various electrolytes under focused light at the focal distance of 2.5 cm.

Electrolyte Type	Time (min)	Temp (°C)	V_{oc} [V]	J_{sc} [mA/cm^2]	FF	E_{sys} [%]
Liquid Iodolyte	0	30	0.69	100.14	0.41	28.44
	30	68	0.69	82.77	0.44	25.21
	60	88	0.67	76.45	0.44	22.62
	90	93	0.66	73.29	0.45	21.68
	120	98	0.65	70.65	0.46	20.81
Iodolyte/TiO$_2$	0	30	0.72	80.31	0.45	25.84
	30	60	0.71	82.47	0.43	25.04
	60	75	0.69	83.23	0.42	24.44
	90	83	0.68	84.27	0.41	23.94
	120	98	0.68	84.87	0.41	23.61
Iodolyte/TiCN	0	30	0.71	81.36	0.44	25.52
	30	75	0.69	81.48	0.43	24.31
	60	85	0.66	82.49	0.42	22.89
	90	98	0.64	82.67	0.42	22.11
	120	110	0.64	83.58	0.41	22.11
Iodolyte/Si$_3$N$_4$	0	30	0.71	80.94	0.44	25.65
	30	64	0.70	82.48	0.43	25.29
	60	73	0.64	82.56	0.42	22.08
	90	85	0.64	82.62	0.41	22.47
	120	99	0.64	82.65	0.41	22.17

4.5 Conclusion

In this study, the performance of DSSC incorporating the four electrolytes (liquid Iodolyte, Iodolyte/TiO$_2$, Iodolyte/TiCN, and Iodolyte/Si$_3$N$_4$ electrolytes) was analyzed under 1 sun illumination and concentrated light irradiation. Under 1sun illumination, the Iodolyte/TiO$_2$ QSDSSC exhibited a high E$_{ff}$ of 5.02 % higher than that of the DSSC with the liquid Iodolyte electrolyte (E$_{ff}$ of 4.59 %). The high performance of the Iodolyte/TiO$_2$ QSDSSC has been ascribed to its relatively low rate of electron recombination and fast charge transport in the PGE. Under concentrated light irradiation, the liquid Iodolyte DSSC yielded the highest E$_{sys}$ of 28.44 %. At the same time, the Iodolyte/TiO$_2$ QSDSSC had an E$_{sys}$ of 25.84, which is an efficiency enhancement ratio of ~ 6.2 and ~5.1 times, respectively. The increase in E$_{sys}$ under concentrated light has been attributed to the rise in light intensity under focused irradiation. At higher temperatures, QSDSSCs exhibited higher performance stability than the liquid Iodolyte DSSC, which showed remarkably low stability due to the leakage and evaporation of the liquid electrolyte. Similar results were also obtained when a stability analysis was conducted under dark conditions at room temperature for 16 days. This study concluded that QSDSSC promises higher durability and favorable energy conversion efficiency under 1 sun illumination and concentrated illumination. QSDSSCs could present a unique opportunity for the application of DSSC in CPV systems.

4.6 References

1. B. O'Regan, M. Grätzel, Nature 353 (1991) 737–740. https://doi.org/10.1038/353737a0

2. M. Grätzel, et al, Journal of Photochemistry and Photobiology A: Chemistry, vol. 164, no. 1–3, pp. 3–14, 2004. https://doi.org/10.1016/j.jphotochem.2004.02.023

3. G. Hagfeldt, L. Boschloo, L. Sun, L. Kloo, H. Pettersso Chem. Rev., 110 (2010), pp. 6595-6663 https://pubs.acs.org/doi/10.1021/cr900356p

4. I. Liu, Y. Chen, Y. Cho, L. Wang, C. Chien, Y. Lee Jpowsour. 482, (2021), 228962 https://doi.org/10.1016/j.jpowsour.2020.228962

5. J.M. Cole, G. Pepe, O.K.A. Bahri, C.B. Chem. Rev., 119 (2019), pp. 7279-7327 https://doi.org/10.1021/acs.chemrev.8b00632

6. C.-P. Lee, C.-T. Li, K.-C. Ho, Mater Today Off., 20 (2017), pp. 267-283 https://doi.org/10.1016/j.mattod.2017.01.012

7. Y. Saygili, M. Söderberg, N. Pellet, F. Giordano, Y. Cao, A.B. Muñoz-García, S.M. Zakeeruddin, N. Vlachopoulos, M. Pavone, G. Boschloo, L. Kavan, J.-E. Moser, M. Grätzel, A. Hagfeldt, M. Freitag J. Am. Chem. Soc., 138 (2016), pp. 15087-15096 https://doi.org/10.1021/jacs.6b10721

8. K. Kakiage, Y. Aoyama, T. Yano, K. Oya, J.-I. Fujisawa, M. Hanaya, Chem. Commun., 51 (2015), pp. 15894-15897 https://doi.org/10.1039/C5CC06759F

9. S. Venkatesan, S. Su, W. Hung, I. Liu, H. Teng, Y. Lee, J. Power Sources. 298 (2015) 385-390.https://doi.org/10.1016/j.jpowsour.2015.07.062

10. H.W. Han, W. Liu, J. Zhang, X.-Z. Zhao Adv. Funct. Mater., 15 (2005), pp. 1940-1944 https://doi.org/10.1002/adfm.200500159

11. J.R. Durrant, S.A. Haque Nat. Mater., 2 (2003), pp. 362-363 https://doi.org/10.1038/nmat914

12. S. Venkatesana, I. Liu, J. Lin, M. Tsai, H. Teng, and Y. Lee, J. Mater. Chem. A. (2018), 6, 10085-10094. https://doi.org/10.1039/C8TA01729H

13. S. Yuan, Q. Tang, B. Hu, C. Ma, J. Duan, B. He J. Mater. Chem. A, 2 (2014), p. 2814 https://doi.org/10.1039/C3TA14385F

14. Q. Li, H. Chen, L. Lin, P. Li, Y. Qin, M. Li, B. He, L. Chu, Q. Tang J. Mater. Chem. A, 1 (2013), p. 5326 https://doi.org/10.1039/C3TA10224F

15. S. Yuan, Q. Tang, B. He, P. Yang J. Power Sources, 254 (2014), pp. 98-105 https://doi.org/10.1016/j.jpowsour.2013.12.112

16. Q. Li, X. Chen, Q. Tang, H. Cai, Y. Qin, B. He, M. Li, S. Jin, Z. Liu J. Power Sources, 248 (2014), pp. 923-930 https://doi.org/10.1016/j.jpowsour.2013.10.025

17. C.L. Chen, H. Teng, Y.L. Lee Adv. Mater., 23 (2011), pp. 4199-4204 https://doi.org/10.1002/adma.201101448

18. C.L. Chen, T.W. Chang, H. Teng, C.-G. Wu, C.-Y. Chen, Y.-M. Yang, Y.L. Lee Phys. Chem. Chem. Phys., 15 (2013), pp. 3640-3645 https://doi.org/10.1039/C3CP50170A

19. Y. Dkhissi, F. Huang, Y.-B. Cheng, R.A. Caruso J. Phys. Chem. C, 118 (2014), pp. 16366-16374 https://doi.org/10.1021/jp408844q

20. S.J. Seo, H.J. Cha, Y.S. Kang, M.S. Kang Electrochim. Acta., 145 (2014), pp. 217-223 https://doi.org/10.1016/j.electacta.2014.09.016

21. H.-W. Chen, Y.-D. Chiang, C.-W. Kung, N. Sakai, M. Ikegami, Y. Yamauchi, K.C.-W. Wu, T. Miyasaka, K.-C. Ho J. Power Sources, 245 (2014), p. 411 https://doi.org/10.1016/j.jpowsour.2013.06.142

22. D. T. Nguyen, Y. Kurokawa, R. Fujimoto, and K. Taguchi, Journal of the Japan Society of Applied Electromagnetics and Mechanics, 2019 Volume 27 Issue 1 Pages 97-101 https://doi.org/10.14243/jsaem.27.97

23. M. A. K. L. Dissanayake, R. Jayathissa, V. A. Seneviratne, C. A. Thotawatthage, G. K. R. Senadeera, and B. E. Mellander, Solid State Ionics, Vol. 265, pp. 85–91, 2014. https://doi.org/10.1016%2Fj.ssi.2014.07.019

24. J. Zhao, S. G. Jo, and D. W. Kim, Electrochim. Acta, Vol. 142, pp. 261–267, 2014. https://doi.org/10.1016%2Fj.electacta.2014.07.109

25. J. U. Kim, S. H. Park, H. J. Choi, W. K. Lee, J. K. Lee, and M. R. Kim, Sol. Energy Mater. Sol. Cells, Vol. 93, No. 6, pp. 803–807, 2009. https://doi.org/10.1016/j.solmat.2008.09.045

26. P . Selvaraja, H. Baig, T. K. Mallick, J. Siviter, A. Montecucco, W. Li, M. Paul, T. Sweet, M. Gao, A. R. Knox and S. Sundaram, Solar Energy Materials and Solar Cells, 175, (2018), 29-34 https://doi.org/10.1016/j.solmat.2017.10.006

27. H. Baig, N. Sellami, T.K. Mallick Sol. Energy Mater. Sol. Cells, 134 (2015), pp. 29-44, https://doi.org/10.1016/j.solmat.2014.11.019

28. H. Baig, N. Sarmah, D. Chemisana, J. Rosell, T.K. Mallick Energy, 73 (2014), pp. 177-191, https://doi.org/10.1016/j.energy.2014.06.008

29. I. Santos-gonzález, M. Sandoval-reyes, O. García-valladares, N. Ortega Energy Procedia, 57 (2014), pp. 2956-2965, https://doi.org/10.1016/j.egypro.2014.10.331

30. H.G. Agrell, J. Lindgren, A. Hagfeldt Sol. Energy, 75 (2003), pp. 169-180 https://doi.org/10.1016/S0038-092X(03)00248-2

31. A. Sacco, M. Gerosa, S. Bianco, L. Mercatelli, R. Fontana, L. Pezzati, M. Quaglio, C.F. Pirri, A.O.M. Tucci Dye-sensitized solar cell for a solar concentrator system Sol. Energy, 125 (2016), pp. 307-313, https://doi.org/10.1016/j.solener.2015.11.026

32. Chawarambwa, F. L., Putri, T. E., Son, M., Kamataki, K., Itagaki, N., Koga, K., & Shiratani, M. (2020). Cplett, 758, 137920. https://doi.org/10.1016/j.cplett.2020.137920

33. S. Hwang, J.H. Lee, C. Park, H. Lee, C. Kim, C. Park, M. Lee, W. Lee, J. Park, K. Kim, N. Park, C. Kim Chem. Commun. (2007), pp. 4887-4889 https://doi.org/10.1039/B709859F

34. S. Peng, L. Tian, J. Liang, S.G. Mhaisalkar, S. Ramakrishna, ACS Appl. Mater. Interfaces 4, (2012) 397-404 https://doi.org/10.1021/am201461c

35. Y. Duan, Q. Tang, Y. Chen, Z. Zhao, Y. Lv, M. Hou, P. Yang, B. He, L. Yu, Mater. Chem. A, (2015), 3, 5368-5374 https://doi.org/10.1039/C4TA06393G

36. H. Seo, M. Son, S. Hashimoto, T. Takasaki, N. Itagaki, K. Koga, M. Shiratani, Electrochimica Acta. 210 (2016) 880-887. https://doi.org/10.1016/j.electacta.2016.06.020

37. M.-S. Kang, K.-S. Ahn, J.-W. Lee J. Power Sources, 180 (2008), p. 896 https://doi.org/10.1016/j.jpowsour.2008.02.087

38. M.-S. Kang, J.H. Kim, J. Won, Y.S. Kang. J. Phys. Chem. C, 111 (2007), p. 5222. https://doi.org/10.1021/jp067621k

39. Brijesh Tripathi, Pankaj Yadav, Manoj Kumar, International Journal of Photoenergy, vol. 2013, Article ID 646407, 10 pages, 2013. https://doi.org/10.1155/2013/646407

40. S. Venkatesan and Y.-L. Lee , Coord. Chem. Rev., 2017, 353 , 58 —112 https://doi.org/10.1016/j.ccr.2017.09.026

CHAPTER FIVE: Performance Enhancement of DSSCs Via Stepwise co-sensitization of two dye sensitizers

5.0 Introduction

Solar energy is anticipated to become a leading next-generation sustainable and clean energy source. Solar energy is one of the leading available alternatives to mitigate CO_2 emissions to the environment because of the combustion of fossil fuels [1,2]. Photovoltaic technologies offer an efficient method to convert solar light to electricity. Photovoltaic technologies can supplant existing conventional power generating systems to satisfy the growing increasing energy demands. About 4 million exa-joules of solar energy reach the earth's surface, among them 5×10^4 EJ is easily harvestable [3,4].

Dye-sensitized solar cells (DSSCs) are third-generation, high-conversion efficiency solar cells based on a mesoporous semiconductor, electrolyte, and dye system developed by O`Regan and his team [5]. DSSCs development has attracted a lot of attention as a potential alternative to the Si-based solar cell due to their relatively high photo-electricity conversion efficiency, ease of fabrication, and production costs [6-7]. The DSSC consists of three components, namely: (1) a counter electrode (CE), (2) a photoanode, and (3) an electrolyte. The CE performs the following key functions: (i) conducting electrons from the external circuit and (ii) reduction of the electrolyte oxidized by the regeneration of the dye [8-10]. The photoanode is key to the operation of the DSSC as it is responsible for (i) the collection and transportation of electrons released by the dye after photoexcitation to the eternal circuit and (ii) act as a scaffolding that facilitates the adsorption of the dye on mesoporous oxide semiconductor materials [1,8, 11]. The electrolyte is typically placed between the photoanode and the CE, and its key function is the regeneration of the pho-excited dye. A wide range of electrolytes ranging from liquids [12], solids [13], and gel polymers [14] have been utilized in DSSCs. Among these, the liquid electrolyte is widely used due to its good characteristics such as low absorption of light, good solubility, and quick dye regeneration. Howbeit, liquid electrolyte also comes with certain drawbacks such as reduced stability, long-term durability, and poor performance at elevated temperatures [7]. Gel polymer membranes [7, 8] with higher performance stability have been developed to address these challenges.

Absorption of dye (photosensitizer), on porous semiconductor material such as ZnO and TiO$_2$, is essential for DSSC performance [15]. The photosensitizer mainly governs the photo-conversion efficiency of the DSSC. Broad absorption of the solar spectrum with high molar absorptivity and appropriate energy levels of the dye-photosensitizer is key to obtaining high photon flux and efficient electron transport to the electron semiconductor layer. This, in turn, influences the overall efficiency of the DSSC [16-18]. In the past decade, remarkable progress in the efficiency of DSSC was observed from 11.9 % [5] to 14 % [1, 19]. However, to promote wide and large-scale commercial utilization of the DSSC, there is a need to enhance the efficiencies of these photovoltaic devices further. According to Mehmood [20] and Hagfelt [16] et al., the low PCE of the DSSC was mainly due to the narrow absorption range of the dyes. At present, a single dye that can absorb solar spectrum in a range of 400-900 nm is not available [21].

The photosensitizers can be classified into two groups (i) the metal-free organic sensitizer and (ii) the metal complex sensitizers. Metal complex sensitizers usually consist of metal ions including Ni, Co, and Ru complex with terpyridine or bipyridine ligands and adsorbing groups [16]. The most utilized of these dyes are N719, N3, and N749 owing to their inherent and favourable qualities such as (i) long-lived photoexcited state, (ii) high molecular stability, (iii) broad absorption expanding to near-infrared (NIR) region, and (iv) molecular stability [22, 23]. These dyes have a wider spectral absorption range that facilitates high current density (J_{sc}) and can provide notable efficiencies > 10%. For instance, the IPCE onset of the N749 (black dye) is > 950 nm. However, to develop DSSCs for widespread commercial application, further improvements in photovoltaic performance are required. In the case of enhancing J_{sc}, wider coverage of the solar light spectrum is necessary. In principle, DSSC photosensitizers should absorb a wide range of the solar spectrum from the UV-to-IR region, and this requires that the HOMO-LUMO band gap be narrow. The theoretical minimum of the HOMO-LUMO bandgap energy of the photosensitizer is ~1.3-1.4 eV in the case of the TiO$_2$/iodine system [23]. The IPCE spectra of ruthenium-polypyridyl dyes in the NIR-IR and UV spectral regions are less than satisfactory, ensuing in a decrease in J_{sc}. Low IPCEs are due to the dyes' low light-harvesting capabilities corresponding to the spectral regions. Low IPCE values in the UV region are mainly due to competitive light absorption of the sensitizer and triiodide in the electrolyte. On the other hand, low IPCE values in the NIR-IR are attributed to the weak absorption coefficient [23,24]. Although the challenge of a weak absorption coefficient can be addressed by increasing the thickness of the semiconductor, this action will also lead to a

decrease in V_{oc} value which ultimately lowers the PCE of the DSSC [24]. As such, there is a need to enhance the absorption coefficient in the NIR-IR region while ensuring that there is no decrease in other parameters.

The above challenges can be addressed via a sensitization strategy. Co-sensitization, a technique that involves the sensitization of the mesoporous metal-oxide-semiconductor electrode with at least two photosensitizers, is an effective strategy to enhance the light-harvesting capabilities of DSSCs through the expansion of the light absorption range [23]. To date, numerous combinations of photosensitizers like ruthenium co-sensitized with porphyrin complexes [25], and ruthenium complexes co-sensitized with organic dyes [26-28], or co-sensitization of organic dyes with phthalocyanine [29, 30], have been utilized. In 2020, Younas et al [1] co-sensitized an organic sensitizer RK1 with another ruthenizer N749 and achieved a cell efficiency of 8.15%. Kuang et al., [30] employed a solvent-free electrolyte and co-sensitized two organic dyes (JK2 and SQ1) and achieved a PCE of 6.4%. Wanwong et al, [15], developed a boron dipyrromethene featuring a triphenylamine triad, which was then co-sensitized with N719 dye and achieved a PCE of 5.14%. Richhariya et al [31], co-sensitized metal-free organic sensitizers- bromophenol and eosin-Y, achieved a superior efficiency of 2.31%. While Althagafi et al [32], co-sensitized thiophene-based metal-free organic dyes IS-5 and achieved an outstanding efficiency of 8.09% compared to that of the N719 dye (7.62%).

There are two approaches through which co-sensitization can be carried out: (i) a "dye cocktail" and (ii) a stepwise sensitization method. In a "cocktail" method, the mesoporous semiconductor layer is sensitized by a mixture of at least two different dyes. Besides paying special attention to the dye-mixing ratio needs, this method is conducted the same way as the normal single dye adsorption process. However, a decrease in the dye-loading amount of the base dye can be expected because of competitive adsorption. On the other hand, the stepwise method is a lot more complicated. This sensitization method involves the sequential soaking of the semiconductor into each dye solution, which allows dyes to be adsorbed on the vacant spaces of the semiconductor surface (spaces where previous dyes have not been adsorbed) [23]. Since this method allows for the adsorption of different dyes on vacant spaces, competitive adsorption does not occur. Co-sensitization optimization is complicated due to sensitization parameters such as dye concentration, soaking time, soaking order, and other dye conditions. Therefore, through this study, we aimed to

demonstrate a method for effectively co-sensitizing the TiO$_2$ film of the DSSC via the stepwise co-sensitization technique. Herein two sensitizers, an organic (SQ2) and a ruthenium-ion (Z907) based sensitizer with complementary absorption spectrums were investigated. This study investigated the influence of dye soaking order and dye soaking time on the overall performance of the DSSC and the results have indicated that these two factors significantly influence DSSC performance.

5.2 Experimental Methods
5.2.1 Materials

Transparent TiO$_2$ pastes (T/SP), spacer (Meltonix 1170-60), iodine electrolyte (AN50), ruthenizer 520-DN (Z907 dye), and organic sensitizer SQ2 were purchased from Solaronix, Switzerland. Fluorine tin oxide doped glass substrate (FTO, sheet resistance 7 Ω cm^{-2}) was purchased from Sigma Aldrich. Platinum paste (Dyesol PT1) was purchased from Dyesol. Acetone and super-dehydrated ethanol (99.5 %) were purchased from Wako, Japan. All materials were used as purchased without further modifications.

5.2.2 Preparation of the DSSC

The fabrication of the DSSC is illustrated in **Fig. 5.1** for easy visualization. FTO glasses were used as substrates for both the CE and photoanode of the DSSC. The FTO was washed in demineralized water, ethanol, and acetate successively for 20 mins and then dried on a ceramic hot plate at 110 ℃ for 5 mins. The doctor blade method was used to prepare both the Pt CE and the TiO$_2$ photoanode, and both substrates were annealed at 200℃ for the first 10 mins and 450℃ for the next 30 mins. After cooling to room temperature, the TiO$_2$ films were subsequently soaked in respective dye solutions (SQ2 0.05mM and Z907 0.05mM in ethanol) for 18hrs. To facilitate co-sensitization of the dye, the Z907 dye pre-soaked TiO$_2$ films were first rinsed with ethanol and then immediately soaked in the second dye (SQ2) at various soaking durations (0.5, 1, 2, 3h). To fabricate the DSSC, the photoanode and CE were spaced by a 60μm thermoplastic and then sealed by a hot-press thermal process at 110℃. The liquid electrolyte (AN50) was then injected into the DSSC through predrilled holes, and holes were later sealed through another hot-press thermal process. In this study, the active area of the DSSC was 0.275 cm^2.
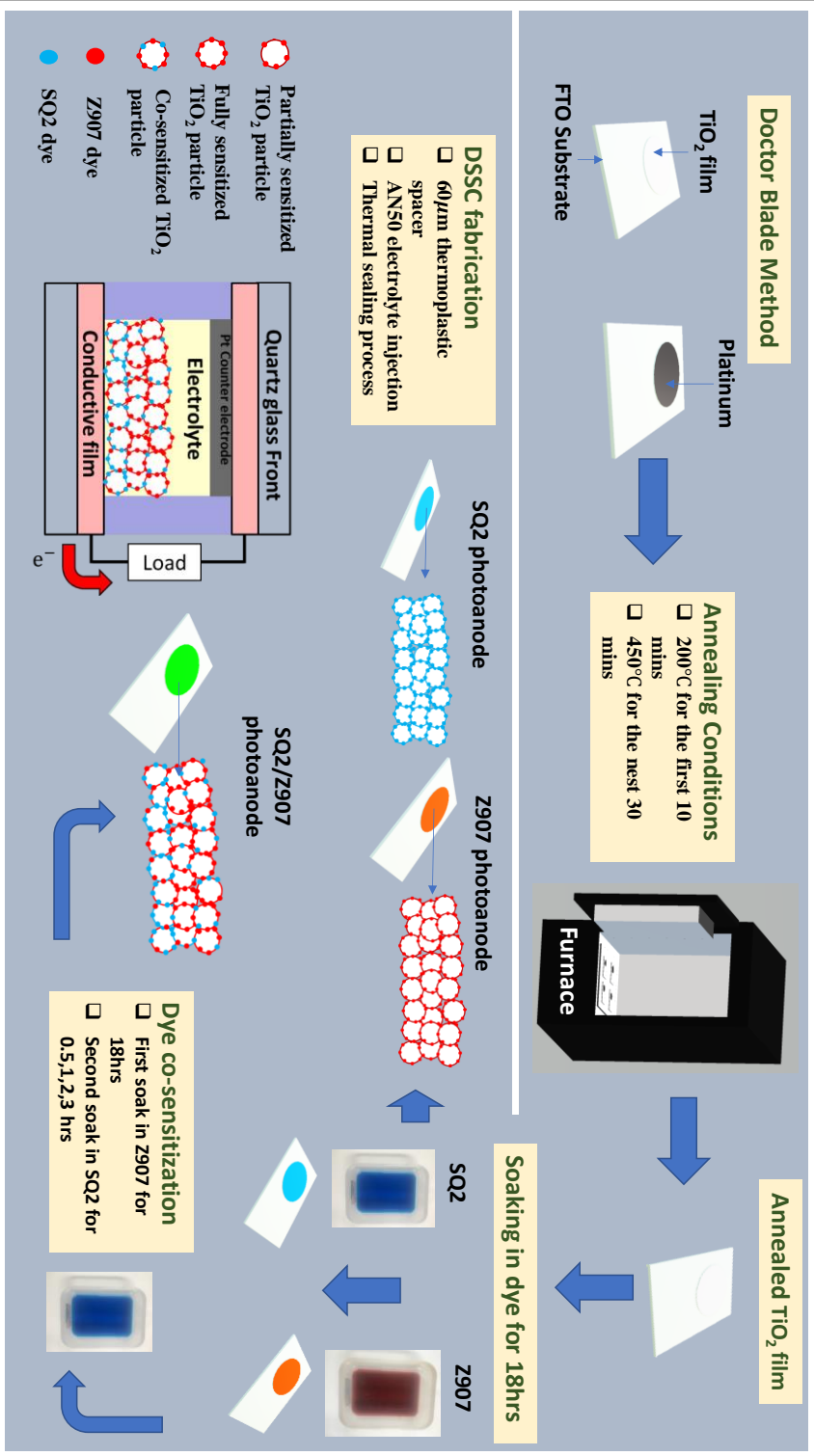
Fig. 5.1: Fabrication of the dye-sensitized solar cell.

5.2.3 Characterization

The cross-section of the transparent TiO_2 films was analyzed using a scanning electron microscope (Hitachi, SEM3500). The atomic composition of the various co-sensitized TiO_2 films was analyzed by a scanning electron microscope and subjected to elemental analysis by using energy dispersion spectrometry (EDX) (EDAX, AMETEK, Octane plus). A BioTek Synergy-HT spectrometer measured the UV-Visible-NIR spectra Z907 and N749 dyes (0.5mM in ethanol). A photo-simulator with a 1000 W Xeon short arc lamp was used to record the photovoltaic properties of the as-prepared DSSCs at 1 sun illumination. The incident photon to current conversion efficiency (IPCE) values (in the range of 240 - 800 nm of the light spectra) of the DSSC were measured by a Xeon arc lamp as the light source coupled with a monochromator. Electrochemical impedance spectroscopy (EIS) was carried out by employing an electrochemical analyzer (SP-150, Biologic SAS) in the frequency range of 10 mHz to 1 MHz.

5.3 Results and Discussion
5.3.1 SEM and EDX results

SEM was used to determine the surface morphology and thickness of the TiO_2 films. According to **Fig. 4.2a**, the thickness of the photoanode was approximately 10 μm. To achieve panchromatic DSSC and enhance the cell performance, the TiO_2 film was stepwise co-sensitized with a ruthenium ion-based dye (Z907) and an organic dye SQ2. For individually sensitized photoanode, the TiO_2 films were soaked in their respective dyes for 18hrs. In the case of co-sensitized dyes, the TiO_2 films were first soaked in sequence, first in the Z907 dye for 18 h, and later soaked in the SQ2 dye for a certain duration (0.5, 1, 2, 3 h). The soaking sequence influences the loading of each dye molecule and, ultimately the overall performance of DSSC. The EDX spectrum was used to analyze the atomic quantities of the co-sensitized TiO_2 films. The quantitative analysis is described in **Table 5.1**. The results indicate a gradual decrease in the atomic percentage of ruthenium ions in the co-sensitized films. It is believed that sequential dye soaking will facilitate the adsorption of the dye on the surface of the unoccupied TiO_2 nanoparticles. This is probably true in the case of the D709 18 h/SQ2 0.5 h and D907 18 h/SQ2 1.0 h films in which the Ru ion percentage is nearly the same.

However, with a further increase in soaking time, the percentage of Ru ions decreases to ~0.56%, which suggests that some of the Z907 molecules may have been replaced with the SQ2 dye molecules [**33**]. Therefore, it can be supposed that, for extended soaking time, the aggregation of the Z907 dye molecule is reduced by the competitive adsorption of the SQ2 dye molecule. This can also be explained based on the absorption modes of the two dyes.

Table 5.1: Atomic composition of the co-sensitized Dyes.

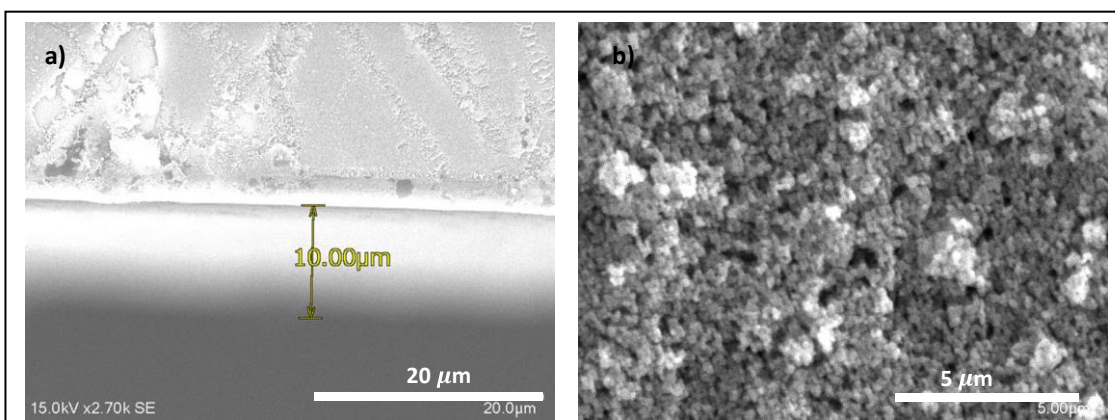| Photoanode	C	O	S	Ru	Ti
D709 18 h	14.70	51.09	1.07	0.72	29.18
SQ2 18 h	12.55	57.99	0.23	-	28.81
D709 18h/SQ2 0.5 h	14.12	50.08	1.03	0.69	31.09
D709 18 h/SQ2 1.0 h	14.90	50.38	0.98	0.67	31.81
D709 18 h/SQ2 2.0 h	14.76	50.55	1.04	0.56	31.17
D709 18 h/SQ2 3.0 h	14.82	50.74	1.02	0.53	31.70

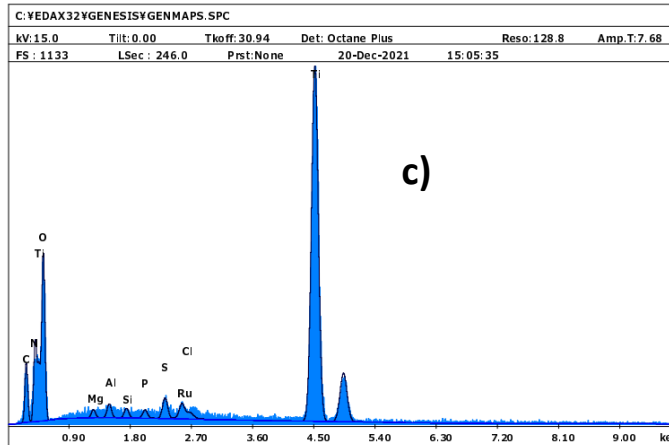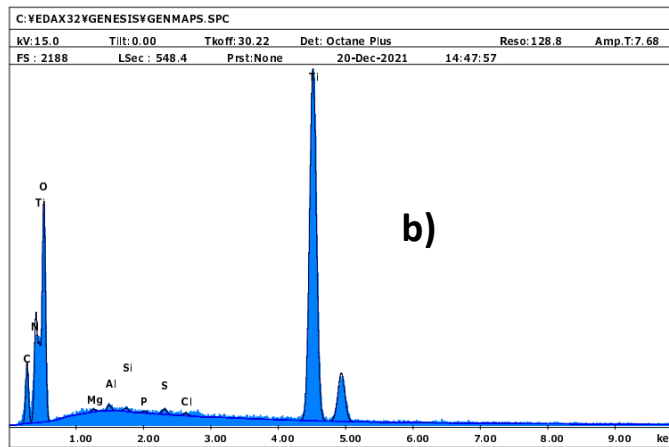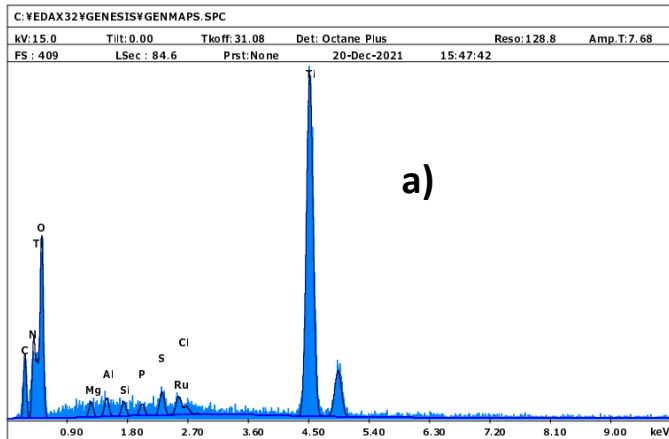**Fig. 5.2**: TiO$_2$ film a) thickness and b) surface image.

Fig. 5.3: EDX spectrum of a) D709 18 h b) SQ2 18 h and c) D709 18 h/SQ2 1.0 h.

5.3.2 Ultraviolet (UV-Vis) spectroscopy and Transmittance

Fig. 5.4a shows the UV-Vis absorption spectra of the Z907 and SQ2 dyes in ethanol. The absorption spectrum of SQ2 shows two absorption peaks in the region of 280 to380 nm and 520 to 690 nm. The 520-690 nm peak can be attributed to a) $\pi - \pi^*$ electronic transitions of the conjugated molecules and b) donor-acceptor anchoring groups` intermolecular charge transfer [**8**]. On the other hand, the Z907 dye shows three broader peaks at 280, 440, and 550 nm. These peaks can be attributed to intra-ligand ($\pi - \pi^*$) charge transfer and the metal-ligand charge transfer transitions, respectively [**8**]. The absorption spectra show that it is highly probable that through co-sensitization of these two respective dyes, the absorption spectrum of the DSSC could be broadened. **Fig. 5.4b** shows the transmittance of TiO_2 films soaked in SQ2 and DN709 dyes for various durations. The TiO_2/SQ2 film shows high transmittance in the 400-580 nm range which corresponds well with the weak absorbance of the SQ2 dye in the same range as shown in **Fig. 5.4a**. On the other hand, the TiO_2/DN709 film shows a weaker transmittance in the 350-540 nm range which corresponds well with the absorbance of the DN709 dye in the same range. Soaking of the TiO_2/DN709 film in SQ2 for 1 hour reduces lowers transmittance in the 300-350nm range from ~3.5 to 0%. Soaking in SQ2 dye further lowers transmittance, especially in the 350-540nm range. This could point to an increase in the absorbance of the films due to co-sensitization. However, although further increasing the soaking time of the TiO2/DN709 films in SQ2 (2 and 3 hrs) slightly reduces the transmittance of the films, this also leads to aggregation and dye overloading of the semiconductor films. It can be concluded that at a much higher soaking time in SQ2 dye, the overall performance of the co-sensitized photoanode is bound to decrease owing to both substitutional absorbance and dye overloading.

Fig. 5.4: UV-Vis spectra and structure and chemical names of Z907 and SQ2 dyes.
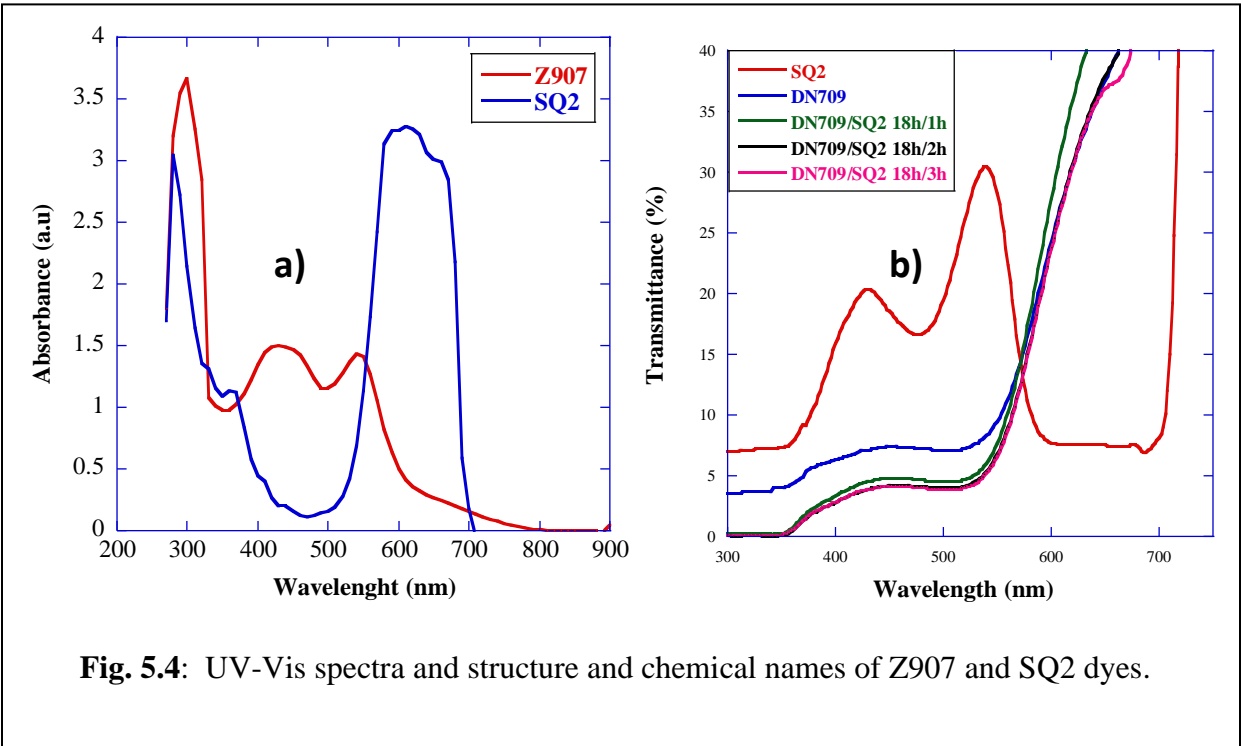
5.3.3 EIS analysis of the co-sensitized DSSC

Charge recombination is one of the major challenges in DSSCs. To elucidate the interfacial charge recombination process in the DSSCs, electrochemical impedance spectroscopy (EIS) was employed. The Nyquist plots and the equivalence circuit are shown in **Fig. 5.5** and the impedance values are shown in **Table 5.2**. Z_1 refers to the impedance between the CE/electrolyte interface. Z_1 is represented by the first semicircle and measurements are conducted in the high-frequency range (1MHz ~ 1kHz). Z_2 is the internal impedance related to the charge transfer at the photoanode/electrolyte interface. The second semi-circle and measurements representing Z_2 are conducted in the middle-frequency range (1kHz ~ 1 Hz). Electron recombination in the TiO_2/dye/electrolyte interface can be calculated from the recombination lifetime (τ_{oc}) equation [**7**]:

$$\tau_{oc} = R_2 C_2 \qquad\qquad (5.1)$$

where C_2 and R_2 are the charge transfer capacitance and resistance associated with impedance Z_2, respectively. Normally, higher Z_2 values indicate a smaller dark current and an increased charge recombination resistance [**32**]. Results show a gradual increase in Z_2 resistance (R_2) as the SQ2 dye soaking time increases. For the individually soaked Z907, DSSC R_2 is 21.22 Ω, while that of the SQ2 DSSC is 601Ω. In the case of the co-sensitized DSSCs, R_1 values increased from 22.88 Ω (SQ2 soaking time 0.5hrs) to 23.59Ω (SQ2 soaking time, 3hrs). This indicates a slight increase in charge recombination resistance with an increase in SQ2 dye soaking time. Larger R_1 values indicate that it is more difficult to transfer the injected electrons from the TiO_2 particles back to the electrolyte. As a result, back recombination can be suppressed in the DSSC. The Z907 sensitized DSSC had the smallest τ_{oc}, which indicates a faster electron recombination process between the injected electrons and the I_3^- in the electrolyte [**7**]. Co-sensitized DSSCs exhibit slightly higher τ_{oc} values and this can be attributed to the aggregation of dye molecules on the TiO_2 films (due to dye overloading or failed adsorptions), which affects electron recombination.
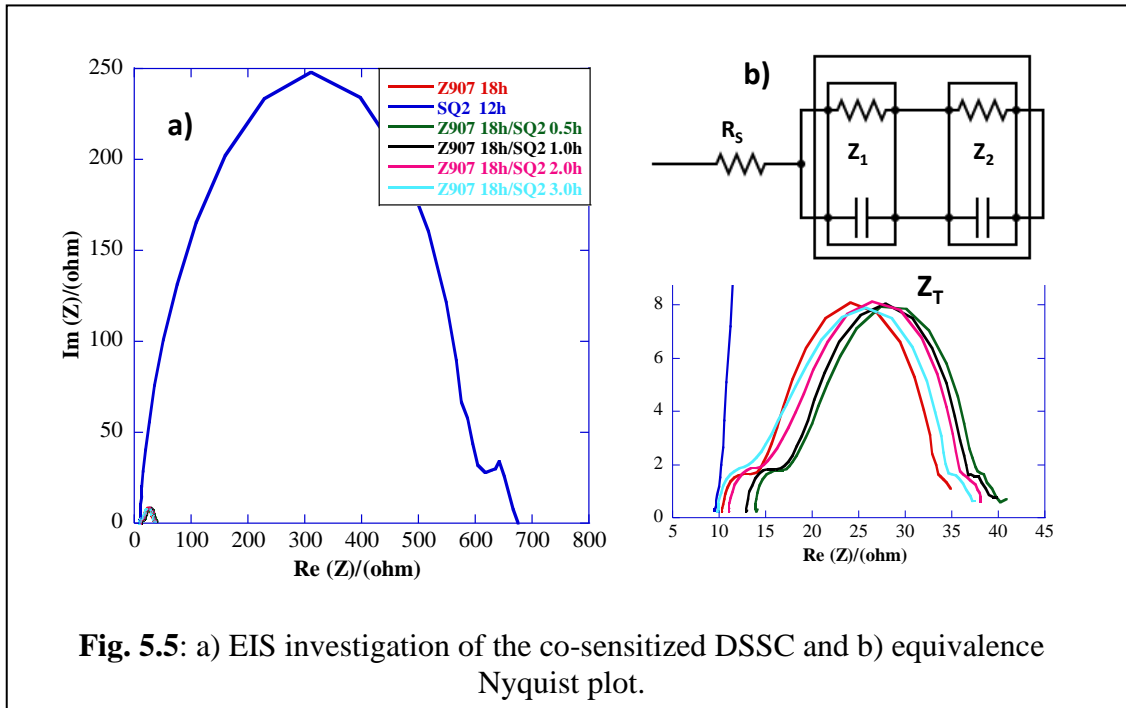
Fig. 5.5: a) EIS investigation of the co-sensitized DSSC and b) equivalence Nyquist plot.

Table 5.2: Surface resistance and impedance values.

DSSC	R_s (Ω)	Z_1 Resistance (Ω) Capacitance (μF)	Z_2 Resistance (Ω) Capacitance (μF)	Z_T Resistance (Ω) Capacitance (μF)	τ_{oc} Recombination Lifetime (ms)
Z907 18 h	10.4	5.15	21.22	24.69	2.25
		9.29	106	109	
SQ2 12h	9.56	15.17	601	613	3.20
		0.16	5.33	6.42	
Z907 18h/SQ2 0.5h	14.07	4.23	22.88	25.99	3.32
		5.24	145	128	
Z907 18h/SQ2 1.0h	12.99	4.68	22.71	26.1	3.32
		4.73	144	127	
Z907 18h/SQ2 2.0h	11.09	5.46	23.26	27.37	3.30
		5.97	142	127	
Z907 18h/SQ2 3.0h	9.81	5.78	23.59	27.41	3.25
		5.64	138	127.4	

5.3.4 IPCE and J-V characteristics of the DSSCs

The IPCE can be used to confirm the spectral attribution of the co-sensitized devices (shown in **Fig. 5.6a**). IPCE is the measurement of external quantum efficiency (EQE) of fabricated DSSC over a specific wavelength range (from 240-800 nm). In simple terms, IPCE/EQE explains the efficient workability of the fabricated DSSC in the specified wavelength region [**1,8**]. IPCE is the ratio between the total sum of all generated electrons in response to the total sum of photons falling on the active area of the fabricated DSSC. According to Grätzel [**34**], IPCE can be calculated by **Eq. 5.2**:

$$\text{IPCE} (\lambda) = \text{LHE} (\lambda) * \varphi_{inj} * \eta_{cc} \tag{5.2}$$

Where *LHE* is the light-harvesting efficiency which is highly dependent on the wavelength. φ_{inj} represents the amount of injected photo-generated electrons from the excited dye to the conduction band of the TiO$_2$ nanoparticles. Lastly, η_{cc} is a factor that represents the collection efficiency of the photo-generated electrons. All these three quantum efficiencies are related to the adsorbed dye concentration, TiO$_2$ inter-particle connectivity, the number of absorbed photons by the dye, and TiO$_2$ inter-particle connectivity.

Fig. 5.6: a) IPCE spectra and b) I-V curve of differently co-sensitized DSSCs
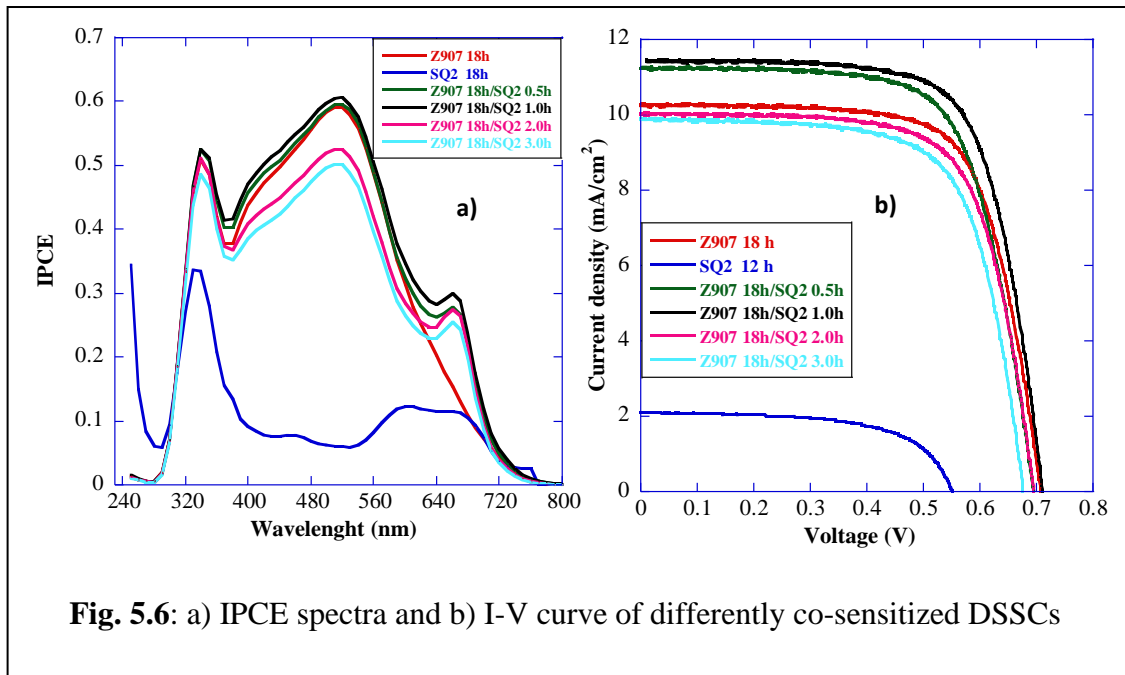
It should be noted that the IPCE spectrum shows progressive changes in the long-wavelength region with SQ2 dye soaking time. The IPCE results indicate an improvement in IPCE in the range of 620-720 nm after co-sensitization. From **Fig. 5.6a**, there is a general increase in overall IPCE as the soaking time in SQ2 dye is increased from 0 to 1 hr. However, a further increase in SQ2 dye soaking time results in significant IPCE reduction between the 400-620 nm range. The overall decrease in IPCE at extended SQ2 dye soaking time may be attributed to either of the following reasons:

a) the substitutional adsorption of the more efficient Z907 dye by the lesser efficient SQ2 dye ultimately results in the reduction of cell performance
b) prolonged soaking of the TiO_2 film in the SQ2 dye eventually leads to overlapping dye molecule aggregations, which eventually reduces the overall performance of the DSSC [**33**].

Table 5.3: Photovoltaic parameters of the fabricated DSSC

Device	Dye	Voc[V]	Jsc [A/m^2]	FF	Eff [%]
1	18h in N709	0.71	10.23	0.71	5.12
2	12h in SQ2	0.58	3.12	0.61	1.10
3	18h in N709/0.5h in SQ2	0.69	11.23	0.69	5.47
4	18h in N709/1h in SQ2	0.71	11.39	0.71	5.75
5	18h in N709/2h in SQ2	0.70	10.01	0.70	4.85

Fig. 5.6b shows the I-V curves of the fabricated DSSCs with co-sensitizers. The photovoltaic parameters: current density (J_{sc}), open-circuit voltage (V_{oc}), fill factor (FF) and efficiency (η) are listed in **Table 5.3**. The DSSC with Z907 dye showed an efficiency of 5.12% while the SQ2-sensitized DSSC showed an efficiency of 1.10%. **Table 5.3** shows that the current density and cell performance of the co-sensitized DSSC increase with SQ2 dye-soaking time until it optimizes at 1hr. When the SQ2 dye soaking time was 1hr, the co-sensitised DSSC showed Jsc = 11.39

MA/cm2, Voc = 0.71, FF = 071 and η= 5.75 %. The performance is higher than the individually sensitized DSSCs (Z907 and SQ2). The enhanced performance can be attributed to the co-sensitization technique, which avails the DSSC with maximum absorption owing to the higher absorption coefficient of the organic dye (SQ2) and more current owing to the less bandgap of the Ru ion-based dye (Z907). Further increase in SQ2 dye soaking time results in a decrease in both current density and cell performance. The subsequent loss in V_{oc} with the increase in SQ2 dye soaking time is probably due to the extended SQ2 dye loading time resulting in serious dye aggregation on the TiO_2 films, which lowers DSSC V_{oc}. The results can be attributed to the difference in adsorption rates of the SQ2 and the Z907 dyes i.e., the higher adsorption rate of SQ2 makes the unbalance of the loading amounts for the two dye molecules on the TiO_2 films. The existence of competitive adsorption in the post-adsorption process of SQ2 in which some of the pre-adsorbed Z907 molecules are replaced by SQ2 dye is also believed to be true. Through competitive adsorption loading, the extra Z907 is replaced by SQ2, which appears to form stronger bonds with the TiO_2 surface. These results are consistent with the IPCE which decreases with prolonged SQ2 dye soaking time. The results indicate that the overall performance of the co-sensitized DSSC depends on the dye soaking order and soaking time.

5.4 Conclusion

In this study, we have demonstrated a method for enhancing the performance of DSSCs through a stepwise co-sensitization technique. Organic sensitizer SQ2 was used as the co-sensitizer with a ruthenium ion-based sensitizer Z907. The TiO_2 film was first sensitized in Z907 for 18hrs and later sensitized in the SQ2 dye at various durations (0.5-3 h). The fabricated DSSCs were characterized by EDS spectroscopy, EIS, IPCE, and I-V characteristics. The major findings of this study are as follows:

a) The results have indicated that the stepwise co-sensitization technique is effective in boosting the overall cell performance of the DSSC

b) IPCE measurements indicate an increase in the 620-800 nm range when the pre-sensitized Z907 film is co-sensitized with the SQ2 dye. It has been observed that overall IPCE increases as the SQ2 dye soaking time increased from 0 to 1 hr. However, a further increase in SQ2 dye soaking time results in significant IPCE reduction between the 400-620 nm

range. This decrease in IPCE has been attributed to either i) the substitutional adsorption of the more efficient Z907 dye by the lesser efficient SQ2 or ii) the overlapping dye molecule aggregations, which ultimately reduce the overall performance of the DSSC.

c) The performance of the co-sensitized DSSC increases with SQ2 dye soaking time and optimizes at an efficiency of 5.75%. This is significantly higher than the performance of individually sensitized DSSCs (SQ2 = 1.10% and Z907 = 5.12%).

d) Electrochemical examinations have indicated low charge transfer resistance in co-sensitized DSSCs.

The study revealed a decrease in impedance associated with the counter electrode/electrode for the best-performing co-sensitized DSSCs, which reduces dark current and increases the current density of the DSSCs.

5.5 References

1) M. Younas, K. Harrabi, Performance enhancement of dye-sensitized solar cells via co-sensitization of ruthenium (II) based N749 dye and organic sensitizer RK1, Solar Energy. 203 (2020) 260–266. doi:10.1016/j.solener.2020.04.051.

2) M.A. Ehsan, M. Younas, A. Rehman, M. Altaf, M.Y. Khan, A. Al-Ahmed, et al., Synthesis and utilization of platinum(ii) dialkyldithiocarbamate precursors in aerosol assisted chemical vapor deposition of platinum thin films as counter electrodes for dye-sensitized solar cells, Polyhedron. 166 (2019) 186–195. doi:10.1016/j.poly.2019.03.058.

3) E. Kabir, P. Kumar, S. Kumar, A.A. Adelodun, K.-H. Kim, Solar energy: Potential and future prospects, Renewable and Sustainable Energy Reviews. 82 (2018) 894–900. doi:10.1016/j.rser.2017.09.094.

4) E.H. Adeh, S.P. Good, M. Calaf, C.W. Higgins, Solar PV power potential is greatest over croplands, Scientific Reports. 9 (2019). doi:10.1038/s41598-019-47803-3.

5) B. O'Regan, M. Grätzel, A low-cost, high-efficiency solar cell based on dye-sensitized colloidal Tio$_2$ films, Nature. 353 (1991) 737–740. doi:10.1038/353737a0.

6) F.L. Chawarambwa, T.E. Putri, S.-H. Hwang, P. Attri, K. Kamataki, N. Itagaki, et al., Improved luminescence performance of Yb^{3+}-Er^{3+}-Zn^{2+}: Y_2O_3 phosphor and its application to solar cells, Optical Materials. 123 (2022) 111928. doi:10.1016/j.optmat.2021.111928.

7) F.L. Chawarambwa, T.E. Putri, P. Attri, K. Kamataki, N. Itagaki, K. Koga, et al., Effects of concentrated light on the performance and stability of a quasi-solid electrolyte in dye-sensitized solar cells, Chemical Physics Letters. 781 (2021) 138986. doi:10.1016/j.cplett.2021.138986.

8) M. Younas, M.A. Gondal, U. Mehmood, K. Harrabi, Z.H. Yamani, F.A. Al-Sulaiman, Performance enhancement of dye-sensitized solar cells via cosensitization of ruthenizer Z907 and organic sensitizer SQ2, International Journal of Energy Research. 42 (2018) 3957–3965. doi:10.1002/er.4154.

9) F.L. Chawarambwa, T.E. Putri, M.-K. Son, K. Kamataki, N. Itagaki, K. Koga, et al., Graphene-Si3N4 nanocomposite blended polymer counter electrode for low-cost dye-sensitized solar cells, Chemical Physics Letters. 758 (2020) 137920. doi:10.1016/j.cplett.2020.137920.

10) U. Mehmood, H. Asghar, F. Babar, M. Younas, Effect of graphene contents in polyaniline/graphene composites counter electrode material on the photovoltaic performance of dye-sensitized solar cells (DSSCs), Solar Energy. 196 (2020) 132–136. doi:10.1016/j.solener.2019.12.024.

11) M.-E. Yeoh, K.-Y. Chan, Recent advances in photo-anode for dye-sensitized solar cells: A Review, International Journal of Energy Research. 41 (2017) 2446–2467. doi:10.1002/er.3764.

12) K. Ashok Kumar, K. Subalakshmi, M. Karl Chinnu, J. Senthilselvan, Polarization effect of dye-sensitizers on the current density and photovoltaic efficiency of co-sensitized dsscs using metal-free and metal-based organic dyes, Journal of Materials Science: Materials in Electronics. 30 (2018) 230–240. doi:10.1007/s10854-018-0285-5.

13) H. Iftikhar, G.G. Sonai, S.G. Hashmi, A.F. Nogueira, P.D. Lund, Progress on electrolytes development in dye-sensitized solar cells, Materials. 12 (2019) 1998. doi:10.3390/ma12121998.

14) J.C. de Haro, E. Tatsi, L. Fagiolari, M. Bonomo, C. Barolo, S. Turri, et al., Lignin-based polymer electrolyte membranes for sustainable aqueous dye-sensitized solar cells, ACS Sustainable Chemistry & Engineering. 9 (2021) 8550–8560. doi:10.1021/acssuschemeng.1c01882.

15) S. Wanwong, W. Sangkhun, J. Wootthikanokkhan, The effect of co-sensitization methods between N719 and boron dipyrromethene triads on dye-sensitized solar cell performance, RSC Advances. 8 (2018) 9202–9210. doi:10.1039/c8ra00862k.

16) A. Hagfeldt, G. Boschloo, L. Sun, L. Kloo, H. Pettersson, Dye-sensitized solar cells, Chemical Reviews. 110 (2010) 6595–6663. doi:10.1021/cr900356p.

17) J.-H. Yum, E. Baranoff, S. Wenger, M.K. Nazeeruddin, M. Grätzel, Panchromatic engineering for Dye-sensitized solar cells, Energy Environ. Sci. 4 (2011) 842–857. doi:10.1039/c0ee00536c.

18) B.E. Hardin, H.J. Snaith, M.D. McGehee, The renaissance of dye-sensitized solar cells, Nature Photonics. 6 (2012) 162–169. doi:10.1038/nphoton.2012.22.

19) K. Kakiage, Y. Aoyama, T. Yano, K. Oya, J.-ichi Fujisawa, M. Hanaya, Highly-efficient dye-sensitized solar cells with collaborative sensitization by silyl-anchor and carboxy-anchor dyes, Chemical Communications. 51 (2015) 15894–15897. doi:10.1039/c5cc06759f.

20) U. Mehmood, S. Ahmed, I.A. Hussein, K. Harrabi, Co-sensitization of tio 2 -mwcnts hybrid anode for efficient dye-sensitized solar cells, Electrochimica Acta. 173 (2015) 607–612. doi:10.1016/j.electacta.2015.05.132.

21) J.-H. Yum, S.-R. Jang, P. Walter, T. Geiger, F. Nüesch, S. Kim, et al., Efficient co-sensitization of nanocrystalline tio2 films by organic sensitizers, Chemical Communications. (2007) 4680. doi:10.1039/b710759e.

22) M. Grätzel, Dye-sensitized solar cells, Journal of Photochemistry and Photobiology C: Photochemistry Reviews. 4 (2003) 145–153. doi:10.1016/s1389-5567(03)00026-1.

23) Y. Numata, S. Zhang, X. Yang, L. Han, Cosensitization of ruthenium–polypyridyl dyes with organic dyes in dye-sensitized solar cells, Chemistry Letters. 42 (2013) 1328–1335. doi:10.1246/cl.130701.

24) S. Nakade, Y. Saito, W. Kubo, T. Kitamura, Y. Wada, S. Yanagida, Influence of tio2 nanoparticle size on electron diffusion and recombination in dye-sensitized tio2 solar cells, The Journal of Physical Chemistry B. 107 (2003) 8607–8611. doi:10.1021/jp034773w.

25) H.-P. Wu, Z.-W. Ou, T.-Y. Pan, C.-M. Lan, W.-K. Huang, H.-W. Lee, et al., Molecular engineering of cocktail co-sensitization for efficient panchromatic porphyrin-sensitized solar cells, energy & Environmental Science. 5 (2012) 9843. doi:10.1039/c2ee22870j.

26) H. Ozawa, R. Shimizu, H. Arakawa, Significant improvement in the conversion efficiency of black-dye-based dye-sensitized solar cells by cosensitization with organic dye, RSC Advances. 2 (2012) 3198. doi:10.1039/c2ra01257j.

27) L. Wei, Y. Yang, R. Fan, P. Wang, L. Li, J. Yu, et al., Enhance the performance of dye-sensitized solar cells by co-sensitization of 2,6-bis(iminoalkyl)pyridine and N719, RSC Advances. 3 (2013) 25908. doi:10.1039/c3ra44194f.

28) G.D. Sharma, G.E. Zervaki, P.A. Angaridis, A. Vatikioti, K.S.V. Gupta, T. Gayathri, et al., Stepwise co-sensitization as a useful tool for enhancement of power conversion efficiency of dye-sensitized solar cells: The case of an unsymmetrical porphyrin dyad and a metal-free organic dye, Organic Electronics. 15 (2014) 1324–1337. doi:10.1016/j.orgel.2014.03.033.

29) Y. Chen, Z. Zeng, C. Li, W. Wang, X. Wang, B. Zhang, Highly efficient co-sensitization of nanocrystalline tio2 electrodes with plural organic dyes, New Journal of Chemistry. 29 (2005) 773. doi:10.1039/b502725j.

30) D. Kuang, P. Walter, F. Nüesch, S. Kim, J. Ko, P. Comte, et al., Co-sensitization of organic dyes for efficient ionic liquid electrolyte-based dye-sensitized solar cells, Langmuir. 23 (2007) 10906–10909. doi:10.1021/la702411n.

31) G. Richhariya, A. Kumar, Performance evaluation of mixed synthetic organic dye as sensitizer based dye sensitized solar cell, Optical Materials. 111 (2021) 110658. doi:10.1016/j.optmat.2020.110658.

32) I. Althagafi, N. El-Metwaly, Enhancement of dye-sensitized solar cell efficiency through co-sensitization of thiophene-based organic compounds and metal-based N-719, Arabian Journal of Chemistry. 14 (2021) 103080. doi:10.1016/j.arabjc.2021.103080.

33) Y. Zhao, F. Lu, J. Zhang, Y. Dong, B. Zhang, Y. Feng, Stepwise co-sensitization of two metal-based sensitizers: Probing their competitive adsorption for improving the photovoltaic performance of dye-sensitized solar cells, RSC Advances. 7 (2017) 10494–10502. doi:10.1039/c6ra28473f.

34) M. Grätzel, Solar energy conversion by dye-sensitized photovoltaic cells, Inorganic Chemistry. 44 (2005) 6841–6851. doi:10.1021/ic0508371.

CHAPTER SIX: Efficient and Transparent Counter Electrode for Application in Solar Cells

6.0 Introduction

The dye-sensitized solar cell is a new breed of third-generation solar cells. This cell exhibits excellent qualities ranging from a low cost of production, and ease of production to high power conversion efficiency [1-4]. As a result, this cell has received a lot of acclamation and is currently undergoing extensive investigation due to its promising properties. However, despite these advantages, DSSC solar cells still face problems such as low durability, and low power generation efficiency compared to silicon solar cells and continue to employ an expensive platinum-based counter electrode [4]. The basic structure of a DSSC consists of a mesoporous TiO_2 semiconductor layer, a light-absorbing dye, a redox couple electrolyte, and a counter electrode (CE). The CE is an important component of the DSSC whose purpose is the collection of electrons from the external circuit and the regeneration of the electrolyte redox couple (I^-/I_3^-) [3-4]. The commonly employed Pt CE exhibits high conductivity and electrocatalytic activity in the reduction of I_3^- ions to I^- ions, however, Pt is both rare and expensive [5]. It is, therefore, necessary that more stable, efficient, and cost-effective counter electrodes be developed for the utilization in DSSCs. In recent studies, several non-Pt materials have been investigated, such as carbon materials (graphene [6,7] and carbon black [8]), conductive polymers (polyaniline [9], Polypyrrole [10]), alloys [11], and transition metals compounds [12]. Many of which have shown excellent prospects as potential replacements for the Pt CE.

The development of transparent CE is particularly important for extending the potential applications of DSSCs as well as addressing the current energy demand. In a bifacial DSSC, incident irradiation must pass through the glass substrate and excite the dye adsorbed onto the mesoporous TiO_2 layer of the photoanode [9]. An effective bifacial DSSC has a CE that allows a significant amount of light to pass through without being reflected or scattered. There has been a lot of research on materials that can be utilized for developing highly transparent CEs. Some materials such as carbon nitride [5], carbon nanotubes [13], MoS_2:PEDOT:PSS [14] Pt-Mo_2C

[15], Pt [16], PANI [9], and Polypyrrole [10] have exhibited excellent performance in bifacial applications owing to their high light transmittance and unique chemical properties [5].

This study aimed to develop a highly transparent CE that is capable of completely replacing the conventional Pt CE. PEDOT:PSS is a conductive polymer that has gained a lot of attention in recent years. Its application to dye-sensitized solar cells as a potential substitute for Pt has also been investigated numerous times [4,17]. The PEDOT:PSS CE has exhibited high voltage and high current density values that closely match those of the Pt electrode. Howbeit, owing to the flatness and reduced surface area of PEDOT:PSS, the catalytic activity of the electrode is quite low and this results in a low fill factor [4,14]. The challenge now is how best can the catalytic activity of the PEDOT:PSS electrode be enhanced? Studies on PEDOT:PSS that have been conducted before, have proved that surface area, conductivity, or even electrocatalytic activity can be enhanced through the addition of materials such as DMSO [18], graphene [17], carbon black [19], and Si_3N_4 [4]. In this work, PEDOT:PSS is mixed with a dimethyl sulfoxide (DMSO), a surfactant; iso-octyphenoxy-polyethoxyethanol commonly known as Triton X-100 (hereafter referred to as TX100) and TiO_2 nanoparticles to form a new polymer CE. Triton X-is a surfactant that is widely utilized for enhancing the film porosity of different materials [20]. In a previous study by Choi et al [21] Triton X-100 was employed to increase the conductivity of PEDOT:PSS films by stabilizing the PEDOT nanoparticles. In another study by Fic. et al [22] it was discovered that Triton-X-100 can enhance the capacitance of the PEDOT:PSS film by increasing the wettability of the CE. Triton X-100 can also enhance the stability of the PEDOT:PSS film by decreasing surface tension [22].

The developed CE has exhibited high transmittance, high conductivity, low internal resistance, and high electrocatalytic performance.

6.1 Experimental Methods

6.1.2 Preparation of the CE

3 wt% Triton X-100 (Sigma Aldrich) is added to a mixture of 1 ml of PEDOT:PSS, Clevious pH-1000 (Heraeus), and 5 wt% dimethyl sulfoxide (DMSO) (Yoneyama). The mixture was magnetically stirred on a ceramic plate at room temperature for 24 hrs. to form a stable uniform PEDOT:PSS/DMSO/TX100 mixture. 5 mg of TiO_2 nanoparticles (20 nm, Sigma Aldrich) were added separately to 1 ml of PEDOT:PSS/DMSO/TX100 solution mixture. The solution mixture and the TiO_2 nanoparticles were sequentially mixed by a conditioning mixture (AR-Thinky) at 1000 rpm and 400 rpm for 10 and 3 mins respectively, to produce a uniform PEDOT:PSS/DMSO/TX100/TiO_2 solution-mixture. A conductive glass substrate, with a fluorine-doped tin oxide (FTO) layer with a sheet resistance of 7 Ω cm^{-2} (Sigma Aldrich), was used as the substrate for both the anode and the cathode. The FTO was sonicated successively in acetone, ethanol, and deionized water for 20 mins. Uniform CE films of PEDOT:PSS/DMSO/TX100/TiO_2 were obtained after the solution mixtures were spin-coated on clean FTO glass at 4000 rpm for 60 sec. The counter-electrodes were subsequently annealed at 110 ℃ for 10 mins. For comparison, a platinum CE was also prepared. 10 mM of H_2PtCl_6 solution in isopropanol was screen printed on the FTO substrate and sintered at 450℃ for 30 minutes.

6.1.3 Preparation of TiO₂ electrode and fabrication of DSSC

Firstly, TiO_2 colloids (T/SP SOLARONIX) were printed on the FTO glass and sintered at 450°C for 1 hour to form transparent photoelectrode films (the active area of the photoanode was set at 0.275 cm^2). The films were later soaked in the N-719 dye solution (4 x 10^{-4} M ethanol) for 20 hrs. A thermoplastic, (Meltonix 60 μm, SOLARONIX) was utilized as both the sealant and space between the CE and the photoanode. Eventually, a sandwich-type DSSC was fabricated with the CE, an iodine electrolyte (AN50 SOLARONIX), and a sealing process with the help of a hot press.

6.2 Characterization

The transmittance of the PEDOT:PSS/DMSO, PEDOT:PSS/DMSO/TX100/TiO$_2$, and Pt CE films in the visible region was conducted by a UV-VIR-NIR spectrophotometer (V-570, JASCO, spectral resolution of 5-20nm). The morphology of the PEDOT:PSS/DMSO and PEDOT:PSS/DMSO/TX100/TiO$_2$ films were analyzed using an SEM (JIB-4600F, JEOL). The surface roughness of the two CE films was measured by an AFM (Dimension Icon, Bruker). Electrochemical impedance spectroscopy (EIS: SP-150, Biologic SAS) (10 mHz to 1 MHz) was used to measure the internal impedance of the DSSCs. A photo-simulator with a 1000 W Xeon short arc lamp was used to record the photovoltaic properties of the as-prepared DSSCs at 1 sun illumination, room temperature, and an AM of 1.5. The incident photon to current conversion efficiency (IPCE) (in the range 300 - 800 nm of the light spectra) of the DSSCs were evaluated using a Xeon arc lamp as the light source coupled with a monochromator.

6.3 Results and Discussion

6.3.1 Surface Morphology

Fig. 6.1 shows the SEM images of the cross-section of both the PEDOT:PSS and PEDOT:PSS/DMSO/Triton X-100/TiO$_2$ films. Both CE films show good adhesion with the FTO glass. The thickness of the PEDOT:PSS and PEDOT:PSS/DMSO/TX100/TiO$_2$ films averaged 68.8 and 800.1 nm, respectively. This shows that the addition of TX100 and TiO$_2$ nanoparticles adjust the structure of the PEDOT:PSS film and increases film thickness. This is mainly due to the properties of Triton X-100 as a surfactant which increases surface tension, and surface adhesion between molecules and ultimately raises the viscosity of the PEDOT:PSS [20,23].
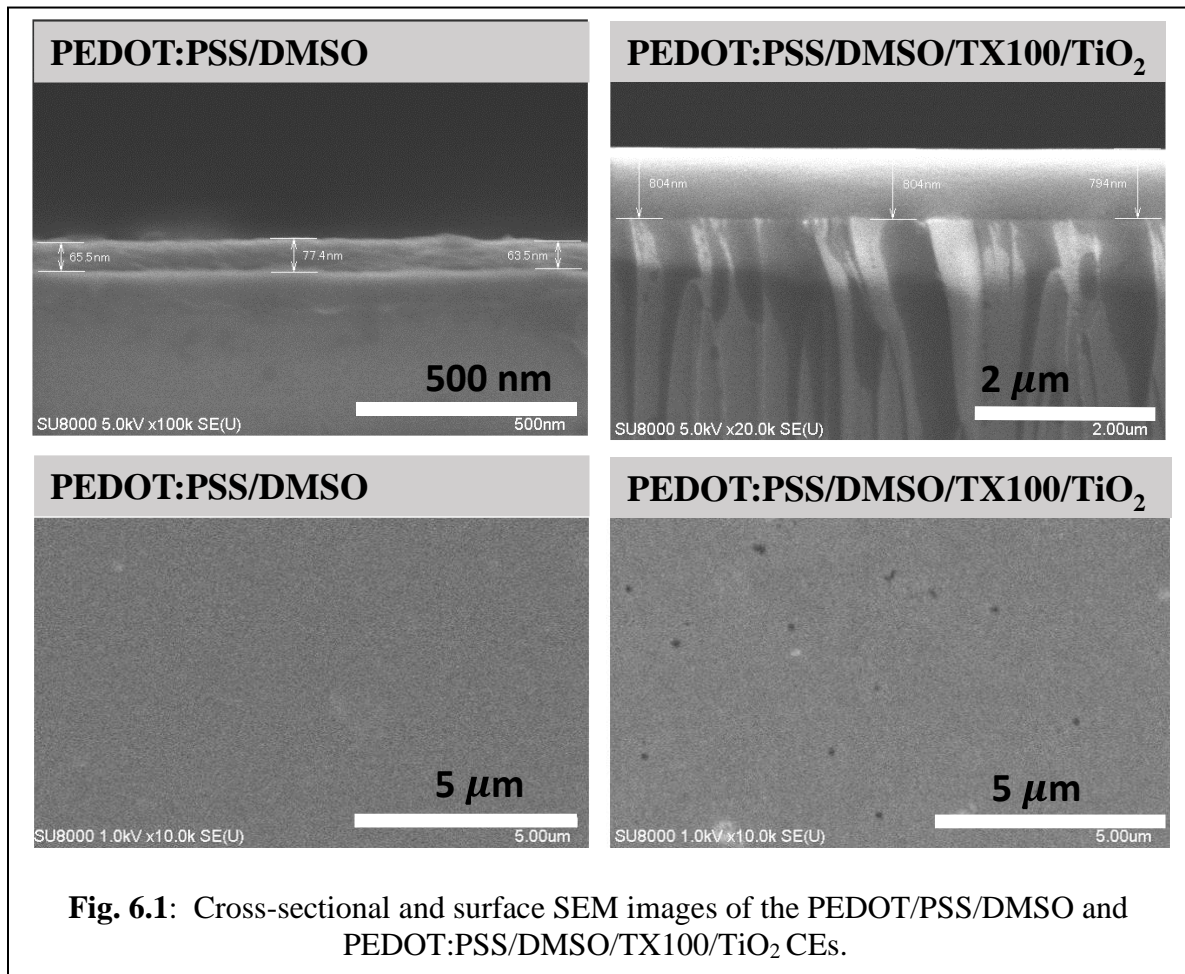
Fig. 6.1: Cross-sectional and surface SEM images of the PEDOT/PSS/DMSO and PEDOT:PSS/DMSO/TX100/TiO$_2$ CEs.

The surface images of the two films show homogenous and smooth morphologies. Compared with the PEDOT:PSS, the PEDOT:PSS/DMSO/TX100/TiO$_2$ film is highly porous as supported by the miniature holes that are spread across the surface of the film, consequently more catalytic active sites are available for more effective iodide/triiodide (I^-/I_3^-) reduction reactions [4, 7, 18]. This structure reinforces the contact with FTO glass and enhances the permeation of the electrolyte [24]. From this, we concluded that the porosity and surface area of PEDOT:PSS can be enhanced through the addition of TiO$_2$ nanoparticles and iso-octyphenoxy-polyethoxyethanol. **Fig. 6.2** shows show AFM topographies of the respective films. The surface roughness of PEDOT:PSS film was 1.28 nm and that of the PEDOT:PSS/DMSO/TX100/TiO$_2$ film was 2.22 nm. The results indicate an increase in surface roughness due to the addition of TiO$_2$ nanoparticles which disrupted the smoothness of the PEDOT:PSS film.

Fig. 6.2:AFM images of the a) PEDOT:PSS and b) PEDOT:PSS/DMSO/TX100/TiO$_2$ electrode.
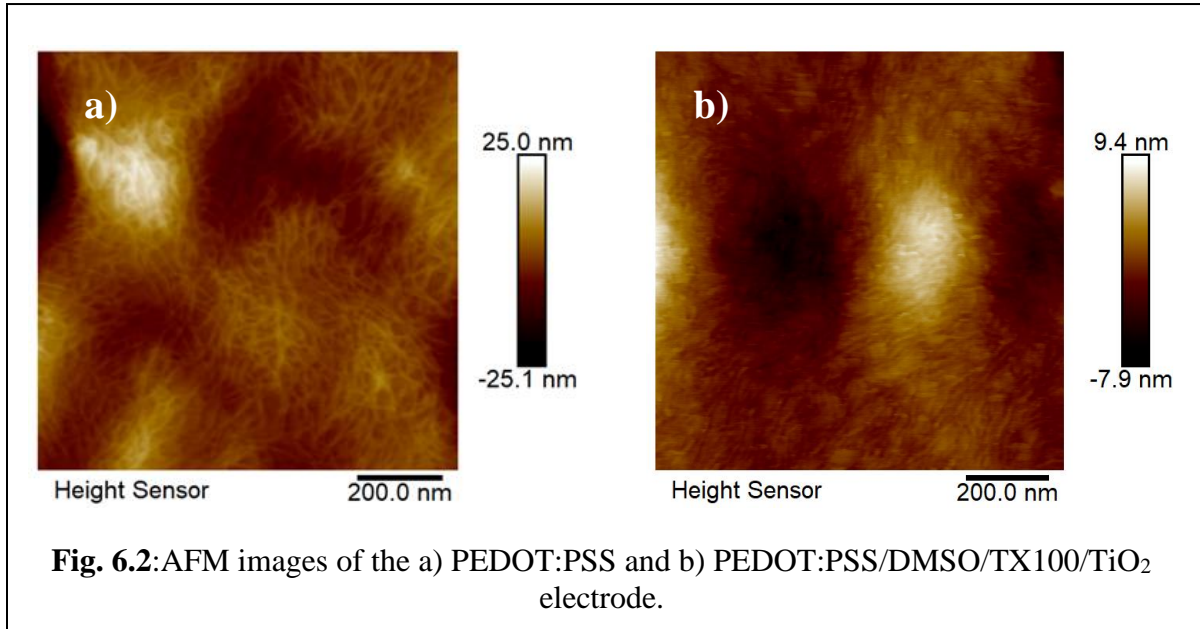
6.3.2 Transmittance and optical properties of the CE

The transmittance of the CE film layer is particularly significant when it comes to bifacial applications. The transmittance of the CE films, influence to a large extent, the overall photovoltaic performance of the DSSC. This is because the incident light must pass through the CE film before being illuminated onto the TiO$_2$ light-harvesting layer. **Figure 6.3** shows the transparency diagram of PEDOT:PSS, PEDOT:PSS/DMSO/TX100/TiO$_2$, and Pt CEs. The transmittance of the CE is conducted in the 300-800 nm light range. From **Figure 6.3**, it can be observed that the PEDOT:PSS films exhibited the highest transmittance followed by the PEDOT:PSS/DMSO/TX100/TiO$_2$ and finally by the Pt film. This is possible because both Triton X-100 [20,25] and PEDOT:PSS [3] have high transmittance in the visible wavelengths.
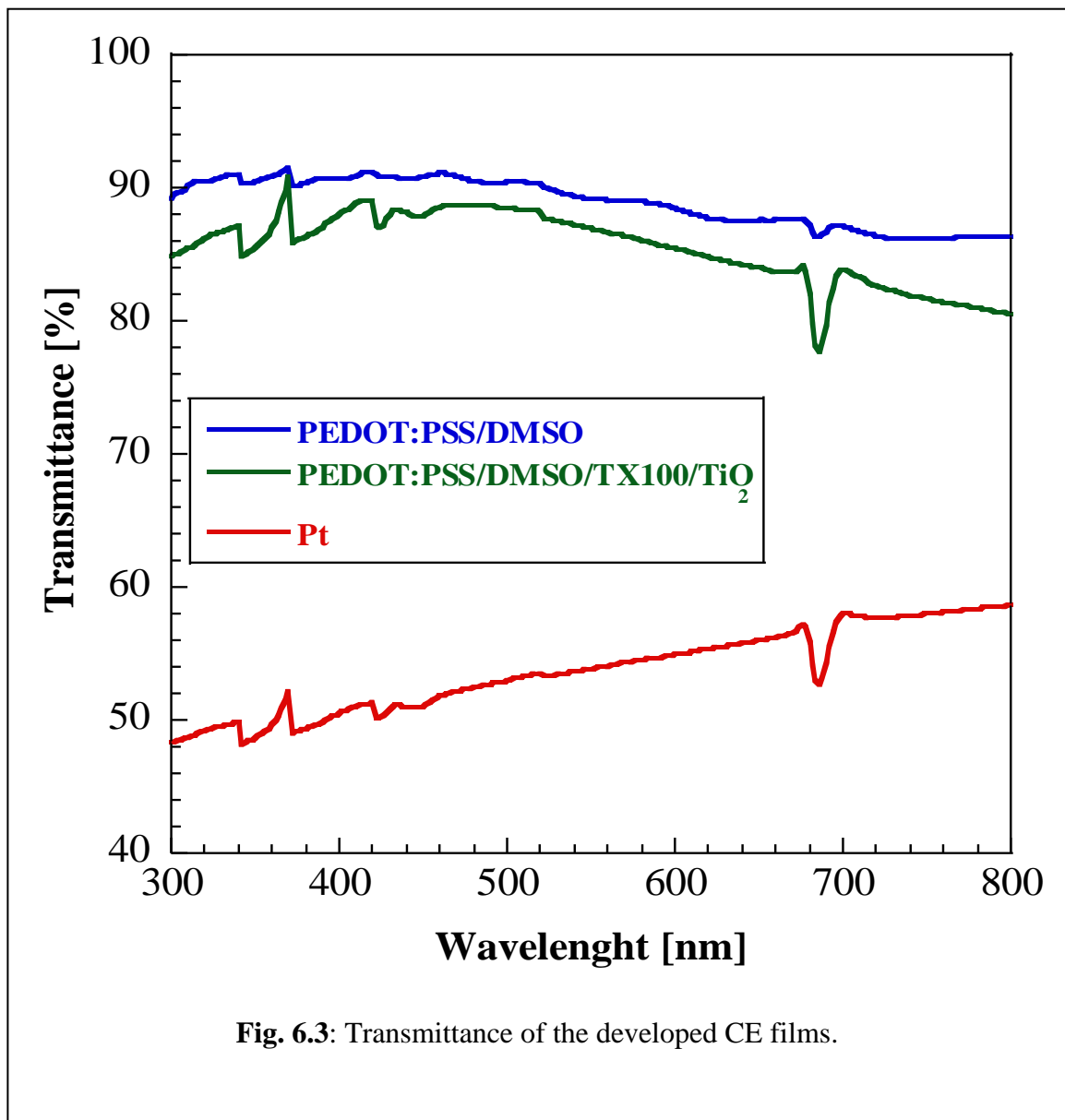
Fig. 6.3: Transmittance of the developed CE films.

6.3.3 Electrochemical activity of the CE

For evaluating electrocatalytic activity, cyclic voltammetry (CV) was set at a scan rate of 100 mVs^{-1} in the potential range from 2 to -2 V [4,17]. **Fig. 6.4a** shows the cyclic voltammograms of the Pt, PEDOT:PSS and PEDOT:PSS/DMSO/TX100/ TiO$_2$ CEs. The cyclic voltammetry for the iodide/triiodide redox shuttle shows twin peaks, a positive and a negative peak. The catalytic activities between electrolyte (I_3^-/I^-) redox couple and the CE are represented by the negative peak whilst the positive peak shows the interaction between the dye and the electrolyte (I_2/I_3^-) [28,29]. The negative and the positive peaks are represented by **Eq. (6.1)** and **Eq. (6.2)** respectively [30]:
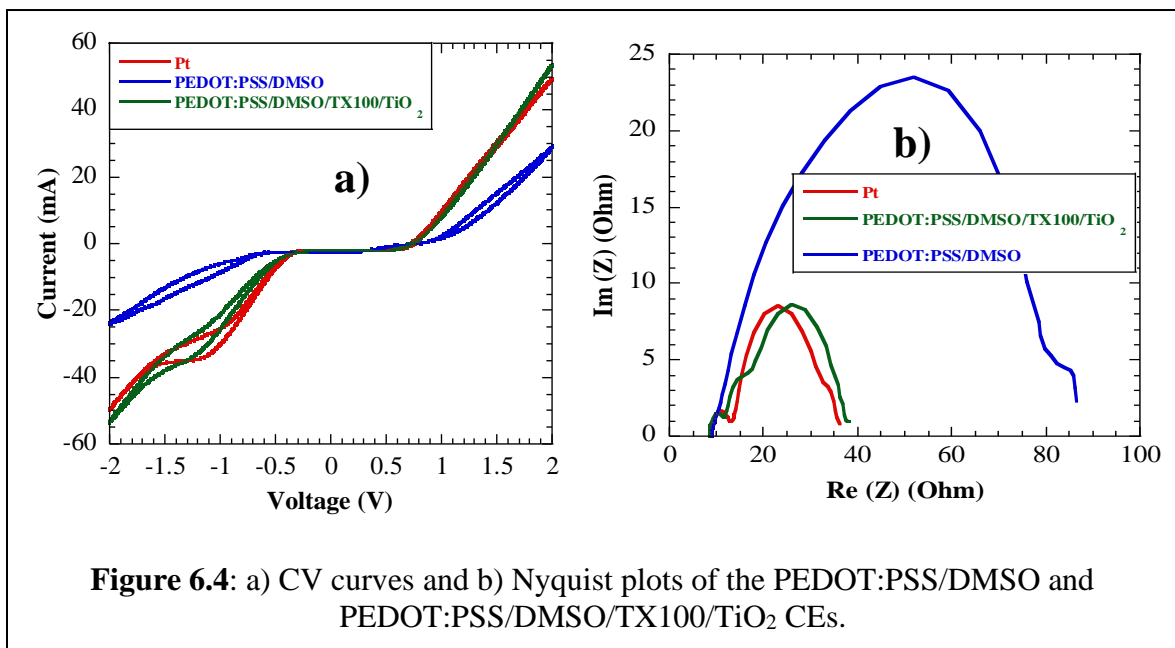
$$I_3^- + 2e^- \leftrightarrow 3I^- \hspace{4cm} (6.1)$$

$$3I_2 + 2e^- \leftrightarrow 2I_3^- \hspace{4cm} (6.2)$$

Figure 6.4: a) CV curves and b) Nyquist plots of the PEDOT:PSS/DMSO and PEDOT:PSS/DMSO/TX100/TiO$_2$ CEs.

Figure 6.4a shows a huge disparity between the CV curves of the PEDOT:PSS and that of the PEDOT:PSS/DMSO/TX100/TiO$_2$ CEs. The negative redox current of I$_3^-$/I$^-$ at the PEDOT:PSS/DMSO/TX100/TiO$_2$ electrode is significantly higher than that at the PEDOT:PSS CE. This indicates that the PEDOT:PSS/DMSO/TX100/TiO$_2$ CE has a faster electrocatalytic activity in the reduction of I$_3^-$ →3I$^-$. Fast electrocatalytic activity leads to the quick transfer of electrons from the CE to the electrolyte which in turn speeds up the recovery of the dye [4]. As a result, electron cycling in the DSSC is sped up increasing the fill factor. On the other side, the overall characteristics of CV curve of the PEDOT:PSS/DMSO/TX100/TiO$_2$ are quite similar to that of the Pt electrode which indicates similar catalytic performance for both CEs. The superior catalytic performance of the PEDOT:PSS/DMSO/TX100/TiO$_2$ can be attributed to its high porosity, high conductivity, and the presence of TiO$_2$ nanoparticles which act as additional catalytic sites on the CE [17,18,23].

Fig.6.3b shows the Nyquist plots of the PEDOT:PSS, PEDOT:PSS/DMSO/TX100/TiO$_2$ and Pt CEs. The Nyquist plot of Pt and PEDOT:PSS/DMSO CE shows two semicircles while the PEDOT/DMSO/TX100/TiO$_2$ CE exhibits three semicircles which are due to the porous nature of these materials [29]. **Table 1** shows the surface resistance and impedance values of the three CEs. These values were obtained after employing the curve fitting tools of the EC-LAB Ver 10.17 software. R$_s$ is the sheet resistance of the substrate. The internal impedance Z$_1$, is represented by the first semicircle and it is related to the charge transportation at the CE/ electrolyte interface. Z$_2$ is the internal impedance represented by the second semi-circle and is related to the charge transfer at the photoanode/electrolyte interface. Z$_3$ is related to the charge transport in the electrolyte, however, it is usually negligible in iodine-electrolyte DSSCs [17]. The total impedance of the DSSC is represented by Z$_T$.

From **Table 6.1**, it can be observed that the PEDOT:PSS CE has the highest Z$_1$ (11.80 Ω) and Z$_2$ (74.81Ω) resistances. On the other hand, the PEDOT:PSS/DMSO/TX100/TiO$_2$ CE has exhibited low Z$_1$ (4.017 Ω) and Z$_2$ (28.67 Ω). This means that there is an increase in conductivity after the addition of Triton X-100 and TiO$_2$ nanoparticles. The Z$_1$ resistance of the PEDOT:PSS/DMSO/TX100/TiO$_2$ CE is lower than that of the Pt CE (4.615) indicating faster

electron transport at the CE/electrolyte interface. Both the PEDOT:PSS/DMSO/TX100/TiO$_2$ CE and Pt CE have low total resistances indicating that they are highly conductive CEs.

Table 6.1: Surface resistance and impedance values of various CEs.

CE TYPE	R$_s$ (Ω)	Z$_1$	Z$_2$	Z$_T$
		Resistance (Ω) Capacitance (μF)	Resistance (Ω) Capacitance (μF)	Resistance (Ω) Capacitance (μF)
Pt	8.97	4.615	24.65	26.61
		2.218	791.9	584.9
PEDOT:PSS/DMSO	8.91	11.80	74.81	77.04
		1.998	653.6	634.6
PEDOT:PSS/DMSO/TX100/TiO$_2$	8.15	4.017	28.67	30.06
		2.549	369.5	352.5

6.3.4 Photovoltaic properties of DSSC

The photocurrent-voltage curves of the DSSCs with the Pt, PEDOT:PSS/DMSO and PEDOT:PSS/DMSO/TX100/TiO$_2$ CEs under simulated solar light are shown in **Fig. 6.5a.** The short-circuit current density (J$_{sc}$), open-circuit voltage (V$_{oc}$), fill factor (FF) and overall cell efficiency (E$_{ff}$) of both the front and rear side of the DSSCs are listed in **Table 6.2**. For comparison, previously reported works on transparent CE have also been included in **Table 6.2**.

In view of frontal illumination, the graph shows that the PEDOT:PSS/DMSO CE DSSC has a high current density (8.123 mAcm^{-2}), however, due to its low electrocatalytic activity, the fill factor of PEDOT:PSS/DMSO is quite low (0.58). The DSSC with Pt CE showed an E$_{ff}$ of 4.49%, a J$_{sc}$ of 8.102 mAcm^{-2}, a V$_{oc}$ of 0.74 V, and an FF of 0.74. In comparison with the DSSC with the Pt CE, the DSSC with the PEDOT:PSS/DMSO/TX100/TiO$_2$ CE exhibited almost the same I-V parameters with E$_{ff}$ of 4.51 %, J$_{sc}$ of 8.424 mAcm^{-2}, V$_{oc}$ 0.74 V, howbeit with a lower FF of 0.72. Considering illumination from the rear side, the DSSCs with PEDOT:PSS/DMSO and PEDOT:PSS/DMSO/TX100/TiO$_2$ CEs, both showed high J$_{sc}$ of 5.139 mAcm^{-2} and 5.638 mAcm$^-$

[2] respectively. However, the FF of the DSSC with the PEDOT:PSS/DMSO (0.67) is still significantly lower than that of the DSSC with the PEDOT:PSS/DMSO/TX100/TiO$_2$ (0.74). On the other side, the DSSC with the Pt CE has a J$_{sc}$ of 4.539 mAcm^{-2} and an FF of 0.69 both of which are lower than those exhibited by the DSSC with the PEDOT:PSS/DMSO/TX100/TiO$_2$ and PEDOT:PSS/DMSO CE. These results conform with the transmittance graphs shown in **Fig. 6.3** of the CEs. The high performance of the PEDOT:PSS/DMSO/TX100/TiO$_2$ CE is due to its high electrocatalytic activity and reduced internal resistance.

Fig. 6.5c shows the performance of developed DSSCs during 16 days. As indicated in the graph, the performance of all three DSSCs decreases with time. There is no significant difference in the degradation rate between the DSSC with the Pt, PEDOT:PSS/DMSO, and PEDOT:PSS/DMSO/TX100/TiO$_2$ CEs. The degradation in cell performance has been attributed to the evaporation and leakage of the electrolyte from the DSSC [17,28].
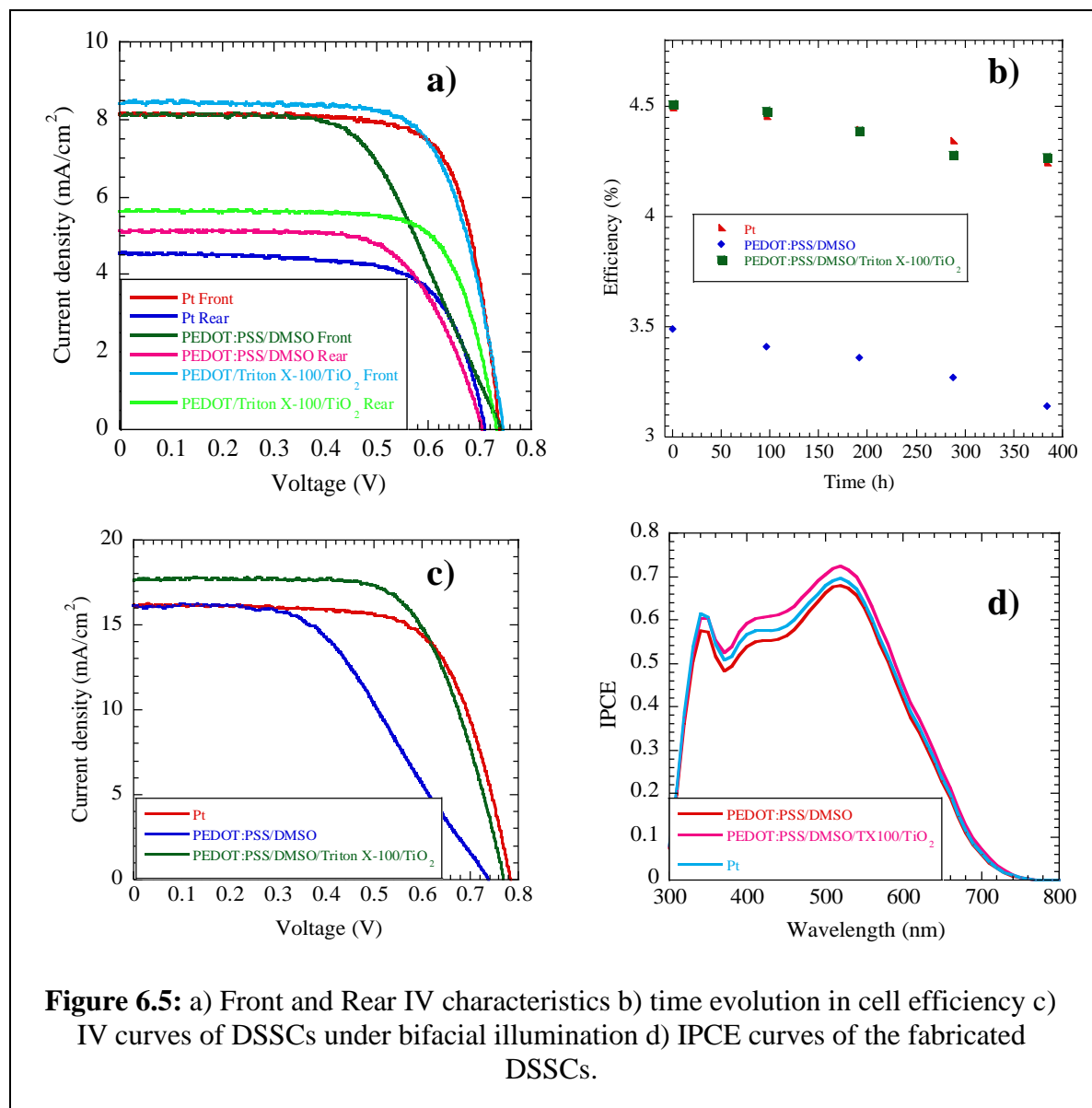
Figure 6.5: a) Front and Rear IV characteristics b) time evolution in cell efficiency c) IV curves of DSSCs under bifacial illumination d) IPCE curves of the fabricated DSSCs.

Table 6.2: DSSC front and rear performance parameters of various CEs.

CE Type	Irradiation	V_{oc} [V]	J_{sc} [A/m^2]	FF	E_{ff} [%]	Retention (%)
Pt	Front	0.74	8.102	0.74	4.49	50 [This work]
	Rear	0.71	4.539	0.69	2.24	
PEDOT:PSS/DMSO	Front	0.74	8.123	0.58	3.49	69 [This work
	Rear	0.71	5.139	0.67	2.42	
PEDOT:PSS/DMSO/TX100/TiO$_2$	Front	0.74	8.424	0.72	4.51	68 [This work]
	Rear	0.73	5.638	0.74	3.05	
PEDOT:PSS/MoS$_2$	Front	0.74	13.73	0.68	7.00	69 [14]
	Rear	0.73	8.75	0.75	4.82	
PANI	Front	0.71	13.08	0.66	6.11	49 [9]
	Rear	0.68	6.11	0.71	3.01	
Polypyrrole	Front	0.72	12.19	0.52	5.74	53 [10]
	Rear	0.72	5.75	0.58	3.06	

To investigate the photovoltaic performance under both frontal and rear irradiation, the setup shown in **Fig. 6.6** was employed. Two reflective mirrors facing each other were placed under a 100 mW/cm^2 simulated solar light. The IV characteristics of the bifacial DSSCs were recorded as the angle of inclination between the mirrors and the horizontal was systematically adjusted from 20° to 70°. The I-V curves under both rear and frontal illumination of DSSCs with Pt, PEDOT:PSS/DMSO/TX100/TiO$_2$, PEDOT:PSS, and Pt CEs are shown in **Fig. 6.5c** while their photovoltaic parameters are listed in **Table 6.3**. The system efficiency (E_{sys}) of the bifacial DSSCs varies with the inclination angle of the mirrors. There is a gradual increase in the efficiency of the DSSC as the angle of inclination is adjusted from 20°-60° after which there is a sharp drop as the angle changes from 60°-70°. **Fig. 6.5d** displays the IPCE curves of the fabricated DSSCs. According to **Fig. 6.5d**, the PEDOT:PSS/DMSO/TX100/TiO$_2$ CE-based DSSC shows better performance than both the Pt CE and PEDOT/DMSO CE-based DSSCs. This is most likely due

to the light scattering effect of the TiO_2 nanoparticles present in the PEDOT:PSS/DMSO/TX100/TiO_2 CE.

Fig.6.6: Schematic of the light splitting design for characterization of bifacial DSSCs.
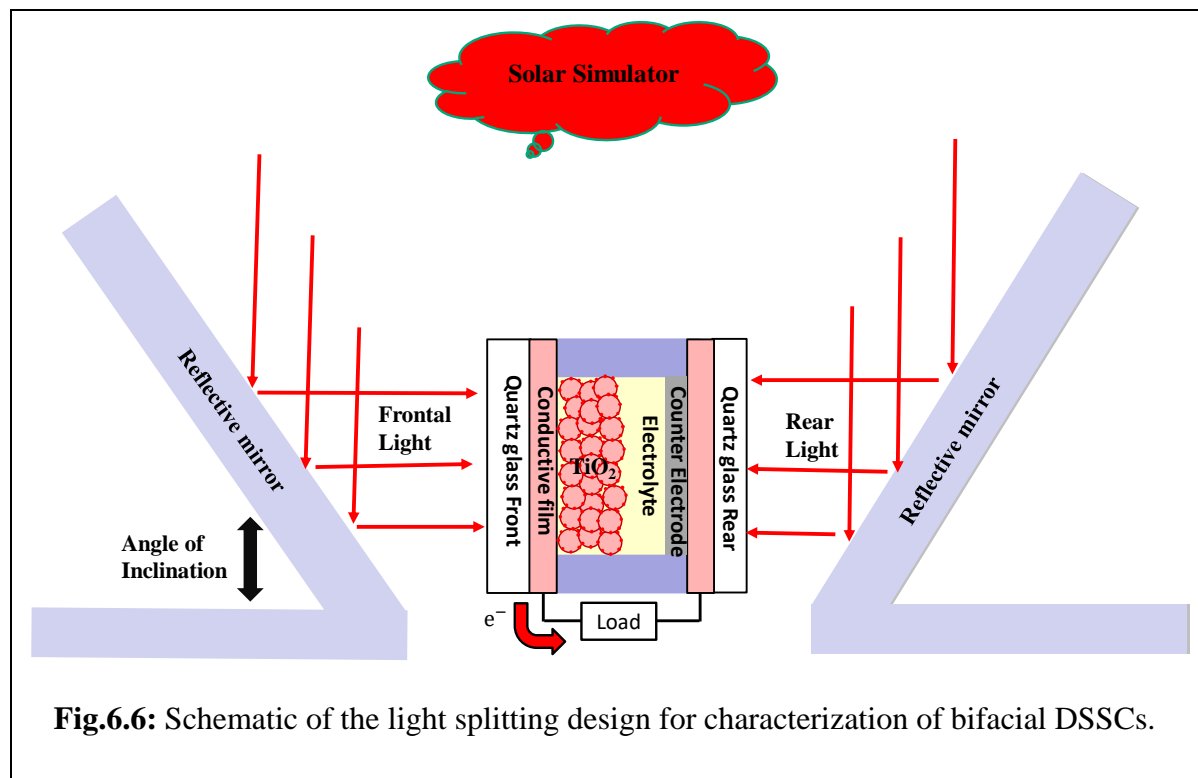
From **Fig. 6.5c** it can be noted that all the three DSSCs exhibit remarkably high current densities under bifacial illumination, with the DSSC with the PEDOT:PSS/DMSO/TX100/TiO_2 exhibiting the highest J_{sc} of 17.724 mAcm^{-2} and E_{sys} of 9.12%. The DSSC with the Pt CE has almost the same J_{sc} (16.15 mAcm^{-2}) as the PEDOT:PSS/DMSO CE which has a J_{sc} of 16.91 mAcm^{-2}. However, the FF value of the PEDOT:PSS/DMSO CE DSSC is quite low (0.49) while that of the Pt CE is 0.69. As a result, there is a large gap in overall cell efficiency between the two DSSCs with Pt CE and PEDOT:PSS/DMSO having E_{sys} of 8.66 % and 6.21 % respectively. The low efficiency of the PEDOT:PSS CE can be attributed to its low catalytic activity and high internal resistance as shown demonstrated by the CV and EIS curves (**Fig. 6.4**). The slightly reduced current density of the Pt CE can be attributed to the reduction in the incident light from the rear side to the reflection of the Pt CE which reduces the number of photogenerated charge carriers [29]. The high performance of the PEDOT:PSS/DMSO/TX100/TiO_2 CE can be attributed to its

fine microporous structure, good electrocatalytic activity, high transmittance, low internal charge resistance on the electrolyte/CE interface, and high transmittance (**Fig. 6.4**).

Table 6.3: DSSC performance parameters of various CEs under bifacial illumination.

CE Type	Inclination angle	V_{oc} [V]	J_{sc} [mA/cm^2]	FF	E_{sys} [%]
Pt	20°	0.76	8.779	0.71	4.76
	30°	0.76	10.387	0.7	5.56
	40°	0.76	10.559	0.7	5.64
	50°	0.76	12.67	0.69	6.68
	60°	0.78	16.152	0.68	8.66
	70°	0.74	12.324	0.71	6.62
PEDOT:PSS	20°	0.71	8.989	0.54	3.46
	30°	0.72	11.101	0.52	4.21
	40°	0.72	12.761	0.52	4.84
	50°	0.74	14.967	0.48	5.32
	60°	0.74	16.149	0.48	5.77
	70°	0.73	12.843	0.52	4.84
PEDOT:PSS/DMSO/TX100/TiO$_2$	20°	0.76	10.214	0.69	5.43
	30°	0.77	11.495	0.69	6.08
	40°	0.77	12.109	0.69	6.47
	50°	0.77	15.679	0.69	8.12
	60°	0.77	17.724	0.67	9.14
	70°	0.74	12.431	0.71	6.65

6.4 Conclusion

To reduce incident losses and make up for the incomplete excitation of the dye in DSSC, there is a need to fabricate efficient and cost-effective bifacial DSSCs with high transmittance. In this study, we prepared a new transparent, and highly effective PEDOT: PSS-based CE. The performance of PEDOT:PSS was enhanced by the addition of Triton X-100 which increased the conductivity, adhesion, and viscosity properties of PEDOT:PSS. In addition, tiny amounts of TiO_2 nanoparticles were added to increase the surface area of the PEDOT:PSS. The combination of PEDOT:PSS, Triton X-100, and TiO_2 resulted in the production of a CE that exhibited low internal resistance, high catalytic activity, and high transmittance. The overall efficiency under bifacial illumination was 9.14% and 8.66% for DSSCs fabricated with the PEDOT:PSS/DMSO/TX100/TiO_2 based CE and Pt-based CE, respectively. The results have shown that the developed PEDOT:PSS/DMSO/TX100/TiO_2 CE matches the performance and is an excellent replacement for the currently employed expensive Pt-based CEs.

6.5 References

[1] B. O'Regan, M. Grätzel, Nature 353 (1991) 737–740. https://doi.org/10.1038/353737a0

[2] M. Grätzel, et al, Journal of Photochemistry and Photobiology A: Chemistry, vol. 164, no. 1–3, pp. 3–14, 2004. https://doi.org/10.1016/j.jphotochem.2004.02.023

[3] X. Wang, L. Zhi, K. Müllen, Nano Lett. 8 (2008) 323. https://doi.org/10.1021/nl072838r

[4] H. Seo, M. Son, S. Hashimoto, T. Tatasaki, N. Itagaki, K. Koga, M. Shiratani, Electrochimica Acta 210 (2016) 880-887. https://doi.org/10.1016/j.electacta.2016.06.020

[5] Wu, C., Li, G., Cao, X., Lei, B., & Gao, X. (2017). Green Energy & Environment, 2(3), 302-309. https://doi.org/10.1016/j.gee.2017.06.002

[6] G.Q. Wang, J. Zhang, S. Kuang, W. Zhang Chem.-Eur. J., 22 (2016), pp. 11763-11769 https://doi.org/10.1002/chem.201601300

[7] I.A. Sahito, K.C. Sun, A.A. Arbab, M.B. Qadir, Y.S. Choi, S.H. Jeong J. Power Sources, 319 (2016), pp. 90-98 https://doi.org/10.1016/j.jpowsour.2016.04.025

[8] Liu, I., Hou, Y., Li, C., & Lee, Y. (2017). Journal of Materials Chemistry A, 5(1), 240-249. https://doi.org/10.1039/C6TA08818J

[9] Wu, J., Li, Y., Tang, Q. et al. Sci Rep 4, 4028 (2014). https://doi.org/10.1038/srep04028

[10] Bu, C., Tai, Q., Liu, Y., Guo, S., & Zhao, X. (2013). Journal of Power Sources, 221, 78-83. https://doi.org/10.1016/j.jpowsour.2012.07.117

[11] X.X. Chen, Q.W. Tang, B.L. He, L. Lin, L.M. Yu Angew. Chem. Int. Ed., 53 (2014), pp. 10799-10803 https://doi.org/10.1002/anie.201406982

[12] G.R. Li, F. Wang, Q.W. Jiang, X.P. Gao, P.W. Shen Angew. Chem. Int. Ed., 49 (2010), pp. 3653-3656 https://doi.org/10.1002/anie.201000659

[13] Cha, S. I., Koo, B. K., Seo, S. H., & Lee, D. Y. (2010). J. Mater. Chem., 20(4), 659-662. https://doi.org/10.1039/B918920C

[14] T. Xu, D. Kong, H. Tang, X. Qin, X. Li, A. Gurung, K. Kou, L. Chen, Q. Qiao, and W. Huang ACS Omega 2020, 5 (15), 8687-8696 https://doi.org/10.1021/acsomega.0c00175

[15] I.K. Popoola, M.A. Gondal, J.M. AlGhamdi and T.F. Qahtan. Sci Rep 8, 12864 (2018). https://doi.org/10.1038/s41598-018-31040-1

[16] C. Wu, R. Li, Y. Wang, S. Lu, J. Lin, Y. Liua and X. Zhang Chem. Commun., 2020,56, 10046-10049 https://doi.org/10.1039/D0CC03744C

[17]   Chawarambwa, F. L., Putri, T. E., Son, M., Kamataki, K., Itagaki, N., Koga, K., & Shiratani, M. (2020). Cplett, 758, 137920. https://doi.org/10.1016/j.cplett.2020.137920

[18]   J.Y. Kim, J.H. Jung, D.E. Lee, Met., 126 (2) (2002), pp. 311-316 https://doi.org/10.1016/S0379-6779(01)00576-8

[19]   G. Yue, J. Wu, J. Wu, Y. Xiao, J. Lin, M. Huang, Electrochimica Acta 67 (2012) 113-118. https://doi.org/10.1016/j.electacta.2012.02.009

[20]   Tevi, T., Birch, S. W., Thomas, S. W., & Takshi, A. (2014). Synthetic Metals, 191, 59-65. https://doi.org/10.1016/j.synthmet.2014.02.005

[21]   J.S. Choi, J.-H. Yim, D.-W. Kim, J.-K. Jeon, Y.S. Ko, Y. Kim. Synthetic Metals, 159 (2009), pp. 2506-2511 https://doi.org/10.1016/j.synthmet.2009.08.049

[22]   K. Fic, G. Lota, E. Frackowiak. Electrochimica Acta, 55 (2010), pp. 7484-7488 https://doi.org/10.1016/j.electacta.2010.02.037

[23]   Ali, A., Malik, N. A., Farooq, U., Tasneem, S., & Nabi, F. (2016). Journal of Surfactants and Detergents, 19(3), 527-542. https://doi.org/10.1007/s11743-016-1800-4

[24]   Chen, J., Wei, H., & Ho, K. (2007). Solar Energy Materials and Solar Cells, 91(15-16), 1472-1477. https://doi.org/10.1016/j.solmat.2007.03.024

[25]   S.H. So, K. Joo, B. R. Kim, B. K. Kim, S. C. Kim, C. D. Shin and I. S. Yeo, Hindawi 7 (2014) 327184 https://doi.org/10.1155/2014/327184

[26]   S. Hwang, J.H. Lee. C. Park. H. Lee, C. Kim, C. Park, M. Lee, J. Park, K. Kim, N. Park, C. Kim, Chem. Commum. (2007) 6550-6560. https://doi.org/10.1039/B709859F

[27]   S. Peng, L. Tian, J. Liang, S.G. Mhaisalkar, S. Ramakrishna, ACS Appl. Mater. Interfaces 4, (2012) 397-404. https://doi.org/10.1021/am201461c

[28]   W. Hong, Y. Xu, G. Lu, C. Li, G. Shi, Electrochem. Commun. 10 (2008) 1555–1558. https://doi.org/10.1016/j.elecom.2008.08.007

[29]   H. Xu, X. Zhang, C. Zhang, Z. Liu, X. Xhou, S. Pang, X. Chen, S. Dong, Z. Zhang, L. Zhang, P. Han, X. Wang, G. Cui, ACS Appl. Mater. Interfaces 4, (2012) 1087-1092. https://doi.org/10.1021/am201720p

[30]   S. Cheng, Y. Hsu, and C. Chen, Journal of the Chinese Institute of Engineers, 33:6, 791-797. https://doi.org/10.1080/02553839.2010.9671669

[31]   T. Qidong; C. Bolei; G. Feng; X. Sheng; H. Hao; S. Bobby; Z., Xing-Zhong ACS Nano (2011), 5(5), 3795-3799 CODEN: ANCAC3; ISSN: 1936-0851

https://doi.org/10.1021/nn200133g

CHAPTER SEVEN: Up-Conversion Performance of Yb^{3+}-Er^{3+}-Zn^{2+}: Y_2O_3 Nanophosphors

7.0 Introduction

Rare earth (RE) doped nanophosphors have gained a lot of attention due to a lot of potential applications ranging from solid-state lighting, fluorescent sensing in biomedical engineering, and light-emitting diodes to the enhancement of solar cell efficiency [1-8]. The research and development of new and effective nanophosphors continue as their demand for glassy and other materials applications continues to rise [1]. Of particular interest, are lanthanide oxides matrix materials. These materials have exhibited remarkably low toxicity, stable chemical properties, and relatively low phonon energy [9-10]. Y_2O_3 has been widely reported as an excellent host material for the doping of RE thanks to its unique properties, such as low phonon energy (600/cm), large exciton binding energy (~156 meV), chemical stability, wide bandgap (~5.8eV), high electron mobility, and low cost of production [11-14]. In addition, the ionic radio of yttrium (Y^{3+}) is comparable to that of RE elements and this unique property enables the effective application of Y_2O_3 as a host material in luminescent nanophosphors [10,15]. In recent years Yb^{3+}, Er^{3+} codoped Y_2O_3 has been synthesized via several different techniques such as solution combustion synthesis, coprecipitation method, propellant synthesis, sol-gel method, flame synthesis, pulsed laser ablation, hydrothermal method [1, 16, 17, 18]. Amongst these techniques, the coprecipitation method is frequently used to prepare oxides because it is easy to control the purity of phase, size distribution, microstructural uniformity, and surface area [1].

The power conversion efficiency of DSSC depends strongly on the utilized sensitizer. The commonly employed dye sensitizers in dye-sensitized solar cells (DSSCs) are ruthenium ion-based with a bandgap of ~1.8 eV and can only absorb a relatively narrow spectral wavelength range. Because of this, the spectral range of the DSSC in the NIR region is limited (300~750 nm) [19,20]. RE up-conversion materials, present an available approach to mitigate the non-absorbable wavelength region of the DSSC via converting near-infrared (NIR) radiation to visible emission [18,21,22]. Up-conversion (UC) refers to a luminescence process through which two or more low-energy infrared photons are absorbed and then converted into a higher-energy visible photon

[23,24]. The most used lanthanide ions utilized in the UC process are the Yb^{3+}, and Er^{3+} codoped materials [25]. In 2015, Du et al prepared Er^{3+}, Yb^{3+} codoped Y_2O_3 nanoparticles which exhibited strong UC at red and green visible wavelengths. Later when the UC nanoparticles were incorporated into the DSSC, the cell showed an enhanced cell efficiency of ~12.4% [26]. In 2017, a study by Wojciech et al [27] achieved UC emission spectra of Yb^{3+}, Er^{3+} codoped lead silicate glasses under infrared excitation at 980 nm. Aside from the popular Er^{3+}/Yb^{3+} UC pair, other ER elements have also been investigated. In 2020, Tadge et al [17], prepared Ho^{3+}, and Yb^{3+} codoped Y_2O_3 nanophosphors. Under IR excitation, these phosphors exhibited strong green and weaker red emissions and when incorporated in the DSSC photoanode, the cell exhibited enhanced cell efficiency of ~10.33%. To date, several UC ER ions and oxide hosts have been utilized for NIR light-harvesting in DSSCs such as Gd_2O_3:Ho^{3+}/Yb^{3+} [9], CeO_2:Er^{3+}/Yb^{3+} hollow sphere [28], $Gd_2(MoO_4)_3$: Er^{3+}/Yb^{3+} [29] and Y_2O_3:Er^{3+} nanorod [30]. These studies have indicated that DSSC incorporating UC materials exhibited better cell performance than the UC material-free DSSC.

To the best of our knowledge, no attempt has been made to investigate the effect of Zn^{2+} concentration on the photoluminescence properties of Er^{3+}, and Yb^{3+} co-doped Y_2O_3. In this study, the concentration of Zn^{2+} has varied from 1-15% while the concentrations of Er^{3+} and Yb^{3+} have been maintained at 1%. Here we endeavored to enhance the Photoluminesce of Er^{3+}, and Yb^{3+} co-doped Y_2O_3 by varying the concentration of Zn^{2+}. This work aimed to determine the optimum Zn^{2+} concentration for the emission of both red and green photoluminescence. The Er^{3+}, Yb^{3+}, and Zn^{2+}: Y_2O_3 nanophosphors were synthesized using a urea-based co-precipitation method.

7.2 Experimental Methods

7.2.1 Materials
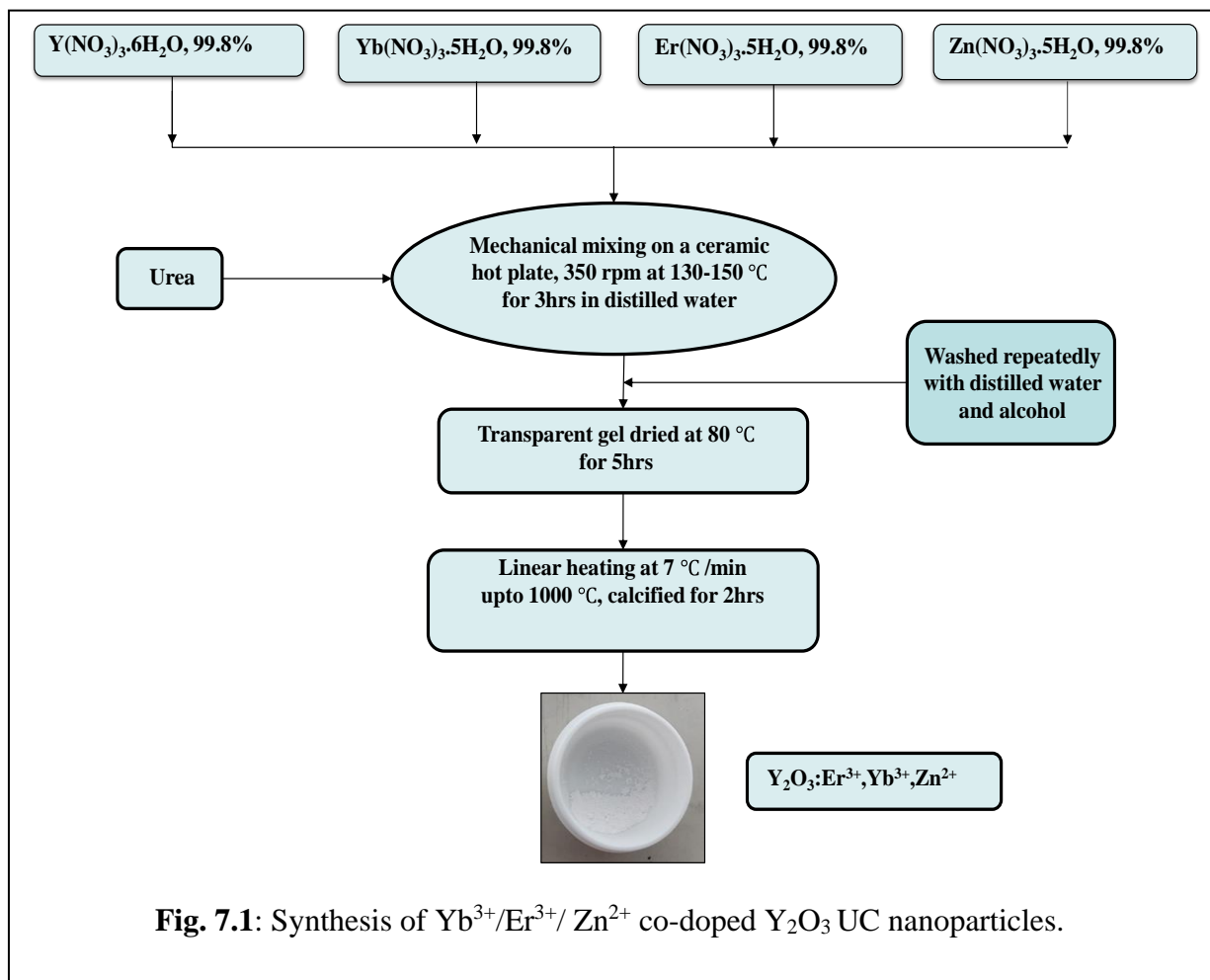
Ytterbium nitrate hexahydrate ($Yb(NO_3)_3 5H_2O$), erbium nitrate pentahydrate (Er $(NO_3)_3 5H_2O$), yttrium nitrate hexahydrate ($Y(NO_3)_3 6H_2O$), zinc nitrate hexahydrate ($Zn(NO_3)_3 5H_2O$), and fluorine tin oxide doped glass substrate (FTO, 7 Ω cm^{-2}) were purchased from SIGMA-Aldrich. Spacer (Meltonix 1170-60), transparent TiO_2 pastes (T/SP), reflective TiO_2 paste (R/SP), cis-dicyano-bis (2,2'-bipyridyl-4,4'-dicarboxylic acid) ruthenium (II) (N719 dye), and iodine electrolyte (AN50)

were purchased from Solaronix, Switzerland. Platinum paste (Dyesol PT1) was purchased from Dyesol. Acetone, super dehydrated ethanol (99.5%), and dimethyl sulfoxide (DMSO) were purchased from Wako. All materials were used as purchased without further modifications.

7.2.2 Preparation of Er^{3+}, Yb^{3+}, Zn^{2+}: Y_2O_3 Nanophosphors

A urea-based facile homogeneous co-precipitation method [26] followed by appropriate thermal treatment was utilized in the preparation of the Y_2O_3: Yb^{3+}, Er^{3+}, Zn^{2+} UC nanophosphors. To optimize UC emission property, both Er^{3+} ion and Yb^{3+} concentration was fixed at 1 mol% while that of Zn^{2+} was varied from 1-5, 10, and 15 mol%. Stoichiometric amounts of high-purity powders $(Y(NO_3)_36H_2O)$, $(Yb(NO_3)_35H_2O)$, $(Er(NO_3)_35H_2O)$, and $(Zn(NO_3)_35H_2O)$, were weighed and dissolved in 50 ml of deionized water (DI) to form a transparent solution. Subsequently, a moderate amount of urea (~1 g) was added, and the mixture was sealed in a beaker with aluminum foil and then heated for 3 hrs. on a ceramic plate at 150℃ under vigorous magnetic stirring at 350 rpm [10]. Next, the precursor was sonicated for 5 mins, centrifuged at 5000rpm for 5 mins, and repeatedly washed with DI and alcohol to remove the remaining ions. The transparent gel was subsequently dried at 80 ℃ for 5 hrs. and then placed in a crucible and sintered in a furnace. The temperature of the precipitate precursor in the furnace was raised at a steady rate of 7℃/minute until it reached 1000°C and then calcified at 1000 ℃ for 2hrs. **Fig. 7.1** shows the schematic diagram of the synthesis process of the Yb^{3+}/Ho^{3+} co-doped Y_2O_3 UC nanoparticles.

Fig. 7.1: Synthesis of $Yb^{3+}/Er^{3+}/Zn^{2+}$ co-doped Y_2O_3 UC nanoparticles.

The flowchart contains the following elements:

- $Y(NO_3)_3.6H_2O$, 99.8%
- $Yb(NO_3)_3.5H_2O$, 99.8%
- $Er(NO_3)_3.5H_2O$, 99.8%
- $Zn(NO_3)_3.5H_2O$, 99.8%

Urea

Mechanical mixing on a ceramic hot plate, 350 rpm at 130-150 ℃ for 3hrs in distilled water

Washed repeatedly with distilled water and alcohol

Transparent gel dried at 80 ℃ for 5hrs

Linear heating at 7 ℃ /min upto 1000 ℃, calcified for 2hrs

$Y_2O_3:Er^{3+},Yb^{3+},Zn^{2+}$

7.2.3 Fabrication of the DSSC

The conventional doctor blade method, as described elsewhere [14] was employed in the fabrication of the DSSCs. Firstly, the substrate FTO glass was sonicated successively in acetone, ethanol, and DI for 20 mins. To prepare the photoanode, transparent TiO_2 colloids were coated on the cleaned FTO surface to form a TiO_2 film using the doctor blade method. The active area of the photoanode was 0.275 cm^2. The wet photoanodes were then sintered at 450°C for 1 hr in an atmospheric furnace. Next, reflective TiO_2 colloids mixed with 2 wt% $Y_2O_3{:}Yb^{3+}$, Er^{3+}, and Zn^{2+} nanophosphors were subsequently screen-printed (by the doctor blade method) on top of the TiO_2 film yielding a second TiO_2 + $Y_2O_3{:}Yb^{3+}$, Er^{3+}, Zn^{2+} layer. The photoanode was sintered for the second time at 450°C for another 1hr. The prepared photoanodes were cooled in the air to room temperature and then soaked in the N-719 dye solution (4 x 10^{-4} M ethanol) for 20 hours to attach dye molecules. For comparison, UC-free TiO_2 film (hereafter referred to as bare TiO_2) was also prepared and then sintered at 450°C for 1 hr. and later soaked in the dye for 20 hours. On the wise, a Pt counter electrode (CE) was prepared on the FTO substrate using Pt paste, followed by heating at 450 ℃ for 30 mins. Eventually, a sandwich-type DSSC was fabricated with the Pt CE, photoanode, and a 60 µm spacing sealant. A liquid iodine electrolyte was injected between the photoanode and the CE through predrilled holes on the CE and the sealing process was completed with the help of a hot press [31].

7.2.4 Characterization Methods

The phase purity of the prepared nanophosphors was identified by using a powder X-ray diffractometer (XRD) (Bruker, D8 Advance) with Cu Kα irradiation (λ = 1.5418 Å), in the range $20° \leq 2\theta \geq 60°$. The morphology of the prepared UC nanophosphor samples was characterized using an SEM (Hitachi, SEM3500). The photoluminescence (PL) spectra of the UC nanophosphors were recorded in the range 500-800 nm using a NIR laser diode with an excitation wavelength of 980 nm. To determine the photovoltaic characteristics of the prepared DSSCs (at room temperature, 1 sun illumination, and an A.M of 1.5), a solar simulator with a 1000 W Xeon short arc lamp was utilized. The EQE of the prepared DSSCs in the spectra ranges 300 nm ~ 800 nm was evaluated using a Xeon arc lamp as the light source combined with a monochromator.

7.3 Results and Discussion

7.3.1 Crystal structure and phase purity by XRD

The XRD patterns of Yb^{3+}, Er^{3+}, and Yb^{3+}, Er^{3+}, and Zn^{2+} codoped Y_2O_3 nanophosphors calcified at 1000 °C are shown in **Fig. 7.2a**. The main peaks are indexed to the body-centered cubic phase Y_2O_3 and are well agreed with the JCPDS file no. 25-1200. It was concluded that the synthesized samples are well crystalline, and no additional peaks were observed upon Zn^{2+} doping. Furthermore, the sample with Zn^{2+} appears to have more defined sharp diffraction peaks which suggest the improved crystallinity of Y_2O_3 after Zn^{2+} codoping [32]. The slight shifting of diffraction peak (222) shown in **Fig. 7.2b** confirms the retrenchment of the unit cell volume caused by the substitution of Y^{3+} (ionic radii ~90) with Zn^{2+} (ionic radii ~74 pm) ions [5,32,33].
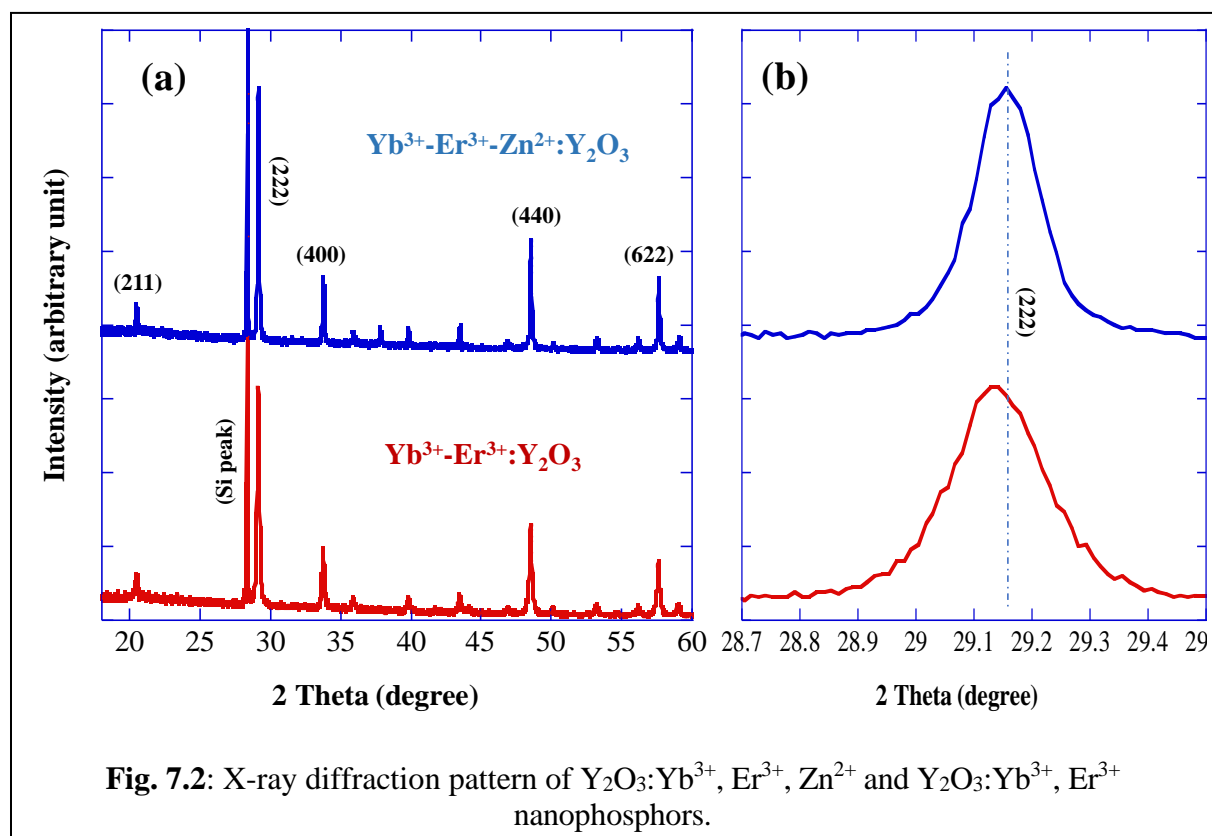
Fig. 7.2: X-ray diffraction pattern of Y_2O_3:Yb^{3+}, Er^{3+}, Zn^{2+} and Y_2O_3:Yb^{3+}, Er^{3+} nanophosphors.

7.3.2 Photoluminescence

The photoluminescence spectra of synthesized $Y_2O_3:Yb^{3+}, Er^{3+}, Zn^{2+}(x\%)$ (x = 1-5, 10, 15) samples measured under 980 nm excitation at room temperature are presented in **Fig. 7.3**. **Fig. 7.4** shows the PL of the UC without Zn^{2+} and $Y_2O_3:Yb^{3+}, Er^{3+}, Zn^{2+}(5\%)$. Green and red UC photoluminescence spectra of Er^{3+} ions were observed under the excitation of Yb^{3+}. The observed green and red emission bands centered at about 670 nm and 550nm correspond to the $^4F_{9/2} \rightarrow ^4I_{15/2}$ and $^2H_{11/2}$, $^4S_{3/2} \rightarrow ^4I_{15/2}$ transitions of Er^{3+} [27]. Yb^{3+} is a common sensitizer in the UC emission of Er^{3+} and has a high absorption cross-section (11.7 x 10^{-21} cm^2) in the NIR region [17]. The unique intrinsic properties of Yb^{3+} enable it to efficiently transfers its energy to Er^{3+} ions [10]. Because Er^{3+} ions have no resonant absorption at 980 nm, the appearance of the Er^{3+} emission peak in $Y_2O_3:Yb^{3+}$, Er^{3+}, and Zn^{2+} nanophosphors on excitation by 980 nm is a sure indicator that energy has been transferred to Er^{3+} from Yb^{3+} ions [17].
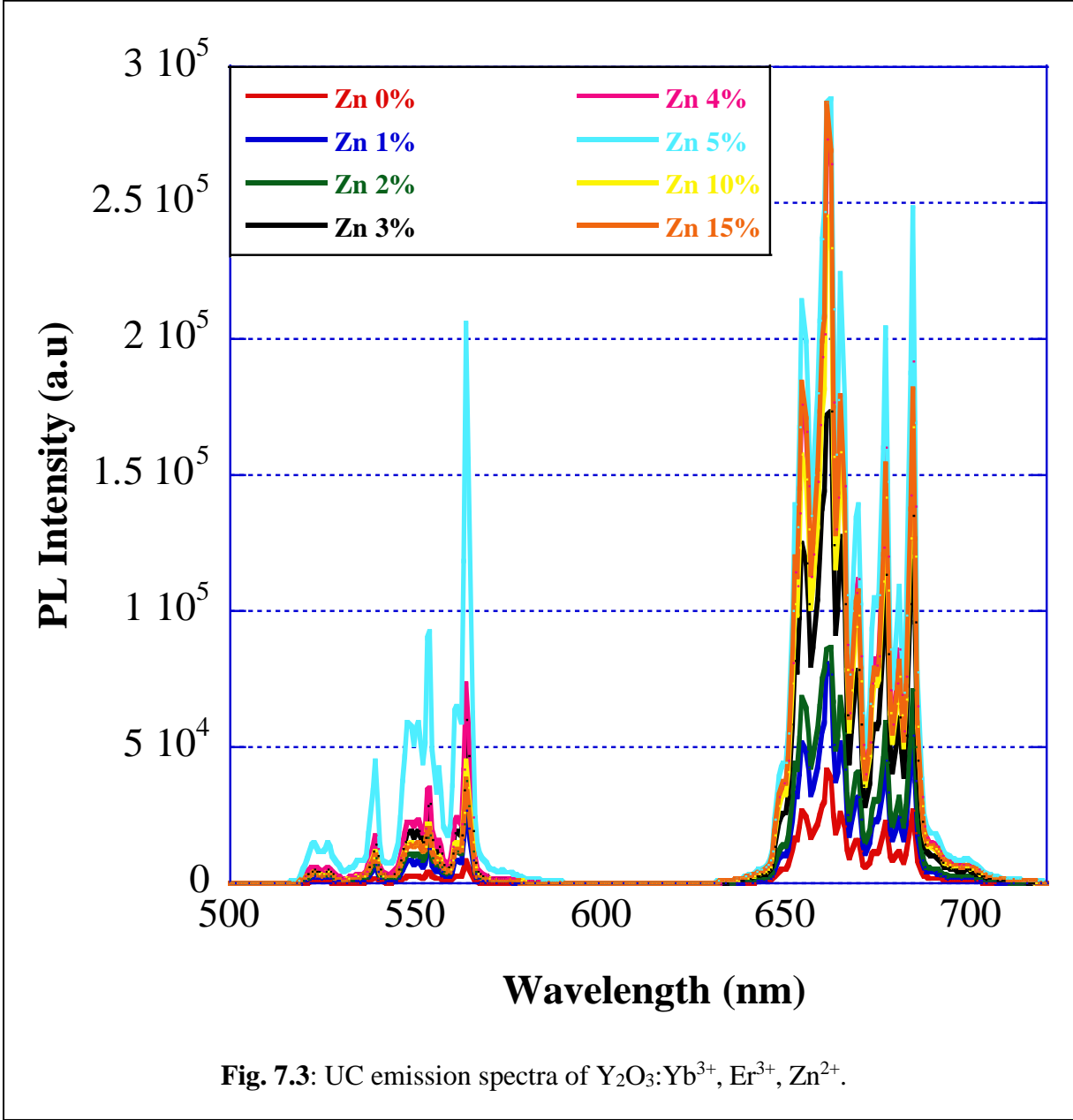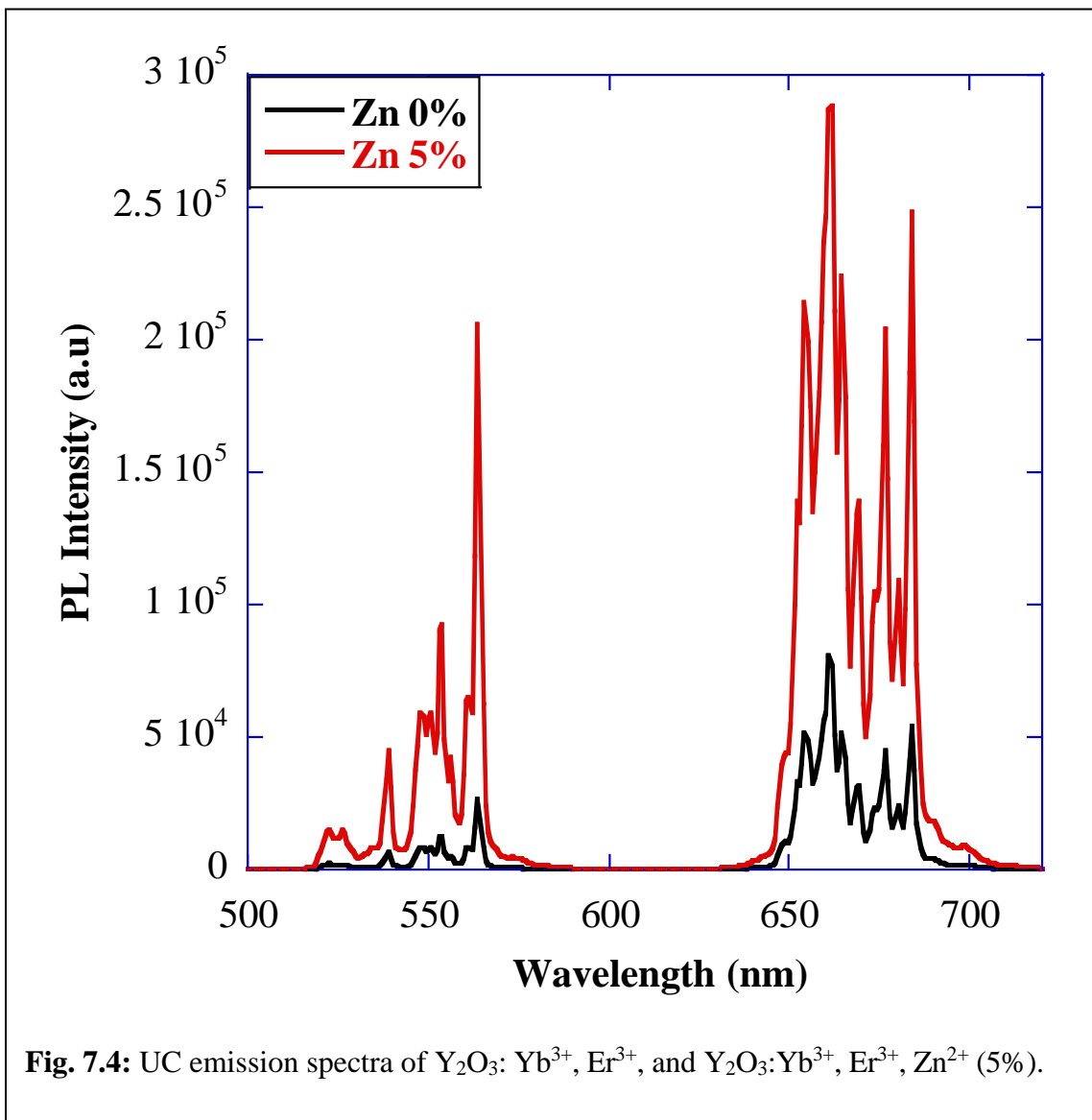
Fig. 7.3: UC emission spectra of Y_2O_3:Yb^{3+}, Er^{3+}, Zn^{2+}.

Fig. 7.4: UC emission spectra of Y_2O_3: Yb^{3+}, Er^{3+}, and Y_2O_3:Yb^{3+}, Er^{3+}, Zn^{2+} (5%).

It was observed in **Fig. 7.3**, that the concentration of Zn^{2+} influences both the red and green UC photoluminescence spectra of Er^{3+} ions in Y_2O_3. The optimum UC emission was determined at a 5% concentration of Zn^{2+}. The addition of Zn^{2+} to $Y_2O_3:Yb^{3+}$ heightened the UC emission intensities by ~6.92 times and ~25.3 times in the red and green bands respectively. This significant increase in UC emission is a direct result of the presence of the local field around the Er^{3+} ions followed by the substitutional effect [33]. Y^{3+} has a much larger ionic radius of about 90 pm when compared to that of Zn^{2+} (~74 pm) and this leads to the substitution of Y^{3+} ions by the Zn^{2+} ions thereby inducing the contraction in the host lattice. Owing to this substitutional effect, the local crystal field symmetry around the Er^{3+} ion was modified [33]. Further, an increase in the Zn^{2+} concentration results in the reduction of the UC emission over the green emission region. This may be ascribed to the concentration-quenching effect [34].

Table 7.1: Intensity ratio of red to green emissions and CIE coordinates of $Y_2O_3:Yb^{3+}$, Er^{3+}, Zn^{2+}.

Phosphor Samples	Red/Green Ratio	CIE Coordinates (X, Y)
Yb^{3+}, Er^{3+}, Zn^{2+} (0%)	5.087	0.543, 0.447
Yb^{3+}, Er^{3+}, Zn^{2+} (3%)	2.866	0.499, 0.492
Yb^{3+}, Er^{3+}, Zn^{2+} (5%)	1.391	0.499, 0.492
Yb^{3+}, Er^{3+}, Zn^{2+} (10%)	5.441	0.499, 0.492
Yb^{3+}, Er^{3+}, Zn^{2+} (15%)	7.518	0.499, 0.492

The red-to-green ratio of the synthesized $Y_2O_3:Yb^{3+}$, Er^{3+}, and Zn^{2+} nanophosphors at various concentrations of Zn^{2+} ions are shown in **Table 7.1.** The Table shows that the ratio of intensities of red to green emissions of Er^{3+} ions in Er^{3+}, Yb^{3+} codoped Y_2O_3 have been significantly affected by the changes in Zn^{2+} concentrations. There was a gradual decrease in the red/green emission ratio as the concentration of Zn^{2+} was increased from 0-5% which indicates that there was a decrease in the purity of the red color emitted from the UC nanophosphors. From **Fig. 7.5**, it was observed that the color coordinates shift towards the lesser pure red (yellowish) as the of Zn^{2+} was increased from 0-
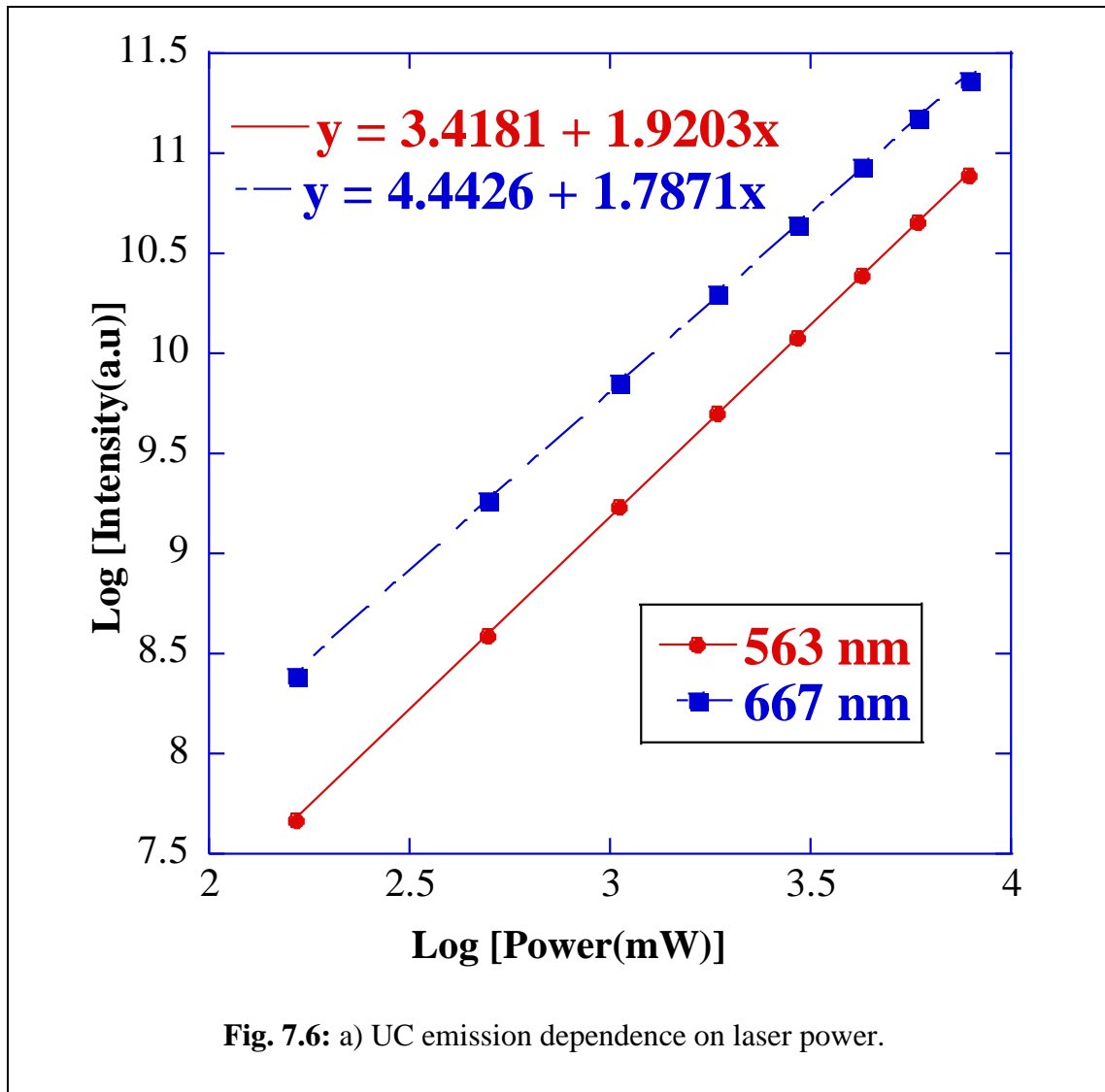
5%. Conversely, when the concentration of Zn^{2+} is further increased to 10% and later 15%, there is an increase in the purity of the red color emitted from the synthesized UC samples. The variations in color emitted from the nanophosphor samples can be observed more clearly from the CIE chromaticity diagram shown in **Fig. 7.5**.


Fig. 7.5: CIE colour coordinates of Y_2O_3:Yb^{3+}, Er^{3+}, and Y_2O_3:Yb^{3+}, Er^{3+}, Zn^{2+} nanophosphors.
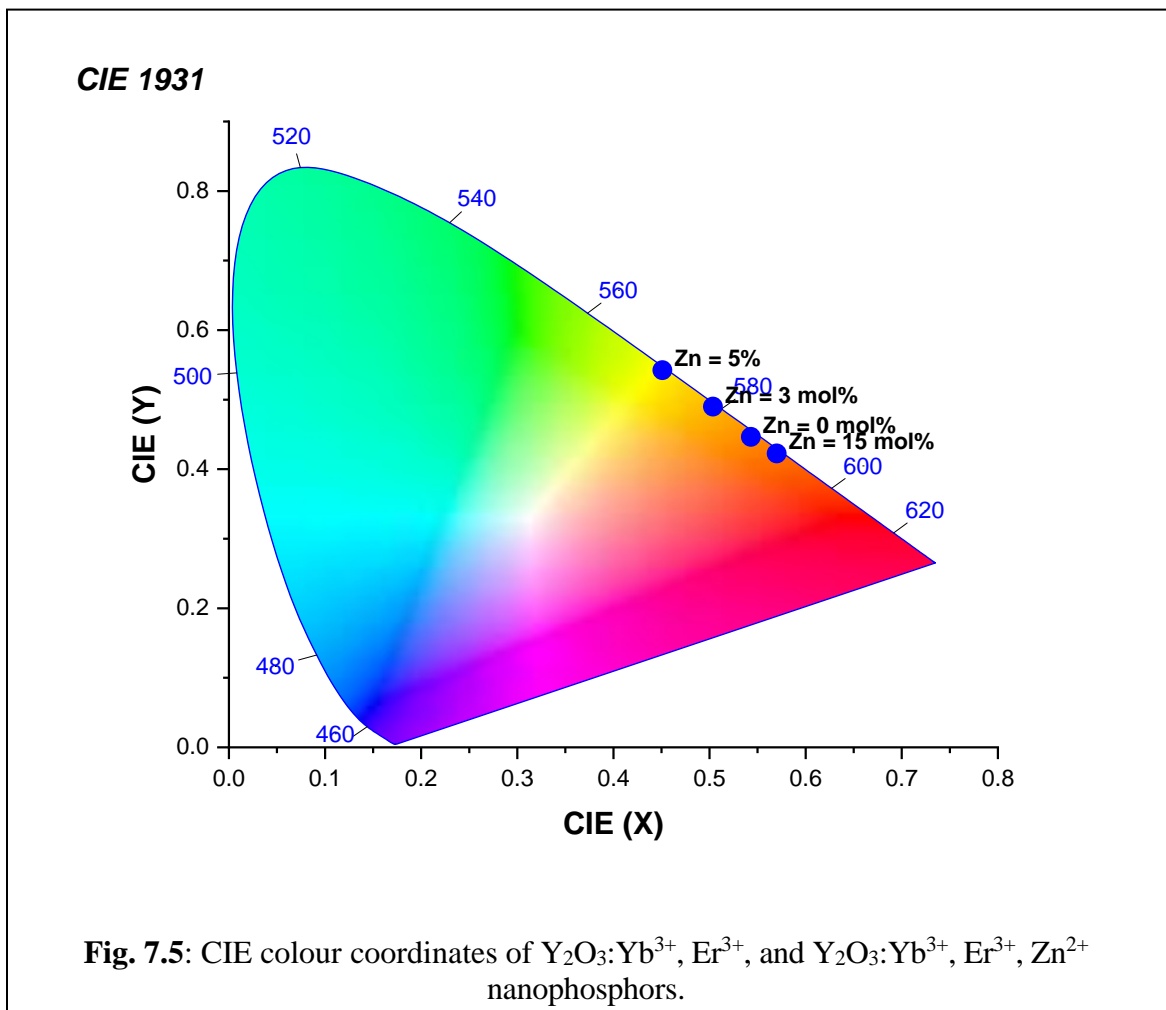
The CIE chromaticity diagram was plotted with the aid of the Origin CIE Chromaticity app. From this figure, it can be observed that the color coordinates shift towards the lesser pure red (yellowish) region in the case of Zn^{2+} codoped Y_2O_3:Yb^{3+}, Er^{3+}, indicating a decrease in the purity of red color emitted from the synthesized nanophosphors.

The mechanism of the up-conversion process was examined based on Ln-Ln plots of visible photoluminescence vs the power of the IR excitation light (shown in **Fig. 7.6**). The Ln-Ln dependence of up-conversion emission intensities for the ${}^4S_{3/2} \rightarrow {}^4I_{15/2}$ (green) and ${}^4F_{9/2} \rightarrow {}^4I_{15/2}$ (red) transaction of Er^{3+} on the excitation power was determined following the relation shown in **Eq. 7.1**:

$$I_{UPC} = P_{pump}^n \qquad\qquad (7.1)$$

y = 3.4181 + 1.9203x
y = 4.4426 + 1.7871x

563 nm
667 nm

Fig. 7.6: a) UC emission dependence on laser power.

Where P is the incident laser power, n is the number of photons involved in the UC process and I_{UPC} is the UC-integrated luminescence intensity [27]. The value of the slope is determined by plotting $Ln\ (I)$ vs. $Ln\ (P)$ [35]. The power-dependent plots for the two different transitions are shown in **Fig. 7.6**. An important observation is that the value of color coordinates at different laser pump powers are similar, and this indicates that there is no color tunability in this present phosphor [33].

Fig. 7.7: Energy transition diagram for Yb^{3+}, and Er^{3+}.
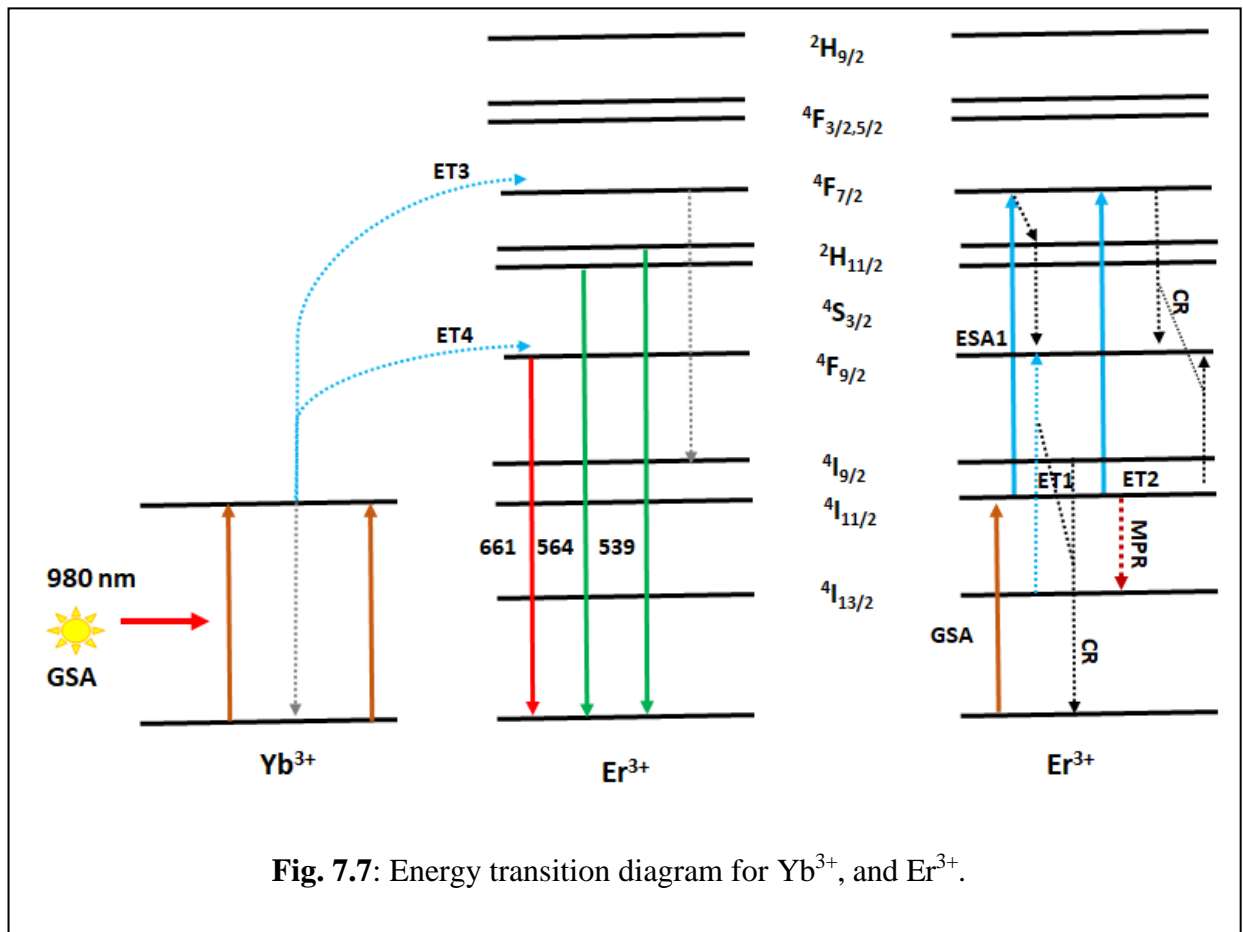
The energy level transition diagram of the Er^{3+} and Yb^{3+} ions and their possible transitions scheme are shown in **Fig. 7.7**. The UC process of Er^{3+} and Yb^{3+} ions consists of a 2-photon mechanism [36]. Two-step energy transfer (ET) from $Yb^{3+} \rightarrow Er^{3+}$ ions tied with other processes such as the ground-state absorption (GSA), excited state absorption (ESA), and cross-relaxation (CR) is responsible for the filling of the $^2H_{12/2}$, $^4S_{3/2,}$ and $^4F_{9/2}$ excited states of the trivalent Er [37]. In Y_2O_3, the ET processes are much more efficient when compared to the ESA process [36, 37].

To begin with, the $^4I_{11/2}$ state of the Er^{3+} ion is populated through GSA of 980 nm photons coupled with energy transfer from Yb^{3+} to the Er^{3+} ions. In the second step, an interaction between excited Er^{3+} and Yb^{3+} ions raises the excitation of trivalent Er from the $^4I_{11/2} \rightarrow {}^4F_{11/2}$ state. Subsequently, a multi-phonon relaxation then quickly transfers the excitation energy from the $^4F_{7/2} \rightarrow {}^2H_{11/2}$, $^4S_{3/2}$ states of Er^{3+} [26]. A portion of this excitation energy relaxes radiatively from the $^2H_{11/2}$, $^4S_{3/2} \rightarrow {}^4I_{15/2}$ ground state through the emission of green light. At the same time, another portion of the excitation energy is dissipated through nonradiative relaxation and gives rise to the emission of red light and this is related to the $^4F_{9/2} \rightarrow {}^4I_{15/2}$ Er^{3+} transition. According to the study by Ge *et al* [1] surface defects such as OH^- and CO_3^{2-} groups enhance nonradiative relaxation rate which in turn leads to relatively stronger red emissions. Moreover, to account for the feeding of the Er^{3+}, $^4F_{9/2}$ state, several cross-relaxation (CR) routes have been proposed in **Fig. 7.7**.

7.3.3 EDX and SEM

The EDX spectra and SEM images of the synthesized Y_2O_3:Er^{3+}(1%), Yb^{3+}(1%), Zn^{2+}(1%) nanophosphors are shown in **Fig. 7.8** and **Fig. 7.9** respectively. The EDX spectra confirm the presence of Y^{3+}, Er^{3+}, $Yb^{3+,}$ and Zn^{2+} ions in the synthesized UC nanophosphors. To determine the surface morphology of the synthesized samples, SEM images of Y_2O_3:Er^{3+}, Yb^{3+}, and Zn^{2+} nanophosphors calcified at 1000℃ were recorded and are shown in **Fig. 7.9**. From the surface image, the nanoparticles are in an agglomerated form with their size in the nanometer range. To establish the effect of the synthesized UC nanophosphors on the photovoltaic performance of the DSSCs, Y_2O_3:Er^{3+}, Yb^{3+}, and Zn^{2+}(5%) nanophosphors were dispersed in the reflective TiO_2 film to produce a UC photoanode. The surface morphologies of bare TiO_2 and UC TiO_2 films are shown in **Fig. 7.10**. Both films are highly porose and are well distributed across the FTO substrate. There

were no major morphological differences observed between the UC TiO_2 and the bare TiO_2. Therefore, it was concluded that the light scattering effects of the UC nanophosphors on the cell performance of the DSSC were limited.
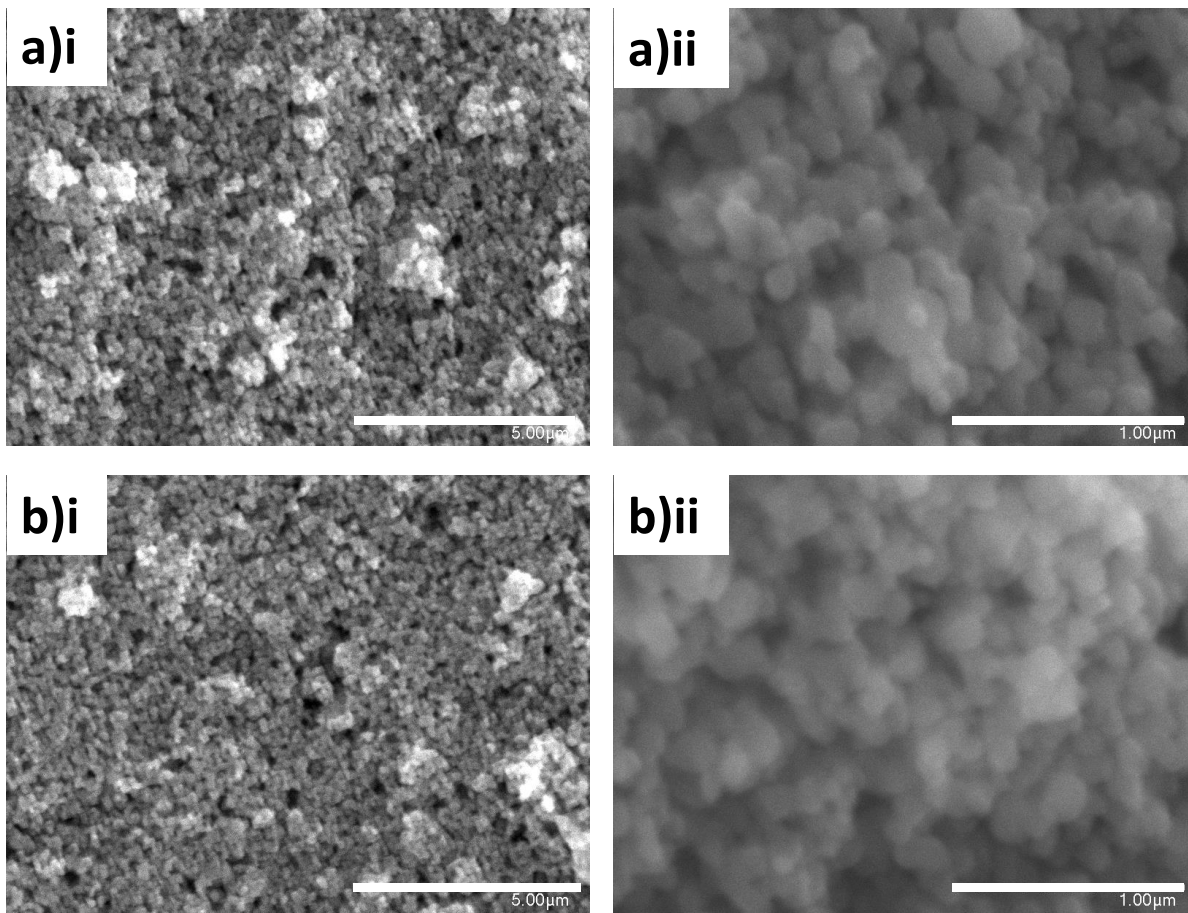
Fig. 7.9: EDX spectra of the fabricated Y_2O_3:Er^{3+}, Yb^{3+}, Zn^{2+} nanophosphors.

Fig. 7.9: Surface SEM images of the synthesized Y_2O_3:Er^{3+}, Yb^{3+}, Zn^{2+}
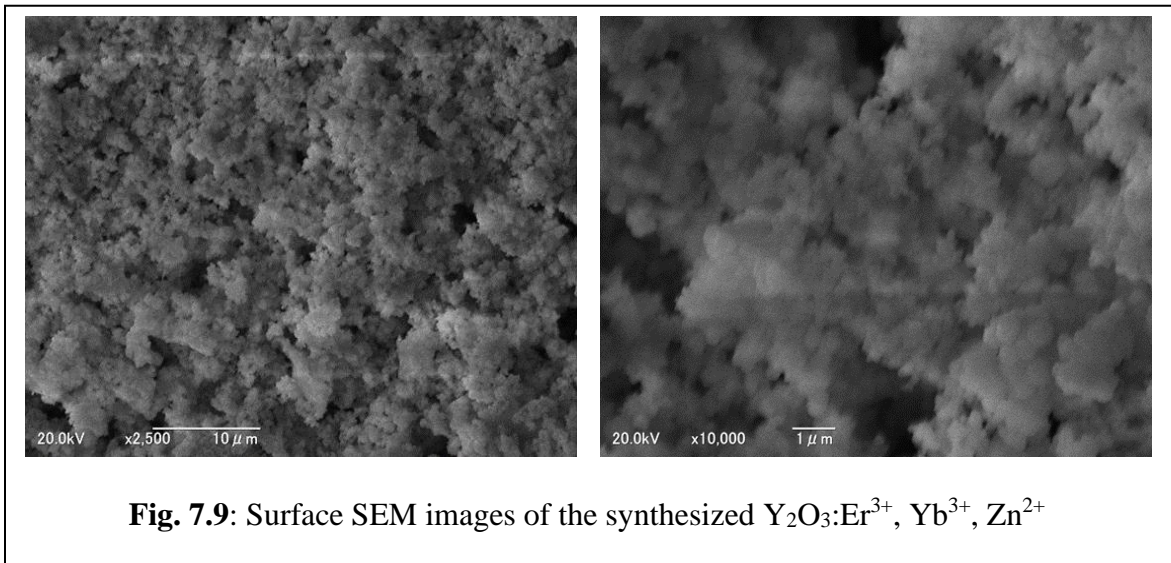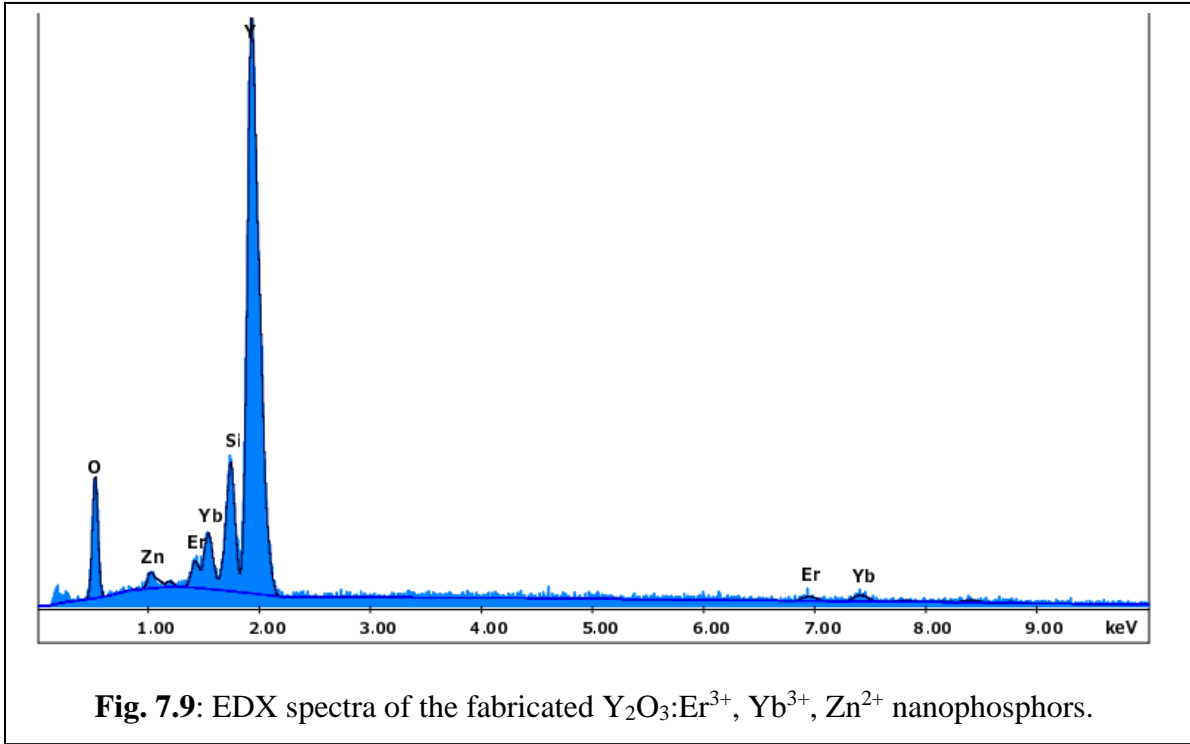
Fig. 7.10: Surface morphologies of a bare TiO_2 b) UC TiO_2.

7.3.4 Photovoltaic performance of the DSSCs

Fig 7.11a shows the J-V curves of the DSSCs with and without the addition of $Y_2O_3:Er^{3+}$, Yb^{3+}, and Zn^{2+} nanophosphors. The main photovoltaic parameters affecting the performance of a solar cell are short-circuit current density (J_{sc}), open-circuit voltage (V_{oc}), and fill factor (FF). All these parameters must be maximized to optimize the performance of the solar cell. The photovoltaic parameters of the fabricated DSSCs are summarized in **Table 7.2**. The bare TiO_2 DSSC has an efficiency of 7.58%. In contrast, the DSSC with the UC, $TiO_2/Y_2O_3:Er^{3+}$, Yb^{3+}, Zn^{2+}(5%) photoanode exhibited enhanced J_{sc}, $V_{oc,}$ and overall cell performance (a significant PCE increment ratio of ~16.6%). This was largely due to the considerable enhancement in the current density ratio of ~17.4% facilitated by the efficient UC emissions of Er^{3+} ions from NIR light to visible light [26,38]. In line with previous studies, the incidence light wavelength range significantly affects the J_{sc} of the DSSC [10, 26]. In this study, $Y_2O_3:Er^{3+}$, Yb^{3+}, and Zn^{2+} UC nanophosphors have a strong light absorption in the NIR region, and consequently, energy can be transferred to the visible region via the UC process leading to the extension of the absorption range of the DSSC [9]. EQE is an important parameter for DSSC as it directly shows how efficiently the DSSC converts the incident photons to electrons. As shown in **Fig. 7.11b**, the EQE of the DSSC with UC nanophosphors was much higher than that of the DSSC with pure TiO_2. These results coincide well with the results of J-V curves in **Fig 7.11a**, indicating that J_{sc} was enhanced owing to the introduction of $Y_2O_3:Er^{3+}$, Yb^{3+}, and Zn^{2+} nanophosphors into the TiO_2 film.

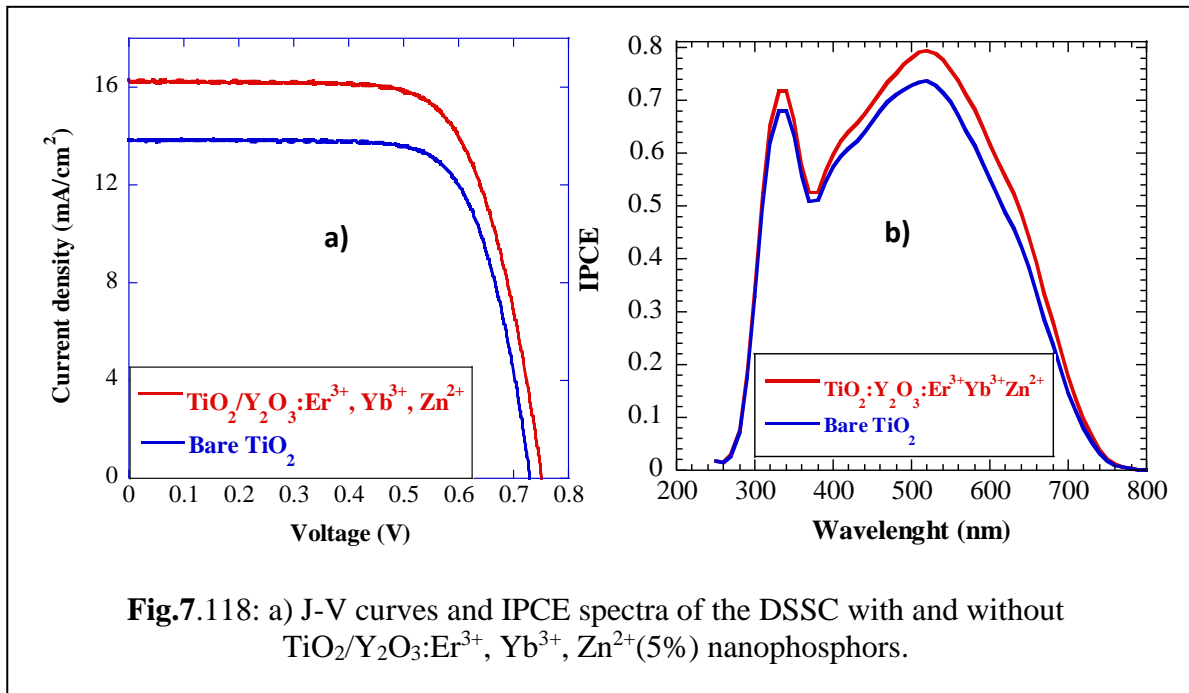**Fig.7**.118: a) J-V curves and IPCE spectra of the DSSC with and without $TiO_2/Y_2O_3:Er^{3+}, Yb^{3+}, Zn^{2+}(5\%)$ nanophosphors.

Table 7.2: DSSC performance parameters.

Photoanode	V_{oc} [V]	J_{sc} [mA/cm^2]	FF	E_{ff} [%]
Bare TiO$_2$	0.73	13.82	0.72	7.33
TiO$_2$/Y$_2$O$_3$:Er^{3+}, Yb^{3+}, Zn^{2+} (5%)	0.75	16.23	0.70	8.55

7.4 Conclusion

In summary, Er^{3+}, Yb^{3+}, Er^{3+}, Yb^{3+}, and Zn^{2+} doped Y_2O_3 UC nanophosphors were synthesized using a urea-based homogeneous coprecipitation method. The developed UC nanophosphors were characterized using SEM, XRD, and PL under IR radiation. The prepared samples emitted intense red and weaker green emissions corresponding to the $^4F_{9/2}{\rightarrow}^4I_{15/2}$ and $^2H_{11/2}$, $^4S_{3/2}{\rightarrow}^4I_{15/2}$ transitions respectively. The enhanced PL emission by the UC nanophosphors in the green region has been achieved by increasing the concentration of Zn^{2+} ions. The ratio of red to green emission of decreases from 5.067 to 1.391 by increasing the Zn^{2+} concentration from 0% to 5% in Y_2O_3:Er^{3+}, Yb^{3+}, Zn^{2+}. The color point of Y_2O_3:Er^{3+}, Yb^{3+}, and Zn^{2+} nanophosphor can be tuned from the near red region to the yellow region under 980 nm excitation by varying the concentration of Zn^{2+} dopants. To investigate the influence of the synthesized UC nanophosphors on the photovoltaic performance of the DSSC, the UC nanophosphors were incorporated in the photoanode of the DSSC. The DSSC incorporating the UC nanophosphors had an overall cell efficiency of 8.55% which is an increment ratio of 16.6% compared to the bare-TiO_2 DSSC. This increase in cell performance has been heavily attributed to the NIR-visible UC by the UC nanophosphors.

7.5 References

1) R. Ge, X. Zhao, L. Qin, Z. Feng, B. Dong, Q. Chen and Q. Li., 2011 Symposium on Photonics and Optoelectronics (SOPO), 2011, pp. 1-6, https://doi.org/10.1109/SOPO.2011.5780634

2) A. Martinez, J. Morales, L.A. Diaz-Torres, P. Salas, E. De la Rosa, J. Oliva, et al. Mater. Sci. Eng. B, 174 (2010), pp. 164-168 https://doi.org/10.1016/j.mseb.2010.04.028

3) H. S. Marder , P. Kele , S. M. Saleh and O. S. Wolfbeis , Curr. Opin. Chem. Biol., 2010, 14, 582. https://doi.org/10.1016/j.cbpa.2010.08.014

4) S. A. Wade , S. F. Collins and G. W. Baxter , J. Appl. Phys., 2003, 94 , 4743. https://doi.org/10.1063/1.1606526

5) R. L. Toquin and A. K. Cheetham , Chem. Phys. Lett., 2006, 423 , 352 https://doi.org/10.1016/j.cplett.2006.03.056.

6) S. Ye , F. Xiao , Y. X. Pan , Y. Y. Ma and Q. Y. Zhang , Mater. Sci. Eng., R, 2010, 71 , 1 https://doi.org/10.1016/j.mser.2010.07.001.

7) S. Fischer , J. C. Goldschmidt , P. Loper , G. H. Bauer , R. Bruggemann , K. Kramer , D. Biner , M. Hermle and S. W. Glunz , J. Appl. Phys., 2010, 108 , 044912 https://doi.org/10.1063/1.3478742

8) C. H. Kim , I. E. Kwon , C. H. Park , Y. J. Hwang , H. S. Bae , B. Y. Yu , C. H. Pyun and G. Y. Hong , J. Alloys Compd., 2000, 311 , 33 https://doi.org/10.1016/S0925-8388(00)00856-2

9) P. Du, J. Lim, S. Kim, J. Yu, Optical Materials Express. 6 (2016) 1896. https://doi.org/10.1364/OME.6.001896

10) F.L. Chawarambwa, T.E. Putri, K. Kamataki, M. Shiratani, K. Koga, N. Itagaki, D. Nakamura. Journal of Molecular Structure, 1228, 129479. https://doi.org/10.1016/j.molstruc.2020.129479

11) G. Wilk, R. Wallace, J. Anthony. J. Appl. Phys., 89 (2001), pp. 5243-5275 https://doi.org/10.1063/1.1361065

12) C. Cannas, M. Casu, M. Mainas, A. Musinu, G. Piccaluga, S. Polizzi, et al. J. Mater. Chem., 13 (2003), pp. 3079-308 https://doi.org/10.1039/B305992H

13) V. Swamy, N. Dubrovinskaya, L. Dubrovinsky. J. Mater. Res., 14 (1999), pp. 456-459 https://doi.org/10.1557/JMR.1999.0065

14) P. de Rouffignac, J. Park, R. Gordon. Chem. Mater., 17 (2005), pp. 4808-4814 https://doi.org/10.1021/cm050624+

15) S. Ekambaram, K. Patil, M. Maaza. J. Alloys Compd., 393 (2005), pp. 81-92 https://doi.org/10.1016/j.jallcom.2004.10.015

16) S.K. Singh, K. Kumar and S.B. Rai. Mater. Sci. Eng. B, 166 (2010), pp. 180-184 https://doi.org/10.1016/j.mseb.2009.11.018

17) P. Tadge, R. Yadav, P. Vishwakarma, S. Rai, T. Chen, S. Sapra et al., Journal Of Alloys And Compounds. 821 (2020) 153230 https://doi.org/10.1016/j.jallcom.2019.153230.

18) N. Yao, J. Huang, K. Fu, X. Deng, M. Ding, M. Shao et al., Electrochimica Acta. 154 (2015) 273-277. https://doi.org/10.1016/j.electacta.2014.12.095

19) H. Yang, F. Peng, Q. Zhang, W. Liu, D. Sun, Y. Zhao, X. Wei. Opt. Mater., 35 (2013), pp. 2338-2342 DOI:10.1016/j.optmat.2013.06.026.

20) M. Gratzel. Nature, 414 (2001), pp. 338-344 DOI: 10.1038/35104607

21) M.J. Lim, Y.N. Ko, Y.C. Kang, K.Y. Junq. RSC Adv., 4 (2014), p. 10039 https://doi.org/10.1039/C3RA47310D

22) W. He, T.S. Atabaev, H.K. Kim, Y.H. Hwang. J. Phys. Chem. C, 117 (2013), p. 17894 https://doi.org/10.1021/jp307954n

23) J.C. Goldschmidt, S. Fischer. Adv. Opt. Mater., 3 (2015), pp. 510-519 https://doi.org/10.1002/adom.201500024

24) M. Rudiger, S. Fischer, J. Frank, A. Ivaturi, B.S. Richards, K.W. Kramer, M. Hermle, C. Goldschmidt. Sol. Energy Mater. Sol. Cells, 128 (2014), pp. 57-68 https://doi.org/10.1016/j.solmat.2014.05.014

25) H. Yang, F. Peng, Q. Zhang, W. Liu, D. Sun, Y. Zhao, X. Wei. Opt. Mater., 35 (2013), p. 2338 https://doi.org/10.1016/j.optmat.2013.06.026

26) P. Du, J.H. Lim, J.W. Leem, S.M. Cha and J.S. Yu. Nanoscale Res Lett 10, 321 (2015) https://doi.org/10.1186/s11671-015-1030-0

27) W.A. Pisarski, J. Pisarska, R. Lisiecki, and W. Ryba-Romanowski. Opt. Express 25, 28501-28509 (2017) https://doi.org/10.1364/OE.25.028501

28) G. Han, M. Wang, D. Li, J. Bai, G. Diao. Sol. Energy Mater. Sol. Cells, 160 (2017), pp. 54-59 https://doi.org/10.1016/j.solmat.2016.10.021

29) X. Jin, H. Li, D. Li, Q. Zhang, F. Li, W. Sun, W.Z. Chen, Q. Li. Opt. Express, 24 (2016) A1276−A1787 https://doi.org/10.1364/OE.24.0A1276

30) J. Wang, J. Wu, J. Lin, M. Huang, Y. Huang, Z. Lan, Y. Xiao, G. Yue, S. Yin, T. Sato. ChemSusChem, 5 (2012), pp. 1307-1312 https://doi.org/10.1002/cssc.201100596

31) F.L. Chawarambwa, T.E. Putri, P. Attri, K. Kamataki, M. Shiratani, K. Koga, N. Itagaki. Chem. Phys. Letts, 768, 138369 https://doi.org/10.1016/j.cplett.2021.138369

32) V. Vasanthi, M. Kottaisamy, V. Ramakrishnan. Journal of Materials Science: Materials in Electronics, vol. 29, no. 23, 2018, pp. 19724–19731., https://doi.org/10.1007/s10854-018-0097-7

33) A. Pandey and V.K. Rai. (2013). Dalton Transactions, 42(30), 11005. https://doi.org/10.1039/c3dt50592h

34) G. Xiang, Y. Ma, W. Liu, S. Jiang, X. Luo, L.L. Zhou, Z. Gu, J. Wang, Y. Luo, Y.J. Zhang. Inorg. Chem., 56 (2017), pp. 9194-9199 https://doi.org/10.1021/acs.inorgchem.7b01236

35) M. Pollnau, D.R. Gamelin, S.R. Luthi, H.U. Gudel. Phys. Rev. B, 61 (2000), pp. 3337-3346 https://doi.org/10.1103/PhysRevB.61.3337

36) S. Xu, G. Wang, S. Dai, J. Zhang, L. Hu, and Z. Jiang. J. Lumin. 109, 187–192 (2004) https://doi.org/10.1016/j.jlumin.2004.02.007

37) F. Auzel. Chem. Rev. 104(1), 139–173 (2004) https://doi.org/10.1021/cr020357g

38) Zou Z, Wang J, Nan F, Bu C, Yu Z, Liu W, et al. Nanoscale. (2014) 6:20525–2055. https://doi.org/10.1039/C3NR04315K

CHAPTER EIGHT: Summary and Recommendations

8.1 Summary

In this doctorate thesis, we have successfully developed various efficient and cost-effective materials that can be applied separately to the DSSC. Written below, are summaries of all the studies and achievements that we have conducted in this study.

CHAPTER 4 describes the development of quasi-solid electrolytes for application in DSSC. Liquid electrolytes are volatile, leading to leakage, which in turn reduces the long-term stability of the DSSC. To solve this problem, we prepared three printable polymer gel electrolytes with excellent conductivity and electrocatalytic performance. The quasi-solid dye-sensitized solar cell (QSDSSC) with the TiO_2 nanofillers, which exhibited an overall cell efficiency of 5.02 % (under 1 sun illumination) was higher than DSSC with the liquid electrolyte (4.59 %). Further, we investigated the performance of the QSDSSC under focused light irradiation using a concentric mirror. Under focused light, the system efficiency of the QSDSSC was enhanced above ~5 times as compared to the control (without focused light). Furthermore, we studied the impact of light soaking time on the photovoltaic performance of QSDSSCs under focused, concentrated light. The QSDSSCs have exhibited higher predominant stability than the liquid DSSC due to the 3-D frame formed by the nanofillers and polymers, which effectively prevent evaporation and leakage of the electrolyte. Hence, our QSDSSCs retain high efficiency and stability at higher temperatures.

CHAPTER 5 describes the effect of stepwise co-sensitization on the performance of the DSSC. Co-sensitization is an excellent technique to enhance the performance of a DSSC by broadening the cell's absorption spectrum. Therefore, in this study, we used ruthenium- (Z907) and organic- (SQ2) based sensitizers having a wide range of absorption spectra (300-750 nm). We observed that the dye loading procedure and dye soaking time influence the photovoltaic performance of the co-sensitized DSSCs. Fabricated DSSCs have been evaluated using incident photon conversion efficiency (IPCE), electrochemical impedance (EIS), and current-voltage characteristics. Interestingly, the results indicate an increase in the IPCE for co-sensitized DSSCs in the 620-720 nm range. The general increase in overall IPCE was observed as the soaking time

in SQ2 dye was increased from 0 to 1 h. Although, a further rise in SQ2 dye soaking time results in significant IPCE reduction between the 400-620 nm range. The reduction in IPCE can be attributed to several factors but mainly due to a) the replacement of the pre-adsorbed Z907 molecules by the post-adsorption of SQ2 molecules and/or b) the aggregation of dye molecules due to overloading. Upon optimization, the co-sensitized DSSC exhibits an efficiency of 5.75 %, enhanced by 12% and 462% compared with the DSSC with single Z907 (5.12%) and SQ2 (1.06%), respectively. The results indicate that the dye loading procedure and dye soaking time significantly affect the photovoltaic performance of the DSSC.

CHAPTER 6 describes the experimental details of the development of a PEDOT:PSS/Triton X-100/TiO_2 CE. Poly (3, 4-ethylenedioxythiophene): poly (styrene sulfonate) (PEDOT:PSS) is a well-known conductive polymer that is often used as a counter electrode (CE) in DSSCs. PEDOT:PSS is highly favored due to its high transmittance and conductivity. However, the low electrocatalytic activity of PEDOT:PSS due to the flatness of its surface results in a low fill factor and low overall cell conversion efficiency. To address this limitation in PEDOT:PSS, 3 wt% of iso-octyphenoxy-polyethoxyethanol (Triton X-100), 5 wt% DMSO and 5mg TiO_2 NPs were mechanically added to PEDOT:PSS. The addition of Triton X-100 to PEDOT:PSS enhances the adhesion of the PEDOT:PSS with the FTO glass, and enhances the surface area of PEDOT:PSS which ultimately improves the electrocatalytic properties of PEDOT:PSS CE. TiO_2 NPs, in enhances the conductivity and surface area of PEDOT:PSS. A bifacial DSSC based on the PEDOT:PSS/TX100/TiO_2 was fabricated, and its photovoltaic characteristics were obtained under simulated solar light of 100 mWcm^{-2}. Under bifacial illumination, the DSSC with the Pt CE achieved a current density (J_{sc}) of 16.16 mAcm^{-2} and system efficiency (E_{sys}) of 8.67% while the $_{DSSC}$ with the PEDOT:PSS/DMSO/TX100/TiO_2 CE achieved a J_{sc} of 17.72 mAcm^{-2} and an E_{sys} of 9.14%. PEDOT:PSS/DMSO/TX100/TiO_2 CE is very stable, has a high transmittance, exhibits high electro-catalytic activity, and is an excellent substitute for Pt CE.

CHAPTER 7 describes the synthesis of up-conversion (UC) nanoparticles. UC materials can convert low-energy photons into visible light and, therefore, can be incorporated into solar cells to increase the absorption of visible light. This study synthesized UC nanophosphors Yb^{3+}, Er^{3+}: Y_2O_3 and Yb^{3+}, Er^{3+}, Zn^{2+}: Y_2O_3 by a simple co-precipitation method for application in dye-

sensitized solar cells (DSSCs). The impact of the enhancement in the concentration of Zn^{2+} on the photoluminescence (PL) and color point of the synthesized nanophosphors was also investigated. The synthesized UC nanophosphors emitted strong red and weaker green emissions upon excitation at 980 nm. The addition of Zn^{2+} to the Yb^{3+}, Er^{3+}: Y_2O_3 nanophosphors leads to color tunability in the yellow and red regions. Moreover, the synthesized UC nanophosphors were incorporated into the DSSC photoanode to form a TiO_2-UC-based DSSC for converting near-infrared (NIR) into visible light. The study has indicated that the TiO_2-UC-based DSSC showed an enhancement ratio in current density and power conversion efficiency of 17.4% and 16.6%, respectively when compared to the normal DSSC. These results reveal that UC-based Yb^{3+}, Er^{3+}, Zn^{2+}: Y_2O_3 nanophosphors are useful in improving the efficiency of DSSCs and in color tunability applications.

8.2 Future Recommendations

For the past 3 decades, a lot of studies have been done to enhance the efficiency of, long-term stability and reduce the cost of dye-sensitized solar cells. Along the way, we have seen some improvements however, we are yet to witness some breakthroughs especially when it comes to the efficiency of the DSSC. In this study, we have developed new quasi-solid electrolytes using various nanofillers and polymer gels. With these new QSEs, we have also developed a way of improving the overall cell performance by coupling the DSSC with a concentrated power system (CPS). Coupling the DSSC with a CPS yields a performance that is at least 5 times that of the normal DSSC. From these results, the benefit of the new system is clear, however, there were still some unresolved issues. For example, although the QSDSSC was comparatively more stable than the liquid DSSC, its performance was limited under bifacial illumination due to its low transmittance. Therefore, there is a need to develop high transmittance and thermally stable QSE. The stability of the DSSC could also be improved using solid electrolytes. Currently, a lot of studies are being carried out however, the progress seems to be too slow.

In this study, we have also developed new, efficient, and cost-effective counter-electrode materials for application in DSSC. Although the CE (PEDOT: PSS/DMSO/TX100/TiO_2) that we developed matches the performance of the conventional Pt CE, it does not significantly

outperform the Pt CE. The performance of both CES is similar. From these results, it can be observed that we have reached a limit in terms of the performance of the CE. Therefore, new studies need to be conducted to find ways of breaking through this barrier.

Lastly, we have also developed UC nanophosphors (Yb^{3+}, Er^{3+}, Zn^{2+}: Y_2O_3) for application in DSSC. Although the fabricated UC exhibited high photoluminescence properties, the conversion rate when incorporated into the DSSC was quite low. The UC nanophosphors only managed to enhance the performance of DSSC by ~16.6%. One of the obvious challenges could be that the fabricated nanoparticles have a large size ~250-300 nanometers. Smaller sizes could yield better results since they will be able to incorporate directly into the transparent TiO_2. In this study, a co-precipitation homogenous process has been utilized. This method has the advantage of being simple and produces nanoparticles with uniform sizes. The future study could include developing new fabrication methods for the development of smaller-sized nanophosphors with uniform sizes and finding better methods of incorporating the UC materials into the DSSC.

Acknowledgments